Fakultät für Mathematik und Naturwissenschaften | RWTH AACHEN UNIVERSITY

Dissecting inflammatory microenvironments during aging and their effect on the development of chronic blood cancer

Von der Fakultät für Mathematik und Naturwissenschaften der RWTH Aachen University zur Erlangung des akademischen Grades eines Doktors der Naturwissenschaften genehmigte Dissertation

vorgelegt von

Salim Atakhanov, M.Sc.

aus

Taschkent, Usbekistan

Berichter*:* *Univ.-Prof. Dr.rer.nat. Oliver Pabst*

Univ.-Prof. Dr.med. Rebekka Schneider-Kramann, PhD

Univ.-Prof. Dr.rer.nat. Ralph Panstruga

Tag der mündlichen Prüfung*:* *23.06.2026*

“If I have seen further, it is by standing on the shoulders of Giants”,

- Isaac Newton

Table of Contents

1 Zusammenfassung

Die tumorassoziierte Remodellierung des Knochens wird traditionell als ein unidirektionaler Prozess verstanden, der entweder zu pathologischer Knochenneubildung oder zu Knochenverlust führt. Myeloproliferative Neoplasien (MPN) sind eine Gruppe von hämatologischen Krebserkrankungen, die überwiegend durch die JAK2V617F-Mutation verursacht werden und stellen ein einzigartiges Krankheitsmodell dar, in dem die onkogene Hämatopoese zur Entstehung von Knochenmarkfibrose (Myelofibrose) sowie Osteosklerose führt. Dieses Krankheitsbild wurde bislang vor allem einer gestörten Funktion von Osteoklasten zugeschrieben.

In dieser Arbeit wird dieses Paradigma grundlegend hinterfragt. Es wird gezeigt, dass ein einzelner onkogener hämatopoetischer Klon gleichzeitig pathologische Knochenneubildung und aktiven Knochenabbau induzieren kann, in Abhängigkeit der anatomischen Nische und ontogenetischen Herkunft. Osteosklerose verhindert demnach keinen Knochenverlust, sondern überlagert lokal bestehende osteolytische Remodellierungsprozesse. Durch einen interdisziplinären Ansatz aus populationsbasierten Analysen, klinischer Bildgebung, patientenbasierten Einzel-Zell-Sequenzierungen verschiedener Gewebe, murine Krankheitsmodellen sowie humanen Organ-on-a-Chip-Systemen konnte eine bidirektionale Wechselwirkung zwischen MPN und Parodontitis aufgezeigt werden.

Dabei wurde eine bislang unbekannte osteochondrale stromale Verletzungsantwort identifiziert, die sowohl aus der Neuralleiste stammenden als auch Knochen mesodermalen Ursprungs betrifft. Dieses Programm involviert eine konservierte Thrombospondin-1-positive ($Thbs1^{+}$) Stromazellpopulation, welche fibrotische Umwandlungsprozesse funktionell mit Knochenabbau verknüpft. Die kombinierte pharmakologische Hemmung von Thbs1 und JAK2 führte zu einer synergistischen Normalisierung sowohl osteosklerotischer als auch osteolytischer Veränderungen und identifiziert Thbs1 als krankheitsmodifizierenden therapeutischen Angriffspunkt in der Myelofibrose.

Darüber hinaus verstärkt parodontale Entzündung reziprok die maligne Hämatopoese, verändert das Knochenmark-Stammzellkompartiment und begünstigt fibrotische Transformation. Zur mechanistischen Untersuchung dieser systemischen Interaktion wurde eine humane Multi-Organ-on-a-Chip-Plattform entwickelt, die entzündungsinduzierte hämatopoetische Reprogrammierung abbildet und die Migration mutierter Immunzellen zu entfernten Entzündungsnischen sichtbar macht.

Zusammenfassend stellen diese Erkenntnisse das Konzept einheitlicher Gewebereaktionen, die ausschließlich durch onkogene Signalwege gesteuert werden, infrage und definieren stattdessen die Ontogenese des Stromas und die Plastizität der

Abstammungslinien als zentrale Determinanten der tumorassoziierten Knochenpathologie.

2 Abstract

Cancer-associated bone remodeling is traditionally viewed as a unidirectional process leading either to pathological bone formation or bone loss. Myeloproliferative neoplasms (MPNs), a group of hematologic cancers predominantly driven by the JAK2V617F mutation, provide a unique model in which oncogenic hematopoiesis profoundly reshapes the skeletal microenvironment, resulting in bone marrow fibrosis (myelofibrosis) and osteosclerosis. This phenotype has historically been attributed to impaired osteoclast function.

In this thesis, we challenge this paradigm and demonstrate that a single oncogenic hematopoietic clone can simultaneously drive pathological bone formation and active bone destruction in a niche- and ontogeny-dependent manner. Rather than preventing bone loss, osteosclerosis conceals spatially restricted osteolytic remodeling. Through an interdisciplinary strategy integrating population-level analyses, clinical imaging, patient-derived single-cell multi-tissue sequencing, murine models, and human organ-on-a-chip systems, we uncover a bidirectional interaction between MPN and periodontal disease.

We identify a previously unrecognized osteochondral stromal injury program shared across mesoderm- and neural crest–derived bones. This remodeling response is mediated by a conserved Thrombospondin-1–expressing ($Thbs1^{+}$) stromal population that functionally links fibrotic remodeling to bone degeneration. Combined pharmacological inhibition of Thbs1 and JAK2 signaling synergistically restores both osteosclerotic and osteolytic skeletal abnormalities, establishing Thbs1 as a unifying and disease-modifying target in myelofibrosis.

Importantly, periodontal inflammation reciprocally aggravates malignant hematopoiesis, rewires the bone marrow stem cell compartment, and primes fibrotic transformation. To mechanistically model this systemic crosstalk, we developed a human multi-organ-on-a-chip platform that recapitulates inflammation-induced hematopoietic remodeling and enables real-time tracking of mutant immune cell mobilization toward distant inflammatory tissues.

Collectively, these findings challenge the concept of uniform tissue responses driven solely by oncogenic signaling and instead define stromal ontogeny and lineage plasticity as central regulators of cancer-associated bone pathology.

3 Introduction

3.1 Hematopoiesis

The human hematopoietic system is responsible for the continuous production of vast numbers of mature blood cells, generating billions each day and making an annual estimated count of 1,4 x 10^{14} cells[1]. This remarkable regenerative capacity is sustained by a rare population of hematopoietic stem cells (HSCs), which serve as the foundation of lifelong blood formation.

Conceptual understanding of the hematopoietic hierarchy has evolved considerably over time. The term “stem cell” was first introduced by Ernst Haeckel in 1868, originally referring to a unicellular organism as the progenitor of all multicellular life forms. This notion inspired the early depiction of hematopoiesis as a branching tree, with HSCs positioned at the root. HSCs possess the dual capacity for self-renewal and differentiation, enabling lifelong maintenance of the blood system[2]. Through a hierarchical process, HSCs give rise to multipotent progenitors (MPPs), which further differentiate into lineage-committed progenitors and ultimately mature blood cells. Throughout the differentiation, the hematopoietic stem and progenitor cells (HSPCs) exhibit progressively reduced self-renewal capacity and lifespan.

During mammalian development, hematopoiesis occurs in several sequential waves. The earliest wave originates in the yolk sac blood islands, where primitive hematopoiesis takes place. In humans, this phase occurs within the first three weeks of gestation and primarily supports embryonic oxygen transport through the generation of nucleated erythrocytes expressing embryonic globins[3]. In addition to erythroid cells, early monocyte/macrophage and megakaryocytic populations also emerge. Subsequently, erythromyeloid progenitors arise from hemogenic endothelial cells within the yolk sac vasculature. These progenitors enter the circulation and migrate to the fetal liver around eight weeks of gestation, marking the onset of definitive hematopoiesis and constituting the second developmental wave. This stage is characterized by the production of enucleated erythrocytes expressing fetal globins and the emergence of lymphoid progenitors derived from hemogenic endothelium[4]. Importantly, blood cell formation from hemogenic endothelial cells occurs through an

endothelial-to-hematopoietic transition (EHT), rather than by asymmetric cell division[5]. In parallel with the yolk sac, the aorta-gonad-mesonephros (AGM) region serves as an intraembryonic site of definitive hematopoiesis. The third hematopoietic wave involves the generation of bona fide HSCs from the AGM, which possess long-term multilineage reconstitution capacity. In human embryos, functional HSC engraftment potential is first detected around day 32 of gestation[6].

As development progresses toward birth, the primary site of hematopoiesis shifts from the fetal liver to the bone marrow. Recent work has identified a specialized VCAM1-expressing vascular niche within the fetal bone marrow that directs the recruitment of definitive hematopoietic stem and progenitor cells from the fetal liver[7]. This niche is spatially organized by yolk sac–derived myeloid cells, particularly osteoclasts, and is both necessary and sufficient for efficient bone marrow colonization, as disruption of VCAM1 signaling impairs seeding while ectopic VCAM1 expression promotes de novo recruitment. These findings highlight the importance of niche-mediated guidance in establishing lifelong hematopoiesis. Beyond the bone marrow, HSC trafficking and localization are influenced by additional physiological systems, stress factors and other hematopoietic niches. The sympathetic nervous system regulates the rhythmic mobilization of HSCs into peripheral blood through circadian secretion of noradrenaline[8]. Moreover, upon hematopoietic stress (e.g. myeloablation), HSCs have been identified in extramedullary sites such as the spleen[9] and lungs[10]. The functional contributions of these extramedullary niches to HSC migration, differentiation, maintenance, and clonal expansion remain largely unexplored, particularly at single-cell resolution.

For many years, HSCs were considered a homogeneous population, giving rise to two major progenitor branches: the common myeloid progenitor (CMP) and the common lymphoid progenitor (CLP). However, the development of dynamic and quantitative models of physiological hematopoiesis has been limited by the absence of experimental methods capable of capturing processes at single-cell resolution. Recent single cell RNA sequencing (scRNAseq) approaches in combination with mathematical modeling, phenotypic characterization and functional validation reveal functionally heterogeneous HSC pools and challenge the current understanding of hierarchical HSC differentiation trajectories during homeostasis, aging and disease[2,11,12], highlighting the complexity of hematopoietic development. Continued

investigation into the cellular and molecular mechanisms governing hematopoiesis is therefore essential to fully elucidate lineage relationships and accurately model the hematopoietic hierarchy.

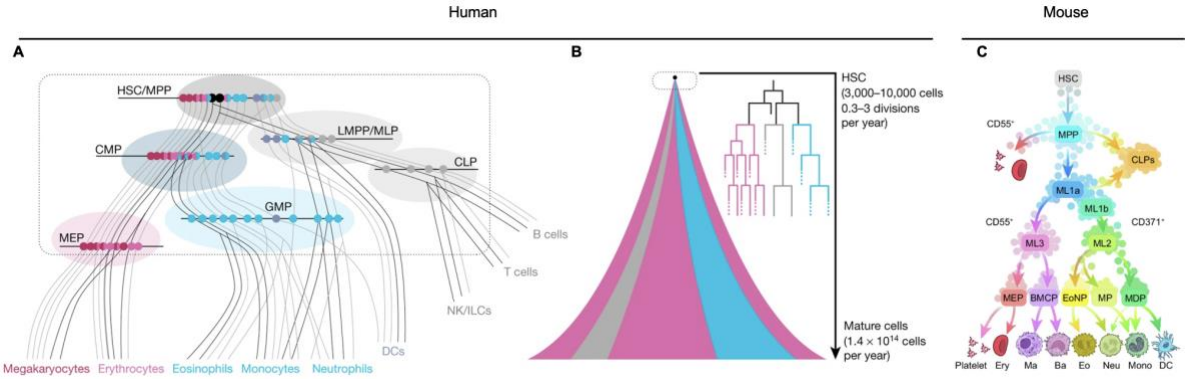

Figure 1: Hierarchical model of early hematopoiesis.

(A) Gradually developing lines represent a heterogenous human HSC compartment (dark grey area) giving rise to the trajectory of differentiation for various types of single cells. HSC pool contains multipotent cells illustrated as black circles. During the trajectory, HSCs differentiate towards progenitor cells (shaded areas) defined by specific combinations of cell surface markers. Each progenitor compartment contains horizontal lines (lineage potential) with either single-color or multiple-color circles representing oligo- or multilineage cells, respectively. Overall, the figure demonstrates the differentiation potential of heterogenous HSCs towards mature myeloid and lymphoid cells.

(B) Depiction of the lineage output from a single hematopoietic stem cell (HSC), with erythroid, myeloid, and lymphoid cells shown in pink, blue, and grey, respectively. The model illustrates cell division history and progenitor expansion throughout differentiation. In adults, the HSC pool comprises approximately 3,000–10,000 cells, each dividing infrequently, yet collectively sustaining the annual production of about 1.4×10^{14} mature blood cells.

(C) Recent study using multi-omic approach revealed murine hematopoietic differentiation proceeding through distinct cellular states along developmental pathways. Identified markers from this study reflecting early transcription factor activation, including CD55 and CD371, are indicated.

(A) and (B) are adapted from Laurenti and Göntgens[1]. (C) is adapted from Ferchen, K., Zhang, X., Thakkar, K. *et al.*[12]

3.2 Clonal hematopoiesis of indeterminate potential

While hematopoiesis is tightly regulated to ensure balanced blood cell production throughout life, this system is not immune to genetic alterations that accumulate over time. Hematopoietic stem cells undergo continuous proliferation and differentiation, providing opportunities for somatic mutations to arise and become fixed within the stem cell compartment. Although most mutations are functionally neutral or eliminated,

certain genetic alterations confer a selective growth advantage, enabling mutated HSCs to expand clonally. This phenomenon, termed clonal hematopoiesis of indeterminate potential (CHIP), represents an age-associated process characterized by the dominance of genetically distinct hematopoietic clones within an otherwise polyclonal blood system.

Many of the genetic and epigenetic alterations observed in CHIP overlap with mutations commonly found in hematologic malignancies such as myelodysplastic syndromes (MDS), myeloproliferative neoplasms (MPNs) and acute myeloid leukemia (AML)[13]. Although the presence of these mutations increases the risk of malignant transformation, the vast majority of individuals with CHIP do not progress to overt blood cancer. Aging is accompanied by a state of chronic low-grade inflammation, called “inflammageing”, suggesting that inflammatory processes may contribute to both the emergence and expansion of mutant hematopoietic clones. Inflammation may promote genomic instability, facilitating mutation acquisition, while simultaneously providing a selective advantage to specific clones.

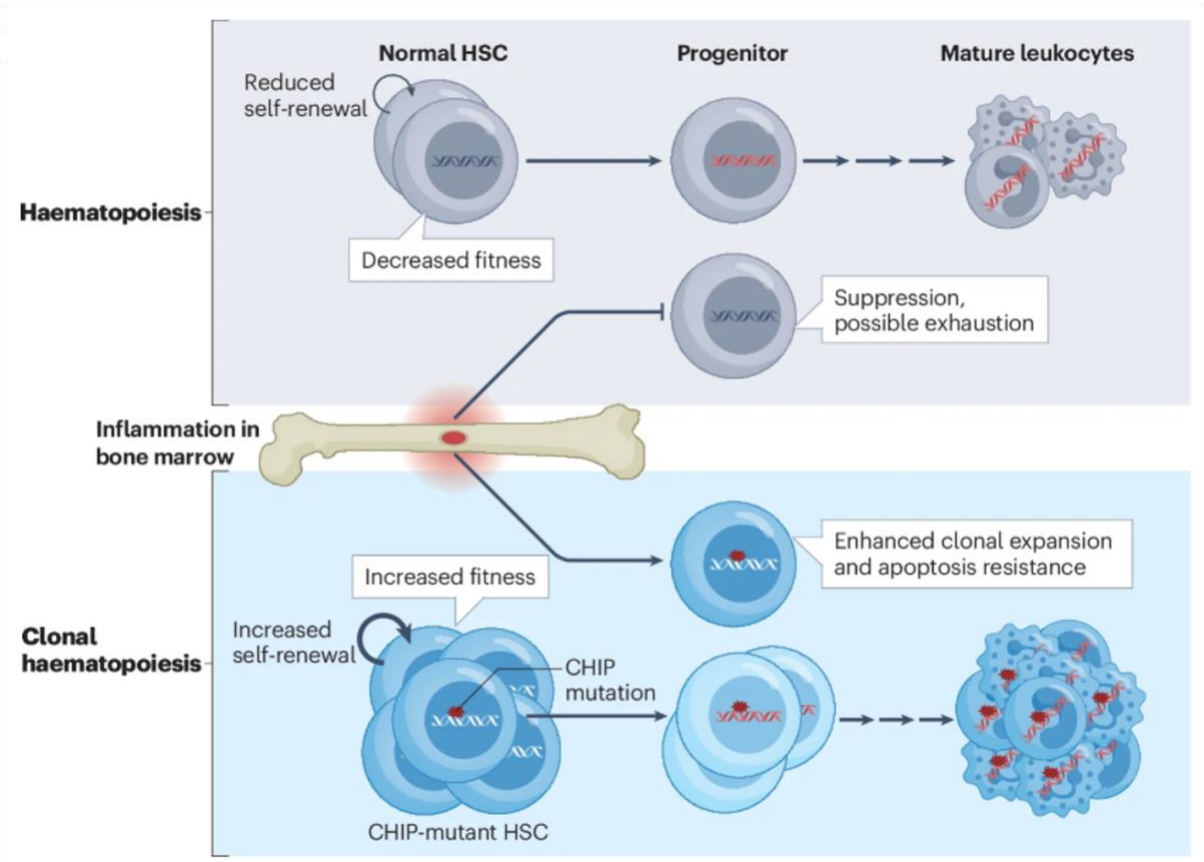

Figure 2: Overview of the effect of inflammation on normal and clonal hematopoiesis.

Persistent inflammatory signaling can impair normal HSC function, driving features commonly associated with hematopoietic aging (inflammaging), including reduced regenerative capacity and, in some cases, stem cell exhaustion. In contrast, hematopoietic clones harboring CHIP-associated mutations display an increased ability to tolerate inflammatory conditions and often gain a competitive growth advantage over non-mutant counterparts. As a result, inflammatory environments selectively disadvantage healthy HSCs while simultaneously favoring the persistence and expansion of mutant clones. Figure modified from Hajishengalis and Chavakis[13].

The progressive accumulation and expansion of such clones can subtly reshape hematopoietic output and the bone marrow microenvironment, serving as a critical intermediary state between normal hematopoiesis and overt hematologic malignancy. Cancer cells frequently exhibit substantial phenotypic diversity, even among patients carrying identical genetic mutations. Recent lineage-tracing strategies in combination with scRNAseq approaches have demonstrated that the functional consequences of myeloid malignancy-associated mutations depend strongly on the differentiation state of the cell of origin[14]. Mutations acquired in specific stem cell populations can promote clonal expansion or reprogram developmental trajectories, thereby generating diverse malignant phenotypes. These findings suggest that the timing of somatic mutation acquisition during hematopoietic differentiation critically shapes disease behavior and may underlie heterogeneity in cancer presentation and therapeutic response among patients harboring the same genetic lesions.

Among CHIP-associated mutations, alterations in *TET2* represent the second most frequently observed genetic events[15]. Recent studies have linked TET2 deficiency to heightened inflammatory responses. Consistent with this, CHIP has been strongly associated with chronic diseases such as cardiovascular disease, potentially mediated by increased systemic inflammation[13]. Indeed, experimental evidence shows that CHIP promotes atherosclerosis through TET2-deficient bone marrow–derived macrophages, which exhibit elevated secretion of inflammatory chemokines[16].

Interestingly, not all effects of CHIP appear to be detrimental. Other studies have reported that certain CHIP clones may exert protective roles, including an association with reduced risk of Alzheimer's disease, although the underlying mechanisms remain unclear[17].

Therefore, understanding the biological mechanisms governing clonal selection, expansion, and leukemogenic potential is essential for elucidating the earliest stages of hematologic cancer development.

3.3 Myeloproliferative neoplasms

Myeloproliferative neoplasms (MPNs) constitute a group of chronic hematologic malignancies driven by somatic mutations in the JAK2, CALR, or MPL genes, which result in constitutive activation of the JAK–STAT signaling pathway within hematopoietic stem cells (HSCs). The most prevalent alteration is the JAK2V617F mutation, present in approximately 60% of patients, followed by mutations in calreticulin (CALR) in about 30% and in the myeloproliferative leukemia virus oncogene (MPL) in roughly 8%[18]. These genetic lesions promote uncontrolled myeloid proliferation and profoundly reshape the bone marrow microenvironment.

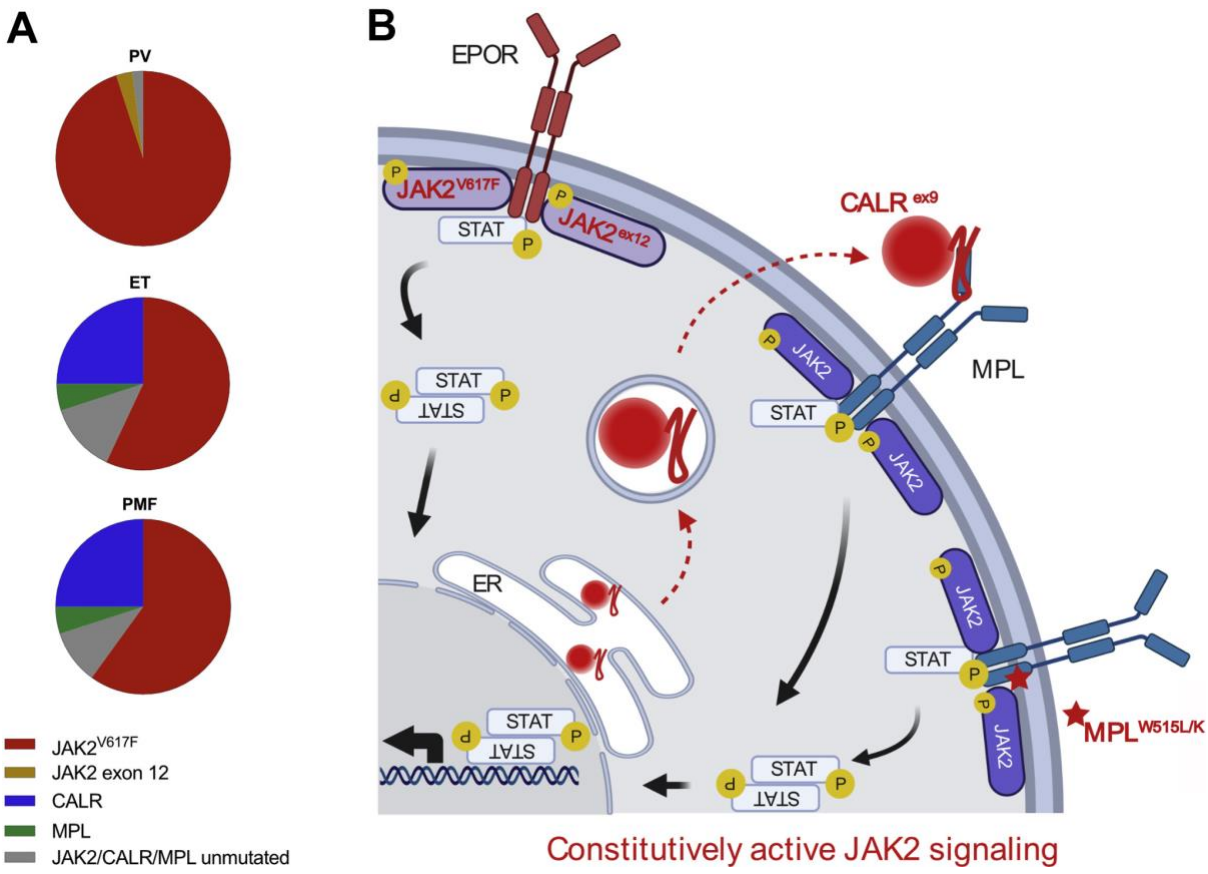

Figure 3: Recurrent somatic driver mutations in myeloproliferative neoplasms converge on constitutive JAK–STAT pathway activation.

(A) Relative prevalence of JAK2V617F, JAK2 exon 12, CALR, and MPL mutations across polycythemia vera (PV), essential thrombocythemia (ET), and primary myelofibrosis (PMF). Cases lacking mutations in JAK2, CALR, and MPL are classified as triple-negative MPNs.

(B) JAK2 V617F mutations are found in conjunction with signaling through the erythropoietin receptor (EPOR) and the thrombopoietin receptor (MPL) across all MPN subtypes. Despite their genetic diversity, these driver mutations uniformly result in persistent activation of JAK2–STAT signaling. Figure adapted from Szybiskni and Meyer[19].

However, several studies have demonstrated that the JAK2V617F mutation can be detected decades before the clinical onset of MPNs[20], indicating that its acquisition does not immediately result in strong clonal expansion and that disease development may require prolonged latency. In some cases, JAK2V617F has even been identified in cord blood[21], and may arise during prenatal life or early childhood[22,23]. In contrast to JAK2V617F, CALR alterations are generally acquired later, potentially reflecting a greater proliferative advantage[24]. Collectively, these findings indicate that driver mutations can remain present within hematopoietic clones for decades before progressing to overt MPN, highlighting the long preclinical phase of disease evolution. What determines the progression from mutation acquisition to CHIP and overt MPN remains incompletely understood.

Clinically, MPNs include essential thrombocythemia (ET), polycythemia vera (PV), and primary myelofibrosis (PMF), all characterized by a bias toward myeloid lineage differentiation. Disease course and prognosis vary considerably among patients and are commonly assessed using risk stratification tools such as the International Prognostic Scoring System (IPSS), the Dynamic IPSS-Plus, and genetically informed prognostic models. These scoring systems underscore the marked heterogeneity of outcomes, with median survival extending beyond 15 years in low-risk patients but decreasing to approximately one year in high-risk disease[18]. While PMF is characterized by fibrotic transformation at presentation, a substantial proportion of patients with ET or PV eventually progress to secondary myelofibrosis. Furthermore, approximately 20% of MPN cases undergo transformation into secondary acute myeloid leukemia, representing a major cause of disease-related mortality[18].

The diagnosis of myelofibrosis relies on bone marrow biopsy with reticulin staining to evaluate the extent of fibrotic deposition. MF exemplifies tumor-induced fibrotic remodeling, in which excessive accumulation of extracellular matrix progressively

disrupts normal hematopoiesis and culminates in bone marrow failure. This pathological process is frequently accompanied by aberrant bone formation, termed osteosclerosis, as well as persistent inflammatory signaling that contributes to systemic manifestations of disease. Emerging evidence indicates that chronic inflammation is a key driver of MPN pathogenesis, influencing disease initiation, fibrotic progression, and leukemic transformation[25]. Various hematopoietic cell populations, including megakaryocytes and monocytes, have been implicated in sustaining inflammatory networks; however, the precise mechanisms through which mutant hematopoietic clones activate stromal cells remain insufficiently defined.

Epidemiological studies from Europe and the United States estimate the prevalence of MPNs to range between 2.5 and 5.7 cases per 100,000 individuals[26]. Despite advances in symptom-directed therapies, allogeneic hematopoietic stem cell transplantation (allo-HSCT) remains the only potentially curative treatment. Its use, however, is restricted by advanced patient age, comorbidities, and significant procedure-related risks, leaving the majority of patients dependent on non-curative management strategies.

Current therapeutic options for MPNs are largely symptomatic and fail to fundamentally alter disease progression. Among approved treatments, the JAK1/2 inhibitor ruxolitinib was introduced to suppress aberrant oncogenic signaling. However, its impact on reducing the JAK2V617F mutant allele burden remains limited, indicating that direct targeting of mutant clone expansion is not its primary mechanism of benefit. Instead, accumulating evidence suggests that ruxolitinib primarily alleviates hallmark disease manifestations, such as splenomegaly and elevated white blood cell counts, by dampening inflammatory cytokine production from both stromal cells and non-mutant hematopoietic populations, rather than eliminating the malignant clone itself[27].

Furthermore, recent studies have highlighted potential unintended consequences of ruxolitinib therapy, including the preferential expansion of RAS-mutant clones within both mutant and non-mutant hematopoietic compartments[28]. Given that RAS mutations are associated with poorer clinical outcomes in MPN patients, these findings underscore the importance of screening for pre-existing resistance-associated mutations to optimize therapeutic strategies.

This therapeutic limitation highlights an urgent need for novel disease-modifying approaches aimed at targeting both the malignant clone, fibrotic transformation process and the inflammatory microenvironment that sustain MPN progression.

3.4 Bone remodeling in myelofibrosis

The bone marrow (BM) is a structurally and functionally complex organ composed of multiple interacting cell populations that collectively sustain and regulate hematopoiesis[29]. Its cellular composition includes diverse subsets of mesenchymal stromal cells (MSCs), endothelial cells, neuronal elements, and hematopoietic cells. Functionally, the BM can be broadly divided into two spatially and biologically distinct microenvironments: the endosteal niche and the central niche[29]. A hematopoietic niche is defined as a specialized microenvironment formed by both hematopoietic and non-hematopoietic cells that supports hematopoietic stem cell (HSC) maintenance, survival, and functional regulation[30].

The central niche occupies the majority of the marrow cavity and contains most sinusoidal and arteriolar vasculature[29,30]. It plays a dominant role in sustaining steady-state hematopoiesis and the continuous production of circulating blood cells. In contrast, the endosteal niche is located adjacent to the mineralized bone surface and has been proposed to provide a protective environment that limits exposure to genotoxic stress. This niche is associated with the maintenance of HSC quiescence and is particularly important during regenerative and stress-induced hematopoiesis.

Regardless of their spatial niche, HSCs are typically found in close association with perivascular stromal cells, which play a critical role in supporting vascular integrity and regulating stem cell behavior. Distinct perivascular cell populations are associated with specific vascular compartments. Nestin^{high} neural-glial antigen 2 (NG2)+ perivascular cells are enriched around transition zone vessels in the endosteal niche and arterioles within the central niche, whereas Nestin^{low} leptin receptor (LepR)+ CXCL12-abundant reticular (CAR) cells predominantly localize to sinusoidal vessels in the central niche[29,30]. CAR cells are notable for their high expression of essential HSC-supportive factors, including CXCL12 and stem cell factor (SCF), which are indispensable for HSC retention and functional stability.

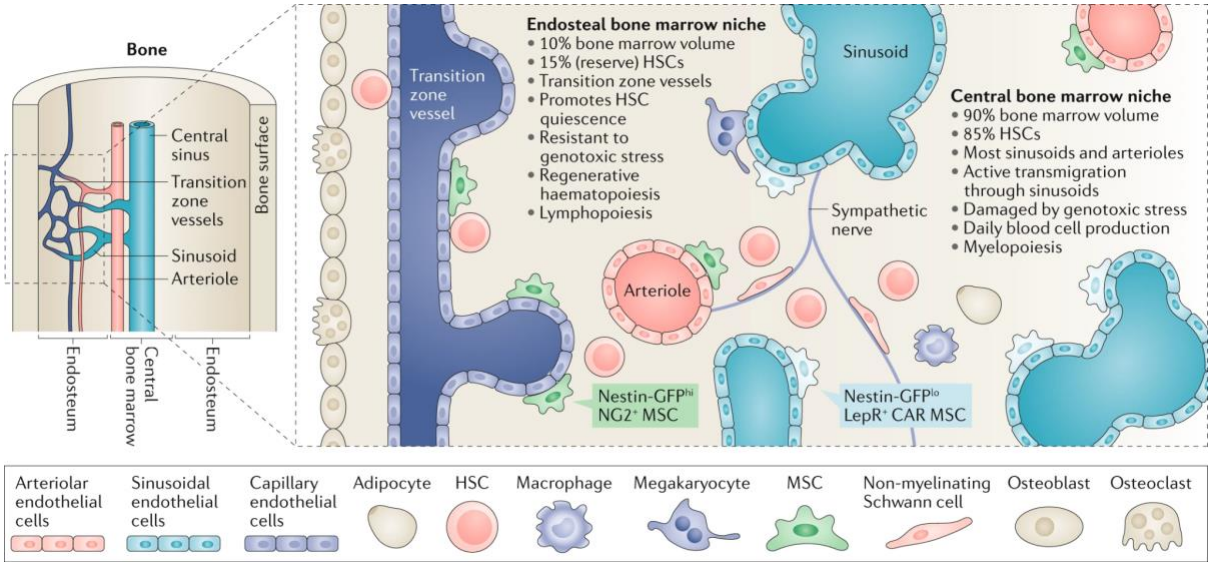

Figure 4: Bone marrow microenvironment.

Overview of endosteal and perivascular (central) bone marrow niche with functional features of each of these niches under steady-state condition. Figure adapted from Mendez-Ferrer et al.[29]

In addition to stromal and endothelial components, a variety of other cell types contribute to niche regulation, either directly or indirectly. These include osteoblasts, as well as hematopoietic cells such as megakaryocytes and macrophages, which secrete cytokines and growth factors that influence HSC fate decisions within the marrow microenvironment[8,29]. The spatial organization of these niches and the coordinated involvement of multiple cellular players underscore the tightly controlled nature of HSC regulation. Disruption of this balance, however, can occur during the development and progression of hematological malignancies, leading to altered stem cell behavior and niche dysfunction[31].

In MPNs, this tightly controlled system becomes profoundly disrupted. Mutant hematopoietic cells engage in pathological cross-talk with stromal populations, driving fibrotic transformation, aberrant bone remodeling, and sustained inflammatory responses[32]. Progressive activation of stromal cells not only promotes myelofibrosis and osteosclerosis but also contributes to declining hematopoietic function and worsening clinical outcomes.

Recent work from our group has identified Gli1-positive stromal cells as key mediators of fibrotic progression and promising therapeutic targets[33]. Through genetic fate

mapping and multi-omics approaches, we demonstrated that distinct anatomical niches within long bones generate specialized stromal responses to malignant hematopoiesis. Peritrabecular osteolineage-derived Gli1+ mesenchymal stromal cells migrate toward the central marrow and contribute to osteosclerosis in response to mutant hematopoietic signals, while Ly6A+ fibroblasts adopt an inflammatory, collagen-producing phenotype. These findings reveal substantial stromal plasticity and emphasize the importance of niche-specific microenvironmental responses in MF pathogenesis.

Studies of bone remodeling in MF have revealed that the cells traditionally responsible for bone resorption (osteoclasts) are not only increased in number but are also derived from the malignant hematopoietic clone and exhibit functional defects[34]. Analyses of bone marrow biopsies from myelofibrosis patients showed abundant tartrate-resistant acid phosphatase (TRAP)-positive osteoclasts. Notably, the proposed clonal origin of osteoclasts in MF was based on signaling activity rather than direct genetic profiling. Phosphorylated JAK2 was detected in TRAP-positive osteoclasts within bone marrow biopsies, indicating active JAK–STAT signaling in these cells. Given the disease context, this signaling pattern was interpreted as consistent with the JAK2V617F genotype, supporting the conclusion that osteoclasts arise from the malignant hematopoietic clone and are functionally impaired. The persistence of increased but dysfunctional osteoclasts suggests that defective bone degradation may contribute to the imbalance in bone turnover observed in MF, favoring net bone formation and osteosclerosis rather than bone loss. In parallel, stromal osteolineage cells, including osteoblasts, are activated in response to aberrant JAK2V617F-driven hematopoiesis, promoting *de novo* bone formation and the pronounced osteosclerotic phenotype that characterizes advanced MF[32]. A recent comprehensive clinical study examined skeletal changes in patients with advanced MF before and after curative allo-HSCT, revealing important insights into osteosclerosis development and reversal[35]. Using high-resolution imaging, bone biopsies, and biochemical analysis, the authors demonstrated that patients with MF show marked increases in bone mineral density at central skeletal sites, which is histologically linked to severe bone marrow fibrosis and osteosclerosis. Importantly, successful allo-HSCT not only reversed marrow fibrosis but also led to rapid normalization of osteosclerosis, associated with recovery of systemic calcium homeostasis. Overall, the study provides direct evidence that

osteosclerosis in MF is a reversible, disease-associated skeletal remodeling process tightly linked to hematopoietic pathology and niche restoration following curative therapy.

Despite these advances, the systemic effects of inflammatory mutant hematopoietic cells on stromal behavior across different skeletal niches remain poorly understood. It is currently unclear whether stromal responses observed in long bones are conserved in other anatomical compartments or whether site-specific microenvironments exhibit unique pathological adaptations.

A recent study mapped blood-forming activity across the skeleton and revealed that the architecture and stress responses of hematopoiesis are not uniform across all bones[36]. Using imaging methods to visualize blood-cell production in situ, the authors defined discrete microanatomical production sites for different lineages that are maintained even under stress conditions such as hemorrhage, infection, or treatment with granulocyte colony-stimulating factor (G-CSF). Importantly, the study showed that distinct bone sites respond differently to the same challenge: for example, the tibia and sternum exhibited opposite changes in response to G-CSF, and the skull did not increase erythropoiesis after blood loss. These findings indicate that hematopoietic stress responses are heterogeneous across skeletal locations, suggesting that local niche environments confer site-specific plasticity in how blood production adapts to physiological insults.

Moreover, a complementary study indicated that ontogenetically distinct bones, such as craniofacial and long bones, respond differently to identical physiological or pathological injuries[37]. In contrast to long bones, the bone marrow within the skull expands throughout adult life and continues to contribute increasingly to systemic blood production, even as classical signs of niche aging (e.g. increased inflammatory cytokines, fat infiltration, and vascular deterioration) are largely avoided in this compartment. The skull's marrow also displays distinct responses to physiological changes (e.g., pregnancy) and pathological challenges (e.g., stroke or experimental leukemia) that differ markedly from those seen in long bones (e.g. femur), indicating that microenvironmental and functional properties vary substantially between developmentally distinct skeletal sites. These findings underscore fundamental

differences in how distinct marrow niches adapt to stress and aging, with implications for understanding site-specific hematopoietic regulation and disease progression.

In line with emerging evidence for site-specific bone marrow responses, skeletal complications are increasingly recognized as clinically relevant features of MF. Interestingly, evidence regarding osteoclast involvement in MPNs remains conflicting. Several studies suggest that osteoclasts in MF are intrinsically impaired, exhibiting reduced bone-resorptive capacity despite their increased presence within the bone marrow[34,35]. In contrast, epidemiological and association-based studies consistently report a positive correlation between myeloid malignancies and bone-destructive phenotypes, including osteoarthritis and osteolytic changes, which are further linked to fibrotic disease features with JAK2 and not CALR mutational status[38]. Moreover, bone marrow biopsies from patients with MF prior to allogeneic stem cell transplantation demonstrate a marked enrichment of osteoclasts compared with age-matched controls[35], supporting the notion of enhanced osteoclastogenesis in chronic disease. Together, these seemingly contradictory observations highlight a critical gap in understanding how malignant hematopoiesis and osteolineage stromal cells and the broader bone microenvironment reshape osteoclast function, potentially driving both: osteosclerosis and osteoporosis.

3.5 Periodontal tissue and periodontitis

The periodontal apparatus and alveolar bone constitute a highly specialized connective tissue system composed of multiple interacting cell populations that collectively maintain the structural integrity of the tooth-supporting unit, including the gingiva, cementum, periodontal ligament (PDL), and alveolar bone. The PDL forms a dynamic interface between the tooth root and the surrounding alveolar bone, enabling mechanical support and tissue homeostasis. Periodontitis is one of the most common chronic inflammatory diseases and is characterized by progressive destruction of the supporting tissues, resulting in alveolar bone loss and tooth instability[39]. Beyond its local effects, periodontitis is associated with persistent low-grade systemic inflammation, reflected by elevated circulating inflammatory mediators. These include pro-inflammatory cytokines, increased peripheral leukocyte counts, prostanoids,

matrix-degrading enzymes such as matrix metalloproteinases, and acute-phase proteins, all of which contribute to tissue breakdown and disease progression.

Experimental models demonstrate that chronic periodontitis not only triggers local tissue destruction but also induces persistent epigenetic reprogramming of hematopoietic stem and progenitor cells in the bone marrow[40]. This “maladaptive trained immunity” primes HSCs toward enhanced myelopoiesis and heightened inflammatory responsiveness, which can be transmitted through bone marrow transplantation and exacerbates secondary inflammatory stimuli, indicating that periodontal inflammation can have lasting effects on systemic hematopoietic function.

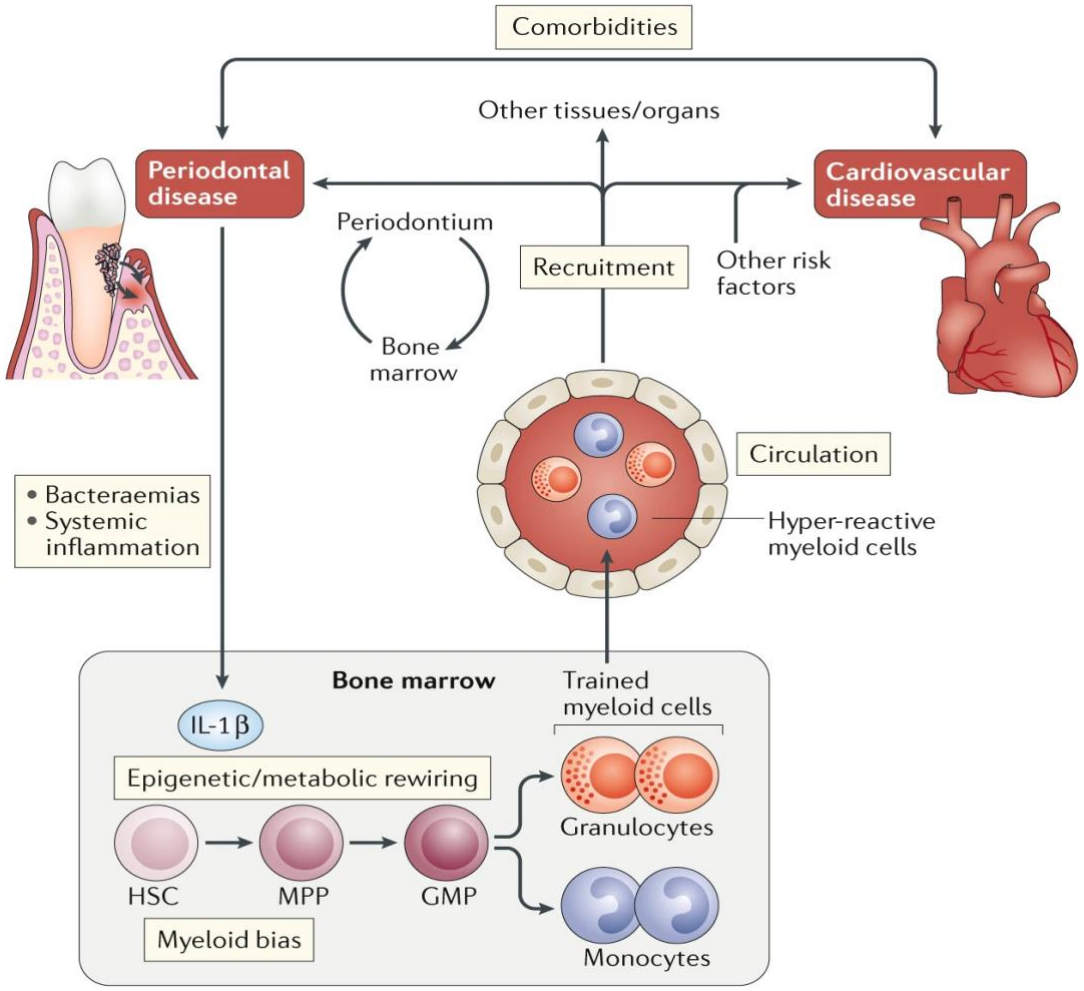

Figure 5: Systemic mechanism linking periodontitis-associated trained innate immunity and inflammatory comorbidities.

Periodontitis-driven inflammatory cytokines such as IL-1β can act on the bone marrow to induce durable metabolic and epigenetic reprogramming of hematopoietic stem cells. These inflammation-adapted HSCs preferentially expand and generate myeloid-biased progenitors, leading to the production of hyper-responsive neutrophils and monocytes. Upon recruitment

to peripheral tissues, including the periodontium, these trained myeloid cells can amplify local inflammation and contribute to periodontitis and related inflammatory comorbidities. Figure adapted from Hajishengalis and Chavakis[41].

Periodontitis is associated with cancer[42]. Clinical observations in patients with myeloid malignancies indicate that high disease burden is associated with disrupted periodontal and dental homeostasis[43]. Remarkably, periodontal inflammation in these patients can resolve following chemotherapy alone, even in the absence of targeted periodontal intervention[44,43]. This clinical reversibility supports the notion that suppression of mutant hematopoietic clones and attenuation of systemic inflammation are sufficient to restore malignancy-driven periodontal tissue homeostasis, highlighting a direct link between hematopoietic pathology and oral health.

Even pre-leukemic conditions might affect periodontium. Insights from studies of CHIP further demonstrate that premalignant hematopoietic states can actively exacerbate inflammatory bone pathology. In particular, DNMT3A-mutant CHIP has been shown to accelerate experimental models of arthritis and periodontitis by enhancing inflammatory osteoclastogenesis and impairing tissue repair mechanisms[45]. These findings suggest that mutant, myeloid-biased hematopoietic clones can directly contribute to the pool of functionally active bone-resorbing osteoclasts. Arthritis and periodontitis, two highly prevalent inflammatory disorders characterized by bone loss, appear to share mechanistic features driven by maladaptive trained myelopoiesis and sustained systemic inflammation.

3.6 Aims of the thesis

MPNs are increasingly recognized as systemic diseases in which mutant hematopoiesis profoundly reshapes the bone and stromal microenvironment in distinct organs. Emerging evidence further suggests that chronic inflammatory conditions, such as periodontitis, may engage in bidirectional crosstalk with pre-leukemic conditions. However, how these processes intersect across distinct skeletal sites and tissue compartments with the focus on stromal cells remains poorly understood. This thesis aims to address these knowledge gaps through the following objectives:

Aim 1: To determine whether JAK2V617F-mutant MPN can give rise to periodontitis.

While MPNs are associated with systemic inflammation and skeletal abnormalities, it is unknown whether JAK2V617F-mutant hematopoiesis alone is sufficient to induce naturally occurring periodontal disease. Establishing this link would provide direct evidence that hematological malignancies can drive inflammatory pathology in distant, non-hematopoietic tissues.

Aim 2: To elucidate the mechanisms underlying bone remodeling in MF, with a focus on underrepresented osteoclasts and osteochondral stromal cells. Myelofibrosis is characterized by severe osteosclerosis and fibrosis, yet the relative contributions of osteoclasts versus aberrant stromal osteolineage differentiation remain unclear. Moreover, the role of osteochondral stromal cells in MF-driven bone disease are almost entirely neglected. Dissecting these mechanisms is essential to understand how malignant hematopoiesis disrupts bone homeostasis and whether hematopoietic clone-stromal crosstalk yields in two opposing skeletal outcomes: osteosclerosis and osteoporosis.

Aim 3: To identify mechanistic targets that drive pathological bone remodeling in MF.

By integrating cellular, molecular, and spatial analyses, this aim focuses on uncovering signaling pathways and cell–cell interactions that mediate MF-driven remodeling. Defining actionable mechanisms underlying stromal remodeling in ontogenetically-distinct bones may reveal therapeutic targets capable of restoring systemic bone homeostasis.

Aim 4: To define ontogeny-dependent bone remodeling responses in MF by comparing neural crest–derived jawbones with mesoderm-derived long bones. The embryonic development of the skeleton is a tightly regulated process, where distinct origins of stromal cells give rise to anatomically different skeletal sites: neural crest-derived stromal cells form clavicle and craniofacial bone, while mesodermßderived stromal cells form axial and appendicular bone. Yet, how the ontogeny of the stromal cells dictates the bone outcome in cancer is not known. Investigating how these ontogenetically distinct bones respond to the same hematopoietic insult in myeloid malignancy will clarify whether skeletal origin dictates niche vulnerability and remodeling outcomes in MF.

Aim 5: To assess whether the two major periodontal compartments, the maxilla and mandible, exhibit distinct pathological responses to hematological malignancy.
Despite their anatomical proximity, clinical observations show the preferential affect of the maxilla (and not the mandible) in response to systemic diseases. Understanding whether these tissues respond differently to MPN-driven inflammation may reveal site-specific disease mechanisms relevant to dental complications.

Aim 6: To investigate whether experimental periodontitis reciprocally exacerbates JAK2V617F-mutant hematopoiesis and accelerates fibrosis.
Chronic periodontal inflammation has been shown to reprogram hematopoietic stem cells toward inflammatory myelopoiesis. This aim tests the hypothesis that periodontitis not only results from MPN-associated inflammation but may also feed back to accelerate mutant clonal expansion and disease progression.

Aim 7: To establish a three-dimensional human *in vitro* model to study organ crosstalk between periodontal inflammation and MPN pathology.
In vivo systems are limited in their ability to dissect human-specific mechanisms of tissue–tissue communication. Developing a 3D human model will enable controlled investigation of how inflammatory periodontal disease affects malignant hematopoiesis, providing a translational platform to study human organ interaction.

4 Materials and methods

4.1 Ethics approvals for human samples

Whole-body PET/CT images of the myelofibrosis patients were provided from the University Medical Center Hamburg-Eppendorf with the ethics approval number 2022-100964-BO-ff. More detailed information on patient characteristics can be found in the Supplementary Table 1.

Retrospective CT images of the femur heads and jawbones of the MPN patients were provided by the Department of Diagnostic and Interventional Radiology of the RWTH Aachen University with the ethics approval number EK028/19. More detailed information on patient characteristics can be found in the Supplementary Table 2.

For single cell studies, primary cell isolation and formalin-fixed paraffin-embedded (FFPE) tissues from bone marrow biopsies and teeth only excess material was used. In accordance with the approval from the ethics committee of the Medical Faculty of the RWTH Aachen University (EK24-409 and EK374/19) all patient material was de-identified at inclusion. Unprocessed bone marrow biopsies and extracted teeth were obtained approximately 2h after successful sample acquisition via the Department of Hematology, Oncology, Hemostaseology and Stem Cell Transplantation, the Department of Oral and Maxillofacial Surgery as well as the Department of Orthodontics in the Faculty of Medicine of the RWTH Aachen University. More detailed information on patient characteristics can be found in the Supplementary Table 3.

FFPE bone marrow biopsies and peripheral blood plasma of MPN and healthy donors were provided by the Laboratory of Stem Cells and Cancer Biology, Division Oncology and Hematology, HOCH Health Ostschweiz with the approval from the ethics committee of Ostschweiz (EKOS 23/022). Informed consent was obtained from all participants and/or their legal guardian/s. All samples were retrospectively collected. All MPN patient biopsies were taken from the pelvic bones. Healthy donor samples were obtained from either hip surgery or non-hematological malignant samples.

Human iPSCs generated from the peripheral blood mononuclear cells of either healthy or MPN patients were used. iPSC work was approved by the ethics committee of the Medical Faculty of RWTH Aachen University (EK206/09). Healthy donor-derived iPSC line HD353.6 was characterized and provided by Dr. Jitske Jansen as part of

collaboration. MPN iPS cell lines derived from a PV patient (age: 47; gender: male; disease type: Polycythemia vera; mutation: JAK2V617F^{hom}; allele-burden: 96%; sample type: Peripheral blood) using JAK2$^{V617F/V617F}$ PV2021 and isogenic CRISPR/Cas9 repaired JAK2$^{WT/WT}$ PV2072 clones as previously described[46].

4.2 Clinical imaging

4.2.1 Positron emission tomography/computed tomography (PET/CT)

Radiographic measurements were analyzed retrospectively in MPN patients (N=7). A detailed patient cohort is described in the Supplementary Table 1. ^{18}F-FDG PET/CT scans of MPN patients were acquired as part of a clinical workup to assess for presence of extramedullary disease before alloHSCT at the University Medical Center Hamburg-Eppendorf between 2012 and 2017. Imaging was performed using a standard whole-body protocol with Gemini GXL10 scanner (Philips) as described before[47]. All control subjects were imaged in the Department of Nuclear Medicine at the RWTH Aachen Medical Faculty with a clinical PET/CT system (*i.e.*, Biograph Vision 600, Siemens Healthineers, Knoxville USA) for suspicion or first staging of lung carcinoma. Under euglycemic conditions 2,5 MBq/kg of FDG were injected in a 0,9% saline solution *via* a peripheral venous catheter. The PET/CT scan was initiated ca. 60 minutes after tracer injection starting with the CT. CT acquisition settings: standard low dose protocol with 35 mA and 120 kVp, with CARE Dose4D and CAREkV enabled to decrease the radiation dose. CT images were reconstructed using a sinogram affirmed iterative reconstruction algorithm (*i.e.*, SAFIRE) to a voxel size of 1,52 × 1,52 × 2,5 mm^3 in a 512 × 512 matrix. Using a vendor software, CT values were converted into Hounsfield units (HU) using the formula:

$$HU = 1000 \times ((\mu_t - \mu_w) / (\mu_w - \mu_a),$$

where μ_w is the linear attenuation coefficient of water, μ_a is the linear attenuation coefficient of air and μ_t is the linear attenuation coefficient of the tissue. Immediately after the CT, a static PET acquisition was acquired with an axial field of view of 263 mm using continuous-bed motion (*i.e.*, FlowMotion®) with a bed speed of 1,4 mm/s (*i.e.*, equivalent to approximately 100 s/bed position). PET data were reconstructed iteratively using 3-dimensional ordinary Poisson ordered subset expectation maximization (*i.e.*, 3D-OP-OSEM with 4 iterations and 5 subsets) using vendor-

recommended settings (*i.e.*, PSF, TRueX and ToF (UltraHD-PET) enabled at zoom of 1x) to a voxel size of 1,65 × 1,65 × 2,50 mm^3 in a 440 × 440 matrix. Smoothing using a Gaussian filter of 2,00 mm full width at half maximum was automatically applied.

PMOD software package version 4.4 (PMOD Technologies LLC, Zürich, Switzerland) was used to view, render, and analyze the PET/CT data. As organs of interest the following bones were selected and further segmented: the left femoral head, the proximal and distal parts of the left femur, the entire mandible, the entire maxilla, the left humeral head, the proximal and distal parts of the left humerus as well as the proximal part of the tibia. Initially, those regions were manually masked as seen on CT. Afterwards, a CT-based automatic isocontour was generated using +500 HU as the minimal threshold to segment the bone structure. To segment the bone marrow a second automatic isocontour was generated using +500 HU as the maximal threshold. Upon completion of all target volumes of interest, the average, the maximum as well as the average of the top 5 hottest voxels was recorded both for the PET (in standardized uptake values, SUV) and CT data (in Hounsfield units, HU). All VOIs were drawn by a blinded member of our team, in order to exclude analysis bias. The analysis was done with the help of Dr. Alexandru Florea from the Department of Nuclear Medicine at RWTH Aachen University as part of collaboration.

4.2.2 Computed tomography (CT)

For the radiological analysis, CT datasets were retrospectively retrieved from the institutional picture archiving and communication system (PACS). A patient cohort with confirmed myeloproliferative neoplasms (MPN; $n = 34$) was analyzed. All available CT examinations were considered, including both non-contrast and contrast-enhanced scans. Image evaluation was consistently performed using bone window settings. Bone density assessment was performed using the PACS software (Philips VUE PACS). Regions of interest were manually placed in the trabecular bone of the femoral neck and the alveolar bone of the mandible and/or maxilla, following a standardized protocol analogous to previously published approaches[35]. Mean attenuation values expressed in Hounsfield units (HU) were recorded for each ROI. Where applicable, multiple measurements per site were obtained and averaged. Data was analyzed by Dr. Aleksandar V. Kargaliev from the Department of Diagnostic and Interventional Radiology, RWTH Aachen University as part of collaboration.

4.3 United Kingdom Biobank (UKBB) study

We analyzed data from the UKBB, a population-based cohort of ~500,000 participants aged 40–69 years recruited between 2006 and 2010. All participants provided informed consent, and the study was approved by the Northwest Multi-center Research Ethics Committee. Analyses were performed under UKB application 245437. MPN was defined using hospital episode statistics from ICD-10 code D47 and chronic periodontitis from ICD-10 code K05, capturing lifetime-risk for the phenome-wide association analysis (PheWAS), and secondly, we restricted outcomes to musculoskeletal and digestive diagnoses for MPN patients and neoplasms for chronic periodontitis patients. Data was provided by Prof. Carolin V. Schneider from the Department of Gastroenterology, Metabolic Diseases, and Intensive Care, RWTH Aachen University as part of collaboration.

4.4 Murine studies

4.4.1 JAK2 model studying the effect of MPN on the periodontal niche

Animal procedures using JAK2 knock-in model were approved by the Animal Care and Use Committee (German Regierungspräsidium Karlsruhe für Tierschutz und Arzneimittelüberwachung, Karlsruhe, Germany) under approval number G247/18 and G150/23. Mice were maintained in individually ventilated cages under specific pathogen-free (SPF) conditions at the German Cancer Research Center (DKFZ, Heidelberg). This murine experiment was conducted by Dr. Ian Ghezzi from the Division of Experimental Hematology, German Cancer Research Center as part of collaboration.

To generate the tamoxifen-inducible JAK2V617FxRosaCreERT1 knock-in mouse model, JAK2-V617F$^{fl/wt}$ mice were crossed with RosaCreERT+/- mice. Littermate pups without the mutation (JAK2WT) were used as control mice. For transplantation experiments, regular C57BL/6J mice (purchased from Janvier Laboratories) were used as recipients. CD45.1+ C57BL/6J background mice were used to create transgenic lines, while competitor C57BL/6J CD45.1+/ CD45.2+ mice were generated by crossing CD45.1+ C57BL/6J mice with C57BL/6J mice.

Bone Marrow Transplantation

Recipient mice were lethally irradiated with two rounds of 500 Rad. 24 hours later, mice were transplanted via i.v. injection with $3x10^6$ whole BM cells derived from JAK2V617F;RosaCre or CrexRosaCre donor mice, together with $3x10^6$ WT CD45.1+/CD45.2+ competitive whole BM cells (1:1 ratio).

4.4.2 Flow cytometry of murine hematopoietic cells

Peripheral blood was collected from the facial vein into EDTA-coated tubes and analyzed using a ScilVet abc Plus veterinary blood cell counter (Scil GmbH). Bone marrow was harvested in RPMI + 2% FCS by isolating, cleaning and crushing the bones. Cell suspensions were filtered through a 40 µm cell strainer, centrifuged and resuspended in ACK buffer (Lonza, #10-548E) or Pharm Lyse Buffer for RBC lysis (BD, #555899) for 10 minutes at room temperature (RT). After washing, cell suspensions were stained using the following antibody panels (Tables 1-3). Cells were analyzed by flow cytometry using FACSymphony™ A5 SE Cell Analyzer and LSR Fortessa. Data was analyzed using FlowJo software (FlowJo, LLC, Ashland, OR 97520).

Antibody	Fluorochrome	Clone	Catalogue	Company
F4/80	Pe-Cy7	BM8	1215570	Sony Biotechnology
CD11b	APC	M1/70	101212	Biolegend
Gr1	AF700	RB6-8C5	108421	Biolegend
CD3	PE	17A2	1000206	Biolegend
CD41	APC-Cy7	MWReg30	133928	Biolegend
B220	PB	RA3-6B2	103227	Biolegend
CD45.1	BV605	A20	110738	Biolegend
CD45.2	PerCP-Cy5.5	104	109828	Biolegend
GFP				

Table 1: Immune panels on murine peripheral blood cells.

Antibody	Fluorochrome	Clone	Catalogue	Company
GFP				
MHCII	PerPC-Cy5.5	M5/114.15.2	107625	Biolegend
CD45.2	PE	104	110707	Biolegend
Ly6G	PE-CF594	1A8	562700	BD
CD19	Pe-Cy5.5	6D5	1575-16	Southern Biotech
CD41	Pe-Cy7	MWReg30	133916	Biolegend
F4/80	APC	BM8	123116	Biolegend
Ly6C	AF700	HK1.4	128023	Biolegend
CD45.1	APC-Cy7	A20	110716	Biolegend

Ter119	PB	TER-119	116232	Biolegend
DAPI	PB	Dapi	422801	Biolegend
CD3	BV605	145-2C11	563004	BD
CD11b	BV711	M1/70	101242	Biolegend
CCR2	BV786	475301	747966	BD

Table 2: Immune panel on murine bone marrow-derived cells.

Antibody	Fluorochrome	Clone	Catalogue	Company
GFP				
Sca1	PerCP-Cy5.5	E13-161.7	122524	Biolegend
CD34	PE	SA376A4	152204	Biolegend
CD150	Pe-Cy7	TC15-12F12.2	115914	Biolegend
c-kit	APC	2B8	105812	Biolegend
CD45.2	AF700	104	560693	BD
CD48	APC-Cy7	HM48-1	103432	Biolegend
DAPI	PB	Dapi	422801	Biolegend
CD3	PB	17A2	100214	Biolegend
CD11b	PB	M1/70	101224	Biolegend
B220	PB	RA3-6B2	103227	Biolegend
Gr1	PB	RB6-8C5	108430	Biolegend
Ter119	PB	TER-119	116232	Biolegend
CD45.1	BV605	A20	110738	Biolegend
CD16/32	BV785	Ab93	740851	BD

Table 3: Murine bone marrow-derived hematopoietic stem and progenitor panel.

4.4.3 *In vivo* treatments

In order to knock in JAK2V617F, primary donor JAK2V617F-LRC mutant mice (JAK2-V617Ffl/wt x RosaCreERT+/- x SCLtTA+/- x H2BGFP+/-) or wild-type Cre-Control mice (JAK2-V617Fwt/wt x RosaCreERT+/- x SCLtTA+/- x H2BGFP+/-) were injected i.p. with 2mg tamoxifen (Merck, #T5648) in 200µL solvent (90% sunflower oil + 10% ethanol). 4 weeks after the last tamoxifen injection, the donor mice were sacrificed by cervical dislocation to collect the cells needed to perform transplantation experiments. Pharmacological treatments started at 16 weeks post transplantation. For pharmacological treatments, fedratinib (120 mg/kg, HY-10409A, MCE) was dissolved in vehicle solution (0.5% methylcellulose + 0.05% Tween-80 in water) and administered to mice via oral gavage daily, 5 days/week. LSKL (30mg/kg, #HY-P0299, MCE) was dissolved in vehicle solution (0,9% NaCL) and administered via i.p., 3 times/week, for either 4 or 8 consecutive weeks.

4.4.4 Thrombopoietin overexpression model

Thrombopoietin (ThPO) overexpression model in TdTomato+ recipients was used from the previously published cohort[33].

4.4.5 JAK2 knock-in model to study the effect of experimental periodontitis on mutant hematopoiesis

Animal procedures using JAK2 knock-in model together with periodontitis model were approved by the Animal Care and Use Committee (Landesamt für Verbraucherschutz und Ernährung NRW) under approval number 81-02.04.2023.A120. Mice were maintained in individually ventilated cages under specific pathogen-free (SPF) conditions at the University Hospital RWTH Aachen.

To generate the tamoxifen-inducible JAK2xHSC-SCL-CreERT knock-in mouse model, JAK2 mice were crossed with HSC-SCL-CreERT (JAX stock #037466, the Jackson Laboratory) mice. Littermate pups without the mutation (JAK2WT) were used as tamoxifen-inducible control mice.

Bone marrow transplantation

JAK2-HSC-SCL-CreERT CD45.2 (JAK2V617F and JAK2WT) donor animals aged 8 weeks or older received intraperitoneal injections of tamoxifen three times at two-day intervals. Tamoxifen was prepared at a concentration of 20 mg/ml in corn oil supplemented with 3% ethanol (EtOH), corresponding to a dose of 100 µg/g body weight (BW). The maximum injection volume did not exceed 10 ml/kg body weight. Donor animals were sacrificed approximately three weeks after the first tamoxifen injection, once recombination was considered complete.

C57BL/6J WT recipient mice received two sublethal irradiation doses of 6.02 Gy each, administered 4 hours apart. The dose rate was 0.86 Gy/min, resulting in an irradiation time of 7 minutes per session. Irradiation was performed using the Faxitron CP-160 system. Meanwhile, donor mice were euthanized by cervical dislocation for the isolation of cKIT+ hematopoietic stem and progenitor cells (HSCs) using MACS CD117 beads (#130-091-224, Miltenyi Biotech).

For transplantation, 5×10^5 hematopoietic stem and progenitor cells (c-kit$^+$ cells) were resuspended for injection. The transplanted cell population consisted of 20% CD45.2$^+$ JAK2-HSC-SCL-CreERT cells and 80% CD45.1$^+$ C57BL/6J wild-type competitor cells.

Cells were prepared in an injection volume of 5 ml/kg body weight, corresponding to 125 µl for a 25 g mouse. Transplantation was performed via retro-orbital injection. Transplanted mice received drinking water supplemented with sulfamethoxazol/trimethoprim (#17550590, Ratiopharm) for 3 weeks post-transplantation. Peripheral blood was obtained every two weeks from Vena facialis as described above.

4.4.6 Orthodontic tooth movement model

Eight weeks after the bone marrow transplant, mice were exposed to the orthodontic tooth movement model to mimic periodontal inflammation. For insertion of the NiTi coil spring, animals were positioned in a supine position on a custom-made surgical bed. The maxilla was immobilized using a filament placed between the upper incisors and molars and secured across the palate, thereby extending the head downward to allow easy access to the oral cavity. This procedure was performed according to a modified method previously described[48,49]. Briefly, mice were anesthetized with isoflurane, and a NiTi coil spring delivering a force of 0.25 N was inserted. The appliance consisted of a tensioned closed-coil spring (0.012-inch nickel–titanium wire; Dentaline GmbH), which was ligated between the upper left first molar and the upper incisors using a dental composite restoration. In a split-mouth design, the first molar in the right maxilla served as the contralateral control. The appliance generated force in a mesial (anterior) direction, resulting in mesial tipping of the first molar. Coil spring was placed for three weeks with a weekly dental check-up if needed.

Flow cytometry of murine hematopoietic cells

Single-cell suspensions were prepared from murine bones and filtered through a 70-µm mesh to remove debris. Red blood cells were lysed using standard lysis buffer (#555899, BD), followed by washing in a staining buffer (PBS supplemented with 5% FCS and 2mM EDTA). Cells were counted and aliquoted into FACS tubes. Cells were then stained for extracellular markers in the staining buffer for 30 min at 4°C protected from light. Table 4 summarizes the immune panel for peripheral blood and bone marrow-derived cells.

Antibody	Fluorochrome	Clone	Catalogue	Company
TER119	FITC	TER119	116206	Biolegend

CD45.2	PE	104	110707	eBioscience
Ly6G	PE-CF594	1A8	562700	BD
CD19	Pe-Cy5.5	6D5	1575-16	Southerm Biotech
CD115	Pe-Cy7	AFS98	135524	Biolegend
CD41	APC	MWReg300	133914	Biolegend
Ly6C	AF700	HK1.4	128024	Biolegend
CD45.1	APC-Cy7	A20	110716	Biolegend
CD47	BV421	miap301	127527	Biolegend
CD3	BV605	145-2C11	563004	BD
CD11b	BV711	M1/70	101241	Biolegend
MHC II	BV785	M5/114.15.2	107645	Biolegend

Table 4: Murine bone marrow and peripheral blood-derived immune cell panel.

For the intracellular staining, following surface staining, cells were fixed using BD Phosflow™ Fix Buffer (#558049, BD) according to the manufacturer's instructions (10 min at 37°C). Fixed cells were washed and permeabilized using a BD Phosflow™ Perm Buffer III (#558050, BD) suitable for phospho-protein detection. For Perm Buffer III–based protocols, cells were permeabilized on ice for 30 min, followed by washing in the staining buffer.

For intracellular phospho-flow staining, permeabilized cells were incubated with fluorochrome-conjugated antibodies against phosphorylated signaling proteins (pSTAT3 [Y705], pSTAT5 [Y694]) for 30 at room temperature protected from light. Cells were then washed thoroughly to reduce background and resuspended in the staining buffer for acquisition. Table 5 summarizes the intracellular HSPCs panel.

Antibody	**Fluorochrome**	**Clone**	**Catalogue**	**Company**
CD3	PB	17A2	100214	Biolegend
CD11b	PB	M1/70	101224	Biolegend
B220	PB	RA3-6B2	103227	Biolegend
Gr1	PB	RB6-8C5	108430	Biolegend
CD48	BV510	HM48-1	563536	BD
CD45.1	BV605	A20	747743	BD
Sca1	BV711	E13-161.7	744326	BD
GFP				
CD117	RB705	2B8	570567	BD
CD34	PE	SA376A4	BDRC:24056: 152204	BD
pSTAT3	PE-CF594	4/P-STAT3 (Y705)	562673	BD
CD16/32	RY703	2.4G2	770499	BD
CD45.2	RY775	104	770242	BD
pSTAT5	AF647	47/Stat5	562076	BD

		(pY694)		
CD150	R718	Q38-480	567735	BD

Table 5: Murine bone marrow-derived hematopoietic stem and progenitor cells with intracellular phospho-Flow antibodies.

4.5 Histological and immunohistological stainings

Murine organs were fixed in 2% paraformaldehyde for 8h and transferred to 70% ethanol. Murine bones were decalcified in 0.5M EDTA for 7 (femur/tibia) and 21 (jaws) days, dehydrated, and paraffin embedded. H&E was performed according to established routine protocols and reticulin staining was performed using the Reticulin silver plating kit according to Gordon & Sweets (Merck, #1.00251) on 5µm sections.

TRAP staining was performed on FFPE bones using a leukocyte acid phosphatase (TRAP) kit (387A, Sigma-Aldrich, Steinheim, Germany) as per manufacturer's instructions. The sections were then covered with Aquatex (1.08562.0050, Merck, Darmstadt, Germany).

For immunofluorescence stainings, samples were incubated in blocking solution (10% fetal bovine serum in PBS with 0.1% Triton X-100) for 1 h at room temperature. Primary antibodies with rabbit anti-COMP (Abcam, #ab231977, 1:50 dilution) were diluted in PBS with 1% fetal bovine serum and incubated overnight at 4 °C. Next, slides were washed 3–5 times in PBS in 5 min intervals. Species-specific Alexa Fluor-conjugated secondary antibodies AF-594 (Thermo Fisher Scientific, A11012) diluted 1:500 in PBS with 1% fetal bovine serum and 0.1% Triton X-100 were added and incubated for 1h at RT. Slides were washed 3–5 times in PBS in 5 min intervals. Nuclei were counterstained with DAPI (Sigma-Aldrich, D9542, 1:1,000 dilution). Coverslips were mounted with Entellan (Merck, #1.07961.0100).

For immunohistochemical analysis of Thrombospondin 1 (THBS1) on murine and human (MPN n=7, healthy n=3) FFPE tissues, antigen retrieval was performed using citrate-buffer in a conventional lab microwave (Vector, antigen unmasking solution). Sections were treated with 3% H2O2 and blocked with Avidin/Biotin blocking kit (Vector), and subsequently incubated with primary antibody (polyclonal goat anti-Thbs1, #PA5-142448, Invitrogen, 1:50 for murine and 1:100 for human samples) for 4◦C overnight. Sections were stained with secondary antibodies for 30 min at room temperature. Slides were incubated with AB complex for 30 min at room temperature, washed, and incubated for a further 10 min with DAB substrate. Slides were counterstained with hematoxylin and mounted with glass coverslip. Slides were

scanned using a PhenoCycler Fusion system (Akoya Biosciences). Images were exported as qptiff and analyzed using the QuPath software v. 0.5.0.

4.6 ELISA

ELISAs were performed on human plasma samples (MPN n=293, healthy donor n=74) with human CD47 (DY4670, Biotechne) and TSP1 (Thrombospondin-1, DY3074, Biotechne) DuoSet ELISA Kits as per the manufacturer's recommendations. Briefly, capture antibody was coated overnight, blocked with blocking buffer (reagent diluent buffer with 1% BSA and 2% FCS) for one hour, 4 times diluted samples were incubated for 2 hours, followed by the detection antibody for 2 hours and finally treated with the Streptavidin-HRP for 30 minutes. After that the TMB substrate was incubated for 20 minutes and 35 minutes for CD47 and TSP1, respectively, the reaction was stopped by adding the stop solution directly to the substrate without any washing step in between. The absorbance at 450nm was measured within 3 minutes after adding the stop solution. CD47 and TSP1 concentrations were calculated from the slopes of the respective standard curves. ELISA for Thbs1 and CD47 was performed by Chiara Stüdle from the Laboratory of Stem Cells and Cancer Biology, Division Oncology and Hematology, HOCH Health Ostschweiz as part of collaboration.

4.7 Murine micro-computed tomography

Femurs, maxillae, and mandibles were fixed in 2% PFA for 8h and scanned in 70% ethanol using a Skyscan 1272 micro-CT system (Bruker Micro-CT, Belgium) at 60 kV and 140 µA with a 0.25 mm aluminum filter, achieving an isotropic voxel size of 5 µm. Data were reconstructed in NRecon software (Bruker Micro-CT, Belgium). For analyses of comparable areas, the data were co-registered to one reference sample in DataViewer (Bruker Micro-CT, Belgium). Subsequently, multiple volumes of interest (VOIs) were defined for quantitative analysis in CTan(Bruker Micro-CT, Belgium).

For femoral specimens, distinct VOIs were established: (1) distal and proximal areas (1.5 mm and 6.5 mm length, respectively), (2) mid-diaphyseal cortical region (0.5 mm length), and (3) growth plate region in the distal femoral head (cylindrical VOI, 0.4 mm diameter × 1.0 mm height). The trabecular part of the femur was defined virtually using a cascade of opening and closing algorithms. The cortical compartment was defined

through ROI shrink-wrap algorithms following trabecular bone subtraction. Bone mineral density (BMD) values were calibrated using hydroxyapatite phantoms scanned under identical conditions. Cortical thickness was estimated after the subtraction of the trabecular region and using an identical algorithm for definition of trabecular thickness. Growth plate thickness was quantified within the cylindrical VOI using the same morphological approach. Femoral length measurements were obtained from the co-registered datasets.

Analysis of maxillary and mandibular specimens were performed in several VOIs: (1) alveolar bone of the first molar tooth socket (M1; 0.8 mm height in maxilla, 0.6 mm height in mandible), (2) alveolar bone between the first and the second molars (M1-2), (3) alveolar bone around the third molar (M3), and (4) periodontal ligament space of the first molar (PDL-1). Bone and periodontal ligament parameters were quantified using established algorithms as previously described[50]. For bone loss assessment, total bone volume was analyzed, incorporating both vertical bone loss and increased alveolar porosity. Periodontal ligament space thickness was determined using standardized trabecular thickness algorithms. Murine microßCT was analyzed by Dr. Marta Rizk from the Department of Orthodontics, RWTH Aachen University as part of collaboration.

4.8 Sequencing

4.8.1 FACS sorting and library preparation

Murine jaws were crushed and flushed using PBS/2%FCS and filtered through a 70µm nylon mesh. The remaining bone chips were digested in 1mg/mL Collagenase II (Thermo Scientific, #17101-015) and DNAse I (100µg/mL, Sigma-Aldrich) at 37 ◦C for 30 minutes. After pooling of the supernatant of the bone chips with the flushed fraction, cells were were stained with the antibodies described in Table 6.

Antibody	Fluorochrome	Clone	Catalogue	Company
CD45	APC-Cy7	30-F11	103116	Biolegend
Sca1	PerCP-Cy5.5	E13-161.7	122524	Biolegend
TER119	PB	TER119	116232	Biolegend
DAPI			422801	Biolegend

Table 6: FACS panel of the murine jawbone-derived cells for single cell RNA sequencing.

Murine jawbone cells were sorted based on the following expression patterns: DAPI-TER119-CD45+ (hematopoietic cells), DAPI-TER119-CD45-Sca1+ (stroma). Following sorting, the sorted populations were mixed at variable ratios, on a sample-to-sample basis, to ensure recovery of all main cell populations. The resulting cell suspension was centrifuged, resuspended in PBS/2%FCS and processed for scRNAseq (10X Genomics, protocol CG000315) using the manufacturer's procedure.

Patient iliac crest biopsies were crushed and flushed using PBS/2%FCS and filtered through a 70µm nylon mesh. The remaining bone chips were digested in Liberase TL (125µg/mL, Roche, for iliac crest biopsies) or 3mg/mL Collagenase I (LS004196, Worthington Biochemical, for teeth samples) and DNAse I (100µg/mL, Sigma-Aldrich) at 37 ◦C for 30 minutes, with gentle agitation. Following this incubation, supernatant was collected and strained through a 70µm nylon mesh. Bone chips were additionally washed twice with PBS/2%FCS before pooling it with the flushed fraction.

Isolated cells were resuspended in PBS/2%FCS and stained at 4 ◦C for 20 minutes using the antibodies described in Table 7.

Antibody	Fluorochrome	Clone	Catalogue	Company
CD34	PE	581	555822	BD
CD45	APC	HI30	555485	BD
CD3	PerPC-Cy5.5	UCHT1	560835	BD
CD19	BB700	SJ25C1	566396	BD
HLA-DR	Pe-Cy7	G46-6	560651	BD
CD235a	PB	HIR2	306612	Biolegend

Table 7: FACS panel of the human bone marrow biopsy-derived cells for single-cell RNA sequencing.

Then, cells were diluted in PBS/2%FCS and stained with Calcein Green (#C34852 Invitrogen, 1µM final) for 10 minutes at room temperature. After washing, cells were resuspended in 400µL of PBS/2%FCS and sorted using a BD FACS Melody. Cells from the iliac crest biopsies were sorted based on the following expression patterns: CD34+ (HSC-enriched), CD34- CD45- CD235a- (stroma-enriched) and CD34- CD45+ HLA-DR+ CD3- CD19- (mononuclear phagocyte-enriched).

Antibody	Fluorochrome	Clone	Catalogue	Company
CD45	BV786	HI30	563716	BD
CD235a	PB	GA-R2	306612	Biolegend
DAPI			422801	Biolegend
CD14	PeCy7	M5E2	557742	BD
CD3	PerCP-Cy5.5	UCHT1	560835	BD

CD66b	PE	G10F5	561650	BD
CD19	FITC	HIB19	555412	BD
CD11b	APC-Cy7	M1/70	561039	BD
CD90	APC	5E10	21270906X2	Immunotools

Table 8: FACS panel of the human teeth-derived cells for single cell RNA sequencing.

Cells from the human teeth samples were sorted based on the antibodies described in Table 8 with the following gating strategy: DAPI-CD235a-CD45+ (hematopoietic cells), DAPI-CD235a-CD45- (stroma). Following sorting, the sorted populations were mixed at variable ratios, on a sample-to-sample basis, to ensure recovery of all main cell populations. The resulting cell suspension was centrifuged, resuspended in PBS/2%FCS and processed for scRNAseq (10X Genomics, protocol CG000315 and CG000731) using the manufacturer's procedure.

All libraries were prepared using the Chromium Next GEM Single Cell 3' Reagent Kits (v3.1 and v4): Library Construction Kit and Gel Bead Kit (PN-1000268), Chromium Next GEM Chip G Single Cell Kit (PN-1000127) and Dual Index Kit TT Set A (PN-1000215), and following the Chromium Next GEM Single Cell 3' v3.1 and v4 (Dual Index) User Guide (CG000315, Rev F and CG000731, Rev B). Finalized libraries were sequenced on a Novaseq6000 platform (Illumina), aiming for a minimum of 20.000 reads/cell using the 10x Genomics recommended number of cycles (28-10-10-90 cycles).
Raw counts were aligned to mouse or human genome (mm10 or hg18) and quantified using 10x Genomics Cell Ranger (version 7.0.0).

4.8.2 Single cell RNA sequencing analysis

Single-cell RNA-sequencing data were processed using R (v.4.4.1) and Seurat (v.5.3.1). Cells failing general quality control (QC) thresholds, including low gene counts, low UMI counts, high mitochondrial gene content (>30%), or >50% ambient RNA (using decontX; Celda v 1.14.2), were excluded from downstream analyses.

After QC filtering, a total of 95,368 cells from human bone marrow and teeth samples were retained for analysis. For the mouse dataset, samples from the maxilla and mandible contained a total of 15,790 cells for downstream analysis. Data integration across samples was performed using Harmony (v.1.2.4) to correct for batch effects and doublets were identified and removed using DoubletFinder (v. 2.0.6). The integrated dataset was visualized using UMAP. Cell type annotation was performed

manually based on the expression of known marker genes. Subclustering was conducted for selected populations when higher resolution was required. Cell type prioritization between conditions was performed using Augur (v. 1.0.3). Differential gene expression analysis between control and diseased samples was carried out in a pseudobulk aggregation approach with DESeq2 (v.1.44) using the Wald test. Genes identified as differentially expressed were subjected to pathway enrichment analysis using Reactome (R.), Gene Ontology (GO), WikiPathways (WP), KEGG, BioCarta, and PID databases. Enrichment significance was evaluated using the fgsea permutation-based enrichment test. Differences in gene and module scores expression between conditions were tested using an unpaired two-sided Wilcoxon rank-sum test, and significance was reported using p-values (non-significant comparisons not shown).

Cell–cell communication analyses were performed using CellChat, and interactions were filtered to those supported by ≥10 cells per group. Statistical significance was assessed using bootstrap resampling (nboot = 100). Global cell–cell interaction changes were summarized using heatmaps based on the delta probability of interaction. Selected cell–cell interactions were visualized using alluvial plots, in which the delta interaction probability was explicitly represented to highlight condition-specific signaling changes. For the human dataset, an intra-patient comparison was conducted to identify differences in signaling between bone marrow and teeth samples. For these analyses, delta–delta interaction probabilities were calculated and reported to quantify tissue-specific changes in signaling.

For the mouse dataset, trajectory inference was performed using Slingshot (v.2.12.0), with inferred lineages visualized by overlaying trajectories on LAP reduction plots. Condition-specific dynamics were further visualized using stream plots, with pseudotime values normalized across conditions. Transcription factor activity analysis was performed using decoupleR (v.2.10.0), leveraging the CollecTRI database to infer regulatory activity. Gene module scores were computed for predefined gene sets curated from the literature. Single cell RNA sequencing was analyzed by Dr. Hector Tejeda Mora from the Department of developmental Biology, Erasmus MC as part of the collaboration.

4.8.3 Spatial transcriptomics

Visium CytAssist spatial transcriptomics data from tibial sections were obtained from our previously published work[33] and reanalyzed in this study. Experimental procedures, including FFPE section processing, hematoxylin–eosin staining, image acquisition, library preparation, and sequencing on an Illumina NovaSeq platform, were performed as previously described. Brightfield images were aligned to capture areas, and segmentation files were generated using Loupe Browser (v8.1.2, 10x Genomics). Raw sequencing data were processed with Space Ranger v3.0.0 to generate spot-level gene expression matrices.

Downstream analysis was performed in Python (v3.10.16) using Scanpy (v1.11.0) and Squidpy (v1.6.5). Spots with 200–7,500 total counts, mitochondrial transcript content >5%, or genes detected in fewer than 10 spots were excluded. Spatial neighbors were computed for each replicate, and Moran's I was used to identify genes with significant spatial autocorrelation (normalized $p < 1\times10^{-4}$) shared across all replicates. The filtered data were normalized to 10,000 counts per spot, log-transformed, scaled, and subjected to PCA. A k-nearest neighbor graph was constructed using 20 principal components and 15 neighbors, followed by Leiden clustering (resolution = 0.3). Differentially expressed genes were identified using a two-sided Wilcoxon rank-sum test, and clusters were mapped back onto tissue sections and annotated based on highly expressed genes. Spatial transcriptomics data was analyzed by Lina Schmidt from the Institute of Cell and Tumor Biology, RWTH Aachen University as part of the collaboration.

4.9 *Cell culture*

4.10 PDL fibroblast cell line

4.10.1 Immortalization and culture of PDL fibroblast cell lines

Human PDL cells (mandible, molar 38) were isolated from a 32 y.o. female patient. Primary human periodontal ligament (hPDL) cells were cultured from periodontal connective tissue, isolated from the middle root section of healthy human teeth. Only decay-free teeth from the patient, which needed to be extracted for medical reasons, were used for human PDL cell isolation. Immediately after extraction, the teeth were

transferred into an isolation medium of DMEM high-glucose (Gibco, Billings, MT, USA), 10% FetalBovine Serum (FBS), qualified heat-inactivated (Gibco), 50 mg/L ascorbic acid (Sigma, Saint Louis, MO, USA), antibiotic-antimycotic (Gibco) and stored at 4◦C until isolation was started within 24 h after extraction. For isolation, The PDL tissue, which is located on the lower three-fifths of the height of the root, was then scraped off and incubated in a solution of 2 mg/mL collagenase type I (Worthington Biochem, Freehold, NJ, USA) for 1.5 h at 37◦C. After incubation, cells were plated into 6-well plates. After the first splitting, the isolation medium was replaced by a culture medium of DMEM high-glucose (Gibco), 10 % FBS (Gibco), 50 mg/L ascorbic acid (Sigma), Penicillin/Streptomycin (Gibco). Primary PDL cells were immortalized with hTERT and SV40 Large T at passage 2. Immortalization and characterization of the PDL fibroblasts was done by Chloe Radermacher from the Institute of Pathology, RWTH Aachen University as part of the collaboration. Adherent PDL fibroblasts were cultured in PDL medium as illustrated in Table 9 and split approximately 2 times per week.

Reagent	Stock concentration	Final concentration	Catalogue Nr.	Company
DMEM high Glucose	1x		11965092	Gibco
Fetal calf serum	1x	10 %	12662029	Gibco
Penicillin/Streptavidin	100x	1 (100 U/mL)	P06-07100	PAN-Biotech
Sodium Pyruvate	100 mM	100 µM	11360070	Gibco
L-ascorbic acid	50 mg/mL	50 µg/mL	72132	Stemcell Technologies

Table 9: Composition of the PDL fibroblast medium.

4.10.2 2D inflammatory stimulation of PDL cell line

When adherent cells reached 80–90% confluency, they were split and 20,000 cells per well were seeded into six-well plates in PDL medium. After 24 h, the medium was replaced with starvation medium (PDL medium supplemented with 1% FCS) and cells

were cultured for an additional 24 h. At 48 h post-seeding, three wells per plate were stimulated with PDL medium containing 1% FCS supplemented with 10 ng/mL IL-1α, while control wells received fresh starvation medium without supplementation. After 24 h of stimulation, the medium was aspirated, cells were washed with PBS, and lysis was performed using the lysis buffer from the Invitrogen™ PureLink™ RNA Mini Kit (Thermo Fisher, #10307963), supplemented with β-mercaptoethanol at a 1:100 dilution. Lysates from each well were transferred into separate centrifuge tubes and stored at −80°C until RNA isolation. For 48 h stimulation experiments, starvation medium with or without 10 ng/mL IL-1α was renewed after the first 24 h. Following a total stimulation period of 48 h, cells were processed and lysed in the same manner as described for the 24 h samples. Subsequently, total RNA was extracted from all samples, followed by cDNA synthesis and quantitative real-time PCR (qPCR) analysis.

4.10.3 3D inflammatory stimulation of PDL cell line

Inflammatory 3D spheroids and corresponding non-stimulated control spheroids were generated following a protocol analogous to the 2D inflammatory stimulation of PDL cells. After reaching 80–90% confluency, adherent cells were passaged and reseeded at a density of 1×10^6 cells per 10 cm^2 dish in PDL medium and cultured for 24 h. Cells were then subjected to serum starvation for 24 h, followed by stimulation for an additional 24 h with 10 ng/mL IL-1α in starvation medium. Control cells received a fresh starvation medium without IL-1α. After the initial stimulation period, adherent PDL cells were detached and counted. A total of 2×10^6 cells were resuspended in 10 mL PDL medium containing 5% FCS, supplemented either with or without 10 ng/mL IL-1α, depending on the experimental condition. Subsequently, 100 µL of the cell suspension was seeded per well into a 96-well ultra-low attachment (ULA) plate. The plate was centrifuged at 350 × g for 5 min and incubated overnight to allow spheroid formation. Inflammatory PDL spheroids were either processed for qPCR analysis or used in microfluidic experiments.

4.11 Induced pluripotent stem cells (iPS cells)

4.11.1 Maintenance of iPS cells

Human induced pluripotent stem cells (iPS cells) were maintained on growth factor–reduced basement membrane matrix (Geltrex™, Gibco, #A1569601) in StemFlex™

basal medium (Gibco, #15627578) supplemented with 1x penicillin/streptomycin (PAN-Biotech, #P06-07100) at 37 °C and 5% CO_2. Medium was exchanged daily, and cells were passaged at 60–80% confluency either as single cells using Accutase (Pan Biotech, #P10-21500) or as small aggregates using EDTA-based dissociation. For single-cell passaging, the ROCK inhibitor Y-27632 (10 µM; Abcam, #129830-38-2) was added for the first 24 h after seeding to enhance cell survival.

4.11.2 Passaging of iPSCs as single cells

Once iPS cells reached 60–80% confluency, the culture medium was removed and cells were washed with phosphate-buffered saline (PBS). Subsequently, 1 mL of pre-warmed Accutase (37°C; PAN Biotech) was added for enzymatic dissociation. After 4 minutes of incubation, cells were gently resuspended in KnockOut Dulbecco's Modified Eagle Medium (KO-DMEM; Gibco, #10829018) and centrifuged at 350 × g for 4 minutes. The cell pellet was resuspended in 1 mL KO-DMEM and cell numbers were determined using the Countess 3 Automated Cell Counter. Cells were centrifuged again and resuspended in KO-DMEM supplemented with Y-27632 ROCK inhibitor (1:1000).

In parallel, a new 6-well plate was coated with 2 mL DMEM/F12 (Gibco, #11320033) containing 40 µL Geltrex per well and incubated at 37°C for 30 minutes. After removal of the coating solution, 2 mL StemFlex medium supplemented with Y-27632 ROCK inhibitor (1:1000) and penicillin/streptomycin (1:100) was added to each well. A total of 50,000 cells per well were then seeded dropwise and evenly distributed by gentle agitation. Following overnight incubation at 37°C, the medium was replaced with 2 mL StemFlex medium without Y-27632 ROCK inhibitor.

4.11.3 Passaging of iPSCs as colonies

At 60–70% confluency, iPS cells were passaged using an aggregate-based dissociation protocol. The culture medium was removed and cells were washed with PBS, as described for single-cell passaging. Subsequently, 700 µL PBS containing 0.5 mM EDTA was added to each well and incubated at 37°C for 4–5 minutes. Following incubation, the PBS/EDTA solution was carefully aspirated and replaced with 1 mL StemFlex medium supplemented with penicillin/streptomycin (1:100). Cell

aggregates were detached by gentle rocking of the plate. An aliquot of 300–1000 µL of the resulting cell suspension was transferred to a new Geltrex-coated 6-well plate. Each well was then topped up with a StemFlex medium containing penicillin/streptomycin (1:100) to a final volume of 2 mL per well.

4.11.4 Viral transduction of GFP and RFP for iPS cells

MPN patient–specific induced pluripotent stem (iPS) cell lines ($JAK2^{V617F/V617F}$ and CRISPR repaired isogenic $JAK2^{WT/WT}$, patient 2 with PV diagnosis, JAK2V617F variant allele frequency 96%) were generated as previously described[51,46]. GFP or RFP labeling of iPS cell lines was achieved using GFP- or RFP-expressing pWPXL lentiviral vectors produced in HEK293T cells with the psPAX and pMD2.G packaging plasmids. iPS cell cultures at 60–70% confluency were incubated overnight at 37 °C in a humidified atmosphere containing 5% CO_2 with a 1:1 mixture of iPS-Brew medium and viral supernatant supplemented with 8 µg/mL polybrene. Following transduction, iPS cells were expanded and sorted for GFP^+ or RFP^+populations using a BD FACSMelody™ cell sorter. Sorted cells were cultured on Laminin-521–coated plates (BioLamina) in the presence of a Rho kinase inhibitor (MedChem Express) for 24 h, followed by further expansion on Matrigel-coated plates. Viral transduction of iPS cells was performed by Dr. Marcelo A.S. de Toledo from the Department of Hematology, Oncology, Hemostaseology and Stem Cell Transplantation, RWTH Aachen University as part of the collaboration.

4.11.5 Cryopreservation of cells

After splitting of iPS cells, 1×10^6 cells were resuspended in 1 mL cryopreservation medium and transferred into 2 mL cryovials (Thermo Fisher Scientific). For iPS cells, the cryopreservation medium consisted of 90% fetal calf serum (FCS), 10% dimethyl sulfoxide (DMSO), and 10 µM Y-27632. For other cell lines, the cryopreservation medium contained 90% FCS and 10% DMSO. Cryovials were initially stored at −80°C and subsequently transferred to liquid nitrogen for long-term storage.

4.11.6 Thawing of cryopreserved cells

Cryovials were removed from either liquid nitrogen or the −80°C freezer and briefly thawed in a 37°C water bath until nearly completely defrosted. The cell suspension

was immediately transferred into 9 mL PBS supplemented with 2% FCS and centrifuged at 1,400 rpm for 4 minutes. After centrifugation, the supernatant was discarded and the cell pellet was resuspended in 10 mL fresh culture medium. The cell suspension was then seeded into a new 10 cm culture dish or, in the case of iPS cells, onto Geltrex-coated 6-well plates.

4.11.7 Differentiation of MPN iPSC-derived hematopoietic stem and progenitor cells

MPN patient–specific iPSC-derived hematopoietic progenitors were generated using a modified spin embryoid body (SpinEB) protocol as previously described[46,51,52]. Briefly, JAK2V617F PV2021 RFP+ and JAK2WT PV2072 GFP+ iPS cells were cultured on Geltrex-coated 6-well plates until they reached 60–70% confluency. On day 0 of the SpinEB protocol, cells were dissociated into a single-cell suspension and counted. A total of 350,000 cells were resuspended in 6 mL of “day 0” differentiation medium supplemented with bovine serum albumin (BSA) (Table 10) and the respective cytokines (Table 11). Subsequently, 50 µL of the cell suspension was seeded into each well of a 96-well U-bottom ultra-low attachment plate (Corning, #7007). The plate was centrifuged at 380 × g for 5 minutes to promote cell aggregation. Proper cell sedimentation and aggregation were confirmed by microscopic inspection to ensure successful initiation of embryoid body formation. Starting from day 2 onward, the media was refreshed daily with the removal of 50µL of the medium from each well and the addition of 50µL of the fresh medium with the double amount of cytokines.

On day 14, cells from the entire 96-well plate were collected. The harvested cells in the suspension medium were passed through a 70 µm cell strainer to obtain a single-cell suspension. To maximize cell recovery, each well was additionally rinsed with PBS prior to centrifugation at 350 × g for 4 minutes. The resulting cell pellet was resuspended in 1 mL FACS buffer (PBS supplemented with 5% FCS and 0.4% EDTA) and cell numbers were determined using the Countess 3 Automated Cell Counter. An aliquot of 150,000 cells was subsequently used for flow cytometric analysis employing the hematopoietic antibody panel (Table 12) and the remaining cells were used for HSPCs enrichment using CD34 UltraPure MicroBeads (Miltenyi Biotec, #130-100-453) as per manufacturer’s instructions.

Reagent	Stock concentration	Final concentration	Catalogue Nr.	Company
IMDM	1x	2.5	12440053	Gibco
Ham's F12	1x	2.5	11765054	Gibco
BSA detox.(day 0 only)	20 %	0.125	Home-made	
Chemically defined lipids	100x	0.05	11905031	Gibco
Glutamax	200 mM	0.05	35050061	Gibco
Monothioglycerol	100 mM	0.02	96-27-5	Sigma-Aldrich
Human Plasbumin (day 2-14)	20 %	1.75	B05AA01	Biotest

Table 10: Serum-free medium for the directed iPSC differentiation into HSPCs.

Reagent	Used on day	Stock conc.	Final conc.	Catalogue Nr.	Company
L-ascorbic acid	0-13	50 mg/mL	50 µg/mL	72132	Stemcell Technologies
h-Transferrin	0-13	17.5 mg/mL	6 µg/mL	11096-37-0	Sigma-Aldrich
FGF-2	0-7	100 µg/mL	10 ng/mL	100-18B	Peprotech
BMP-4	0-7	25 µg/mL	10 ng/mL	130-111-168	Miltenyi
Y-27632 (Rock inhibitor)	day 0 only	10 mM	10 µM	129830-38-2	Abcam
SCF	2-13	100x	1x	130-096-692	Miltenyi
VEGF	2-7	25 µg/mL	25 ng/mL	130-109-385	Miltenyi
Penicillin/Steptavidin	7-13	100x	1 (100 U/mL)	P06-07100	PAN-Biotech
IL-3	7-13	150	30 ng/mL	113400	Immunoto

		µg/mL		37	ols
Hyper IL-6	7-13	25 µg/mL	25 ng/mL	-	Stefan Rose-John, Kiel, Germany
M-CSF	7-13	100µg/mL	50ng/mL	300-25	Thermo Fischer

Table 11: Cytokine composition in the serum free medium for the directed differentiation of iPSCs into HSPCs.

Antibody	Fluorochrome	Clone	Catalogue	Company
CD45	BV786	HI30 (RUO)	563716	BD Bioscience
CD123	BV421	6H6	306018	Biolegend
CD34	BB700	581	555822	BD Bioscience
JAK2-donor	GFP			
CD41	PE-Cy7	HIP8	303718	Biolegend
JAK2V617F-donor	RFP			
CD235a	PE	HIR2 (GA-R2)	12-9987-82	eBioscience
CD38	APC-Cy7	HIT2	303534	Biolegend
CD90	APC	5E10	21270906X2	Immunotools

Table 12: iPSC-derived hematopoietic stem and progenitor cell panel from SpinEB-derived cells.

4.11.8 iPSC-derived bone marrow organoid differentiation

BM organoids were generated using the newly established HD353.6 line based on previously described protocol[53]. In brief, on day −1 of differentiation, the culture medium was removed and cells were washed with PBS. Subsequently, 1 mL PBS supplemented with 0.5 mM EDTA was added and incubated for 3–5 minutes at 37°C. The EDTA solution was carefully aspirated and replaced with 2 mL StemFlex medium supplemented with RevitaCell (1:100; Gibco, #A2644501). Gentle rocking of the plate facilitated detachment of cell aggregates, which were collected and passed through a 150 µm cell strainer. A total volume of 2 mL of the resulting cell suspension was

transferred into each well of a 6-well ultra-low attachment (ULA) plate, ensuring even distribution of aggregates. Cells were incubated for 24 hours at 37°C and 5% CO_2.

On day 0, aggregates were expected to exhibit a round morphology with well-defined borders. Aggregates were carefully harvested by collecting the medium into a 15 mL Falcon tube and centrifuged at 100 × g for 4 minutes at room temperature. The supernatant was aspirated, and the aggregates were gently resuspended in 8 mL phase I medium (Table 13) and redistributed evenly into the same 6-well ULA plate for continued differentiation.

Reagent	Stock concentration	Final concentration	Catalogue Nr.	Company
APEL2 medium	1x		05275	StemCell Technoogies
BMP4	25 µg/mL	50 ng/mL	130-111-168	Miltenyi
FGF2	100 µg/mL	50 ng/mL	100-18B	Peprotech
VEGF-A	25 µg/mL	50 ng/mL	130-109-385	Miltenyi
CHIR99021	5 mM	3 mM	SML1046-5MG	Merck

Table 13: Composition of Phase I medium for mesoderm induction (day 0-3) of the BM organoid differentiation.

On day 3, a medium change was performed comparable to day 0, but without a centrifugation step. Instead, aggregates were allowed to settle at the bottom of the tube by gravity for approximately 5 minutes. The supernatant was then carefully removed, and the aggregates were gently resuspended in phase II medium (Table 14). Subsequently, they were redistributed into the same 6-well ultra-low attachment (ULA) plate for continued culture.

Reagent	Stock concentration	Final concentration	Catalogue Nr.	Company
APEL2 medium	1x		05275	StemCell Technoogies
BMP4	25 µg/mL	50 ng/mL	130-111-168	Miltenyi
FGF2	100 µg/mL	50 ng/mL	100-18B	Peprotech
VEGF-A	25 µg/mL	50 ng/mL	130-109-385	Miltenyi

Murine SCF	10 µg/mL	25 ng/mL	250-03-10UG	Peprotech
FLT3L	25 µg/mL	25 ng/mL	300-19-250	Peprotech

Table 14: Composition of Phase II medium for hematopoietic and vascular commitment (day 3-5) of the BM organoid differentiation.

On day 5, to induce sprouting and vascularization, aggregates were embedded in a collagen hydrogel using a two-layer approach. Wells were pre-wetted with PBS, and the collagen mixture containing 60% collagen (collagen type I (Corning, #354236), collagen type IV (Cell Systems, #5022)) and 40% matrigel (Corning, #354230) was prepared on ice. Hydrogel diluent is described in Table 15. Polymerization was initiated by adding 1M NaOH to adjust the pH to 7.2. After removing PBS, 500 µL of the hydrogel solution was added per well and allowed to polymerize at 37°C for 90–120 minutes.

Reagent	Stock concentration	Final concentration	Catalogue Nr.	Company
Ham's F12	1x	69.6 mL	11765054	Gibco
Glutamax	100x	1.5 mL	35050061	Gibco
Sodium Bicarbonate	7.5 %	3.34 mL	25080094	Gibco
HEPES	1 M	4.2 mL	15630080	Gibco
10x DMEM	10x	20.86 mL	BS.F0455	Bio&Cell

Table 15: Composition of the hydrogel diluent for day 5 of BM organoid embedding.

Aggregates were then collected by gravitational settling (~5 minutes), the medium was aspirated, and a second hydrogel layer was prepared as described above. Aggregates were gently resuspended in the collagen matrix, and 500 µL of the hydrogel–aggregate mixture was added onto the first layer. Following polymerization at 37°C (90–120 minutes), 1 mL phase III (A, Table 16) medium was carefully added to each well and incubated for 48 hours.

Reagent	Stock concentration	Final concentration	Catalogue Nr.	Company
APEL2 medium	1x		05275	StemCell Technologies

KO Serum replacement	1x	5%	10828028	Gibco
Heparin	100 U/mL	5 U/mL	H3149	Merck
VEGF-A	25 µg/mL	100 ng/mL	130-109-385	Miltenyi
VEGF-C	100 µg/mL	50 ng/mL	11344693	Immunotools
BMP4	25 µg/mL	50 ng/mL	130-111-168	Miltenyi
Murine SCF	10 µg/mL	50 ng/mL	250-03-10UG	Peprotech
FLT3L	25 µg/mL	50 ng/mL	300-19-250	Peprotech
FGF2	100 µg/mL	50 ng/mL	100-18B	Peprotech
rh EPO	100 µg/mL	50 ng/mL	11344793	Immunotools
mTPO	100 µg/mL	50 ng/mL	300-18-10UG	Peprotech
M-CSF	100 µg/mL	50 ng/mL	11343133	Immunotools
IL-3	150 µg/mL	20 ng/mL	11340037	Immunotools
IL-6	25 µg/mL	20 ng/mL	Stefan Rose-John, Kiel, Germany	

Table 16: Composition of the Phase III (A) medium used for the vascular sprouting phase (day 5-7) during the BM organoid differentiation.

By day 7, initial sprouting into the hydrogel was expected. After microscopic evaluation, an additional 1 mL phase III (B, Table 17) medium was added (final volume 2 mL per well), and organoids were cultured for a further 72 hours at 37°C.

Reagent	Stock concentration	Final concentration	Catalogue Nr.	Company
APEL2 medium	1x		05275	StemCell Technologies
KO Serum replacement	1x	5%	10828028	Gibco
Heparin	100 U/mL	5 U/mL	H3149	Merck
VEGF-A	25 µg/mL	50 ng/mL	130-109-385	Miltenyi

VEGF-C	100 µg/mL	25 ng/mL	11344693	Immunotools
BMP4	25 µg/mL	25 ng/mL	130-111-168	Miltenyi
Murine SCF	10 µg/mL	25 ng/mL	250-03-10UG	Peprotech
FLT3L	25 µg/mL	25 ng/mL	300-19-250	Peprotech
FGF2	100 µg/mL	25 ng/mL	100-18B	Peprotech
rhEPO	100 µg/mL	25 ng/mL	11344793	Immunotools
mTPO	100 µg/mL	25 ng/mL	300-18-10UG	Peprotech
M-CSF	100 µg/mL	25 ng/mL	11343133	Immunotools
IL-3	150 µg/mL	10 ng/mL	11340037	Immunotools
IL-6	25 µg/mL	10 ng/mL	Stefan Rose-John, Kiel, Germany	

Table 17: Composition of the Phase III (B) medium used for the vascular sprouting phase (day 7-10) during the BM organoid differentiation.

By day 10, sprouting of the organoids was expected to be visible both microscopically and macroscopically. At this time point, 1 mL of the culture medium was removed and replaced with 1 mL of phase III (C) medium (Table 18). Organoids were then incubated for an additional 72 hours at 37°C.

Reagent	Stock concentration	Final concentration	Catalogue Nr.	Company
APEL2 medium	1x		05275	StemCell Technologies
KO Serum replacement	1x	5%	10828028	Gibco
Heparin	100 U/mL	5 U/mL	H3149	Merck
VEGF-A	25 µg/mL	25 ng/mL	130-109-385	Miltenyi
VEGF-C	100 µg/mL	25 ng/mL	11344693	Immunotools
Murine SCF	10 µg/mL	25 ng/mL	250-03-10UG	Peprotech
FLT3L	25 µg/mL	25 ng/mL	300-19-250	Peprotech
FGF2	100 µg/mL	25 ng/mL	100-18B	Peprotech

rhEPO	100 µg/mL	25 ng/mL	11344793	Immunotools
mTPO	100 µg/mL	25 ng/mL	300-18-10UG	Peprotech
M-CSF	100 µg/mL	25 ng/mL	11343133	Immunotools
IL-3	150 µg/mL	10 ng/mL	11340037	Immunotools
IL-6	25 µg/mL	10 ng/mL	Stefan Rose-John, Kiel, Germany	

Table 18: Composition of the Phase III (C) medium used for the vascular sprouting phase (day 10-13) during the BM organoid differentiation.

On day 13, sprouting organoids were harvested and transferred individually into wells of a 96-well ultra-low attachment (ULA) plate. Larger organoids were carefully retrieved from the hydrogel using a P1000 pipette fitted with wide-bore tips. Remaining organoids were collected by mechanically disrupting the hydrogel and transferring the hydrogel–medium mixture into a 15 mL Falcon tube. Separation of organoids from the hydrogel and conditioned medium was achieved by centrifugation at 200 × g for 4 minutes at room temperature. If necessary, additional centrifugation steps were performed with incremental increases of 100 × g to ensure complete separation. Following isolation, 50 µL of phase IV medium (Table 19) was added to each well of the 96-well plate. Mature organoids were maintained at 37°C with medium changes performed three times per week every second day. During each change, 50% of the medium was carefully removed and replaced with an equal volume of fresh medium.

Reagent	Stock concentration	Final concentration	Catalogue Nr.	Company
StemPro-34 SFM	1x	66%	10639011	Gibco
Conditioned medium		30 %		
KO Serum replacement	1x	2%	10828028	Gibco
Chemically defined lipids	1x	2%	11905031	Gibco
Glutamax	100x	1x	35050061	Gibco

VEGF-A	25 µg/mL	25 ng/mL	130-109-385	Miltenyi
VEGF-C	100 µg/mL	25 ng/mL	11344693	Immunotools
Murine SCF	10 µg/mL	25 ng/mL	250-03-10UG	Peprotech
FLT3L	25 µg/mL	25 ng/mL	300-19-250	Peprotech
FGF2	100 µg/mL	25 ng/mL	100-18B	Peprotech
rh EPO	100 µg/mL	10 ng/mL	11344793	Immunotools
mTPO	100 µg/mL	10 ng/mL	300-18-10UG	Peprotech
IL-3	150 µg/mL	10 ng/mL	11340037	Immunotools
IL-6	25 µg/mL	10 ng/mL	Stefan Rose-John, Kiel, Germany	
M-CSF	50 µg/mL	50 ng/mL	11343133	Immunotools

Table 19: Composition of the Phase IV medium used for mature BM organoid culture (day 13 onward).

This medium was also used for all the downstream experiments with mature BM organoids, including organ-on-a-chip.

4.11.9 Engraftment of exogenous cells into bone marrow organoids

On day 14 of SpinEB protocol (see above), EB-derived cells from JAK2V617F;RFP and JAK2WT;GFP iPSC lines were harvested and $CD34^+$ cells were enriched by magnetic-activated cell sorting using CD34 UltraPure MicroBeads (Miltenyi Biotec, #130-100-453) for subsequent use as donor cells (10,000 of JAK2V617F;RFP and 10,000 JAK2WT;GFP cells per well/organoid) for bone marrow organoids. Primary patient-derived CD34+ HSPCs were isolated from the peripheral blood mononuclear cells using CD34 UltraPure MicroBeads (Miltenyi Biotec, #130-100-453) and stained with CellVue (Sigma Aldrich, #12352207) as per manufacturer's instructions. Table 20 describes the composition of the medium used during the engraftment of exogenous donor cells into BM organoids.

Reagent	Stock concentration	Final concentration	Catalogue Nr.	Company
StemPro-34 SFM	1x	96%	10639011	Gibco
KO Serum	1x	2%	10828028	Gibco

replacement				
Chemically defined lipids	1x	2%	11905031	Gibco
Glutamax	100x	1x	35050061	Gibco
VEGF-A	25 µg/mL	20 ng/mL	130-109-385	Miltenyi
VEGF-C	100 µg/mL	20 ng/mL	11344693	Immunotools
Murine SCF	10 µg/mL	20 ng/mL	250-03-10UG	Peprotech
FLT3L	25 µg/mL	20 ng/mL	300-19-250	Peprotech
FGF2	100 µg/mL	20 ng/mL	100-18B	Peprotech
Penicillin/Steptavidin	100x	1x (100 U/mL)	P06-07100	PAN-Biotech

Table 20: Composition of the medium used for engraftment of exogenous CD34+ cells into BM organoids (day 14-17).

4.11.10 Harvesting of BM organoids

To generate a single-cell suspension of bone marrow organoids (BMOs) for downstream applications such as flow cytometry or qPCR, enzymatic digestion was performed. Briefly, 6–8 organoids per condition were collected in a standard centrifuge tube with minimal residual medium. Subsequently, 1 mL of freshly prepared collagenase IV digestion solution (RPMI 1640 medium (Gibco, #11875085) supplemented with 2.5 mg/mL collagenase IV (Gibco, #17104019)) was added. Samples were incubated in a shaking water bath for 5 minutes, followed by vigorous trituration using a P1000 pipette for 30 seconds and an additional 5-minute incubation. Further mechanical dissociation was performed using a P200 pipette until the organoids visibly decreased in size. This cycle of incubation and pipetting was repeated until complete digestion of the BMOs was achieved.

4.12 Organ-on-a-chip

Microfluidic co-culture experiments were performed using the ibidi Pump System, which comprises a pump unit, a drying bottle filled with silica beads (Carl Roth, #3955.3), fluidic units (#10903), a black perfusion tubing set (#10966), µ-Slide III 3D

Perfusion chips (ibiTreat, #80376), and serial connectors for µ-slides (#10830). Prior to each experiment, perfusion tubing sets, µ-slides, and serial connectors were placed in the incubator overnight to equilibrate to incubation temperature and allow degassing, thereby facilitating bubble-free assembly and experimental setup. Bone marrow organoids containing exogenous CD34+ iHSPCs were loaded into the central gel channel of microfluidic chips and co-cultured with PDL fibroblast spheroids placed in adjacent wells. Chips were connected to a perfusion system and cultured under continuous unidirectional flow using organoid culture medium at 37 °C and 5% CO_2 for 7 days. Fluidic experiments were conducted at a constant pressure of 35 mbar, resulting in a flow rate of 0.48 mL/min, creating a unidirectional flow with a switching time of 60 seconds per reservoir. Reservoirs were filled with 1.3 mL medium (Table 19) after complete filling of the tubing and the chip. The average velocity of medium in the channels, connecting two wells on the chip could be calculated in a simplified manner, neglecting friction effects and not resolving laminar flow, based on the flow rate (Q = 0.008 cm^3/s), the width and the height of the channel (w = 0.1 cm; h = 0.05 cm).

4.12.1 Harvesting of the organ-on-a-chip

After 7 days of co-culture, representative microscopic images of BMOs and PDL spheroids were acquired for each chip using the Zeiss Axio Observer microscope. Subsequently, conditioned medium was collected from the medium reservoirs and transferred into labeled 15 mL Falcon tubes. The perfusion tubing was disconnected from both the fluidic unit and the chip, and any residual medium remaining in the tubing and Luer connectors was carefully recovered and pooled with the collected conditioned medium tube. The pooled medium was centrifuged at 350 × g for 5 minutes to pellet migratory cells for subsequent cytospin preparation. The supernatant (conditioned medium) was aliquoted into three Eppendorf tubes per condition and immediately stored at −20°C for later cytokine array analysis.

PDL spheroids were carefully retrieved from the microfluidic chips. For histological analysis, three spheroids per condition were transferred into Eppendorf tubes and processed as described for BMOs. The remaining spheroids were collected in centrifuge tubes and incubated with 1 mL digestion medium at 37°C for 1 minute to remove residual Matrigel. Samples were then centrifuged at 350 × g for 4 minutes, the

supernatant was discarded, and 300 µL RNA lysis buffer (Thermo Fisher Mini RNA Kit) was added. Lysates were stored at −80°C until subsequent RNA extraction.

BMOs were carefully retrieved from the microfluidic chips using a P1000 pipette fitted with wide-bore tips. For histological analysis, three organoids per condition were fixed in 2% paraformaldehyde (PFA) for 30 minutes, washed with PBS, briefly stained with hematoxylin, and embedded in 3% agarose. After solidification, the agarose-embedded organoids were placed into histology cassettes, dehydrated in 70% ethanol overnight, and subsequently processed for paraffin embedding.

The remaining BMOs were subjected to collagenase IV digestion to generate single-cell suspensions for subsequent flow cytometric analysis with the antibody panel described in Table 21.

Antibody	Fluorochrome	Clone	Catalogue	Company
CD45	BV786	HI30 (RUO)	563716	BD Bioscience
CD14	BV605	63D3	367126	Biolegend
CD235a	PB	HIR2	306612	Biolegend
CD16	BB700	B73.1 (RUO)	742286	BD Bioscience
JAK2-donor	GFP			
CD61	PE-Cy7	VI-PL2(RUO)	336415	Biolegend
JAK2V617F-donor	RFP			
CD34	PE	581	555822	BD Bioscience
CD31	APC-Cy7	WM59	303120	Biolegend
CD66b	APC	G10F5	312115	Biolegend

Table 21: BMO-derived hematopoietic panel after co-culture with PDL spheroids under the microfluidic conditions.

4.13 Histological analysis of FFPE bone marrow organoids

Immunofluorescence staining was performed on 2–5 µm paraffin sections prepared using a microtome (Thermo Scientific, HM355S). All buffers were freshly prepared, including staining buffer (PBS with 0.1% Triton X-100 and 1% FCS), blocking solution (PBS with 0.1% Triton X-100 and 10% FCS), bleaching solution (PBS with 4.5% H_2O_2 and 20 mM NaOH), and citrate buffer (1% citric acid in Milli-Q water). Sections were deparaffinized in xylene (3 × 5 minutes), rehydrated through a descending ethanol series (100%, 90%, 70%), and washed in PBS. Antigen retrieval was performed by heating sections in citrate buffer for 30 minutes, followed by cooling on ice. Slides were then encircled with a hydrophobic barrier pen and briefly washed with the staining

buffer. To reduce autofluorescence, sections were incubated in the bleaching solution under LED light for 45 minutes at room temperature. After washing, blocking was carried out for 1 hour at room temperature. An Avidin/Biotin blocking step (Vector Laboratories, #SP-2001) was subsequently performed according to the manufacturer's instructions. Primary antibodies (Table 22) diluted in the staining buffer were applied and incubated overnight at 4°C in a humidified chamber protected from light. The following day, sections were washed and incubated with appropriate secondary antibodies (1:500) and DAPI (1:1000) (Table 23) for 1 hour at room temperature in the dark. After final washing steps, slides were mounted using pre-warmed ProLong Gold Antifade Mountant (Invitrogen, #P36930) and stored at 4°C until imaging.

4.14 Immunofluorescence staining on microfluidic chip

Immunofluorescence staining on microfluidic chips was performed in the wells containing PDL spheroids on the Ibidi chips. Chips were placed in humid chambers and washed three times for 3 minutes with PBS-TS (PBS containing 0.1% Triton X-100 and 1% FCS). Approximately 30 µL PBS-TS containing primary antibodies (Table 22) was added to each well, followed by overnight incubation at 4°C in a humidified chamber protected from light. The following day, the antibody solution was carefully removed and wells were washed three times with PBS-TS. Subsequently, 30 µL PBS-TS supplemented with secondary antibodies (1:500), DAPI (1:1000) (Table 23), and directly labeled antibodies was added. Chips were incubated for 1 hour at room temperature in the dark. After staining, wells were washed three times with 50 µL PBS-TS, each with a 5-minute incubation. Finally, 50 µL PBS-TS was added to each well, and the chips were imaged immediately.

Antibody	Host	Conjugation	Dilution	Reference
Anti-GFP	Rat igG	AF488	1:100	BD Bioscience (#563716)
Anti-RFP	Goat	Unconjugated	1:400	Rockland (#200-101-379)
Phalloidin	-	AF647	1:500	Life technologies (#A22287)

Table 22: Primary antibodies used for immunofluorescence imaging of FFPE tissue and microfluidic chip.

Antibody	Host	Conjugation	Dilution	Reference
DAPI	------	------	1:1000	BioLegend (#422801)
Goat anti-rat	Goat	AF647	1:500	ThermoFisher Scientific (#A21247)

Table 23: Secondary antibodies used for immunofluorescence imaging of FFPE tissue and microfluidic chip.

4.15 Co-detection by indexing (CODEX) multiplex imaging

Multiplex immunofluorescence imaging was performed using the PhenoCycler (Akoya) at 40× magnification according to the manufacturer's instructions. FFPE BMO sections (3 µm) were mounted on poly-L-lysine-coated slides, incubated overnight at 60°C, deparaffinized in xylene, and rehydrated through a descending ethanol series followed by ddH_2O. Antigen retrieval was carried out in a citrate buffer for 20 minutes, followed by bleaching under LED light for 45 minutes as described above. Slides were blocked using a CODEX-specific blocking buffer containing S2 staining buffer supplemented with mouse and rat IgG, sheared salmon sperm DNA, and non-fluorescent oligonucleotides. Sections were incubated overnight at 4°C with a custom DNA-conjugated antibody cocktail according to the predefined multicycle panel (Table 24-25). After staining, tissues were fixed with 1.6% paraformaldehyde, treated with cold methanol, and crosslinked using BS3. Slides were washed and stored in CODEX staining buffer at 4°C until imaging. For each imaging cycle, slides were incubated with a buffered solution containing DAPI and fluorescently labeled oligonucleotides complementary to the antibody-conjugated barcodes. Cycle solutions were prepared in advance in a 96-well plate, with each well containing fluorescent oligonucleotides (400 nM final concentration) diluted in PhenoCycler-Fusion buffer supplemented with DAPI and salmon sperm DNA. Blank wells containing buffers only were included for the first and last cycles. Plates were sealed until use.

Cycle	Cy3	Cy5	AF750
1	Blank	Blank	Blank
2	CD138 _mal12	Ki-67 _mal13	**aSMA _mal11**

3	SPP1 _mal34	Nestin _mal16	RFP _mal57
4	CD36 _mal23	Collagen IV _mal20	CD16 _mal8
5	CD56 _mal46	CD68 _mal26	S100B _mal45
6	CD11c _mal30	CD14 _mal27	PF4 _mal36
7	Vimentin _mal33	IDO1 _mal38	CD61 _mal10
8	CD45 _mal42	CD146 _mal7	CD11b _mal9
9	TGFB1 _mal43	CXCL13 _mal17	CD34 _mal56
10	GFP _mal3	MCT _mal40	Empty
11	Glycophorin A _mal32	Interferon g _mal48	Empty
12	CD38 _mal37	Collagen 1 _mal28	Empty
13	S100A4 _mal4	S100A8+9 _mal53	Empty
14	Empty	Podoplanin _mal6	Empty
15	Empty	CXCL12 _mal47	Empty
16	Empty	**CD31 _mal1**	Empty
17	Blank	Blank	Blank

Table 24: Overview of the multicycle sequence of the CODEX imaging.

The fluorescence images and the quantification of only aSMA+ and CD31+ cells were shown in this study.

Antibody	Host	Reference
aSMA	Mouse	Abcam (#ab240654)
CD31	Mouse	Cell Signaling Technology (#85873SF)

Table 25: Information on CODEX antibodies shown in this study.

4.16 Cytokine array

Cytokine profiling was performed using 1 mL of undiluted, freshly frozen culture supernatant derived from PDL spheroids or microfluidic co-culture experiments. The Abcam Human Cytokine Antibody Array (#ab133998, Abcam) was used according to

the manufacturer's instructions, including all recommended overnight incubation steps. For detection, array membranes were placed on a Blot/UV/Stain-Free Sample Tray (Bio-Rad, #12003028) and imaged with the ChemiDoc Imaging System using chemiluminescence mode (detection size: S; exposure time: 1 s). Image analysis was performed in ImageJ using the "Protein Array Analyzer" macro (Carpentier and Hernault, 2010), which quantifies relative cytokine signal intensities. Data normalization was conducted according to the manufacturer's guidelines. Cytokine array was performed by Lucas Greven as part of his master thesis work under my supervision.

4.17 Cytospins

Morphological analysis of migrating hematopoietic cells from the conditioned medium of the microfluidic chip was performed using Diff Quick staining (Medion Diagnostic, Switzerland). Once the conditioned medium was centrifuged and the pellet of cells collected, isolated cells were centrifuged again at 1400 rpm for 4 min and washed once with PBS. A cytospin chamber, filter card, and glass slide (all Thermo Fischer Scientific) were assembled and prepared by adding 300 µl 1x PBS per hole and spinning at 270 rpm for 4 min. Cytospin chambers were centrifuged in a Shandon Cytospin^{TM} 4 cytocentrifuge (Thermo Fischer Scientific). Finally, 200-400 cell suspension was applied per hole of prepared cytospin chambers, and cells were centrifuged onto glass slides at 270 rpm for 4 min. Glass slides were air-dried before being fixed with methanol (Merck) for 4 min. Subsequently, to visualize myeloid population cells were subjected to Diff Quick solution I five times for 5 sec and Diff Quick solution II (both Merck Millipore, Burlington, Massachusetts, USA) for 30 sec. Lastly, cells were washed with distilled water until excess staining solutions were rinsed off. Glass slides were air-dried and mounted with Entellan (Merck).

4.18 *in vitro* pharmacological perturbations

For drug treatment, mature BM organoids engrafted with JAK2V617F;RFP and JAK2WT;GFP at a ratio of 1:1 were treated with vehicle (water) or LSKL (5µM, #HY-P0299, MCE) either statically or added on top of the fluidic unit starting from 7 days post engraftment of exogenous cells for three times with media replenishment every second day.

4.19 Transcriptomic analysis

4.19.1 RNA extraction

Prior to RNA isolation, PDL cell suspensions, PDL spheroids, or single-cell suspensions derived from BMOs were stored at −80°C in lysis buffer supplemented with β-mercaptoethanol (1:100) from the PureLink™ RNA Mini Kit (Invitrogen, #12183025). For extraction, samples were thawed and homogenized, and RNA was isolated according to the manufacturer's protocol. RNA concentration and purity were determined using the DeNovix DS-11 FX+ spectrophotometer. After extraction, RNA samples were kept on ice during handling and stored at −80°C until further use.

4.19.2 cDNA synthesis

cDNA synthesis was performed immediately after RNA quantification using the iScript™ cDNA Synthesis Kit (Bio-Rad, #1708890). Up to 15 µL of eluted RNA was used per reaction, aiming for an input of 1000 ng total RNA. If RNA concentration was insufficient, the maximum available amount was used, and equal RNA input was maintained across all samples within the same experiment. Reverse transcription was carried out according to the manufacturer's protocol (5 minutes at 25°C for priming, 20 minutes at 46°C for reverse transcription, and 1 minute at 95°C for enzyme inactivation). Synthesized cDNA was stored at −20°C for subsequent analyses.

4.19.3 qRT-PCR

Throughout the entire qPCR preparation, samples and primers were kept on ice, and filter tips were used to prevent contamination. A primer master mix was prepared with 10µM of both forward and reverse primers as well as 6µL Fst SYBR green master mix (#4385617, Applied Biosystems) and aliquoted into the appropriate wells of a hard-shell 96-well PCR plate (Bio-Rad, #HSP9601). Subsequently, a cDNA dilution consisting of 1 µL cDNA and 4.5 µL Invitrogen™ Nuclease-Free Water (Invitrogen, #10185104) was added to each designated well. The plate was sealed with adhesive film and briefly centrifuged before being placed into the CFX Opus 96 Real-Time PCR System (Bio-Rad). The qPCR cycling conditions are summarized in Table 26. All reactions were performed in technical duplicates for each gene–sample combination. *GAPDH* was used as the housekeeping gene for normalization. Relative gene

expression changes between treated and control groups were calculated based on the Ct values obtained from the qPCR analysis.

Step	Temperature [°C]	Time [min]
1	95	20
2	95	3
3+ plate read	60	0.5
4	Go to 2	(39x)
5	95	5
6 melt curves + plate read	60 - 94.8; 0.3°C increments	-

Table 26: Cycling conditions for qRT-PCR.

Primers for qPCR analysis were obtained from Eurofins Genomics and are listed in Table 27. Primer sequences were designed using the Primer-BLAST tool provided by the National Center for Biotechnology Information (NCBI).

Design criteria included: (i) an amplicon length of less than 200 bp, (ii) minimal self-complementarity to avoid primer-dimer formation, (iii) a melting temperature (Tm) between 58°C and 60°C with a maximum difference of 1°C between forward and reverse primers, and (iv) primer binding sites spanning exon–exon junctions to prevent amplification of genomic DNA. Primers were designed by Lucas Greven as part of his master thesis work under my supervision.

Gene name	Forward sequence	Reverse sequence
GAPDH	GAAGGTGAAGGTCGGAGTC	GAAGATGGTGATGGGATTTC
ACTA2	TCCTTCATCGGGATGGAGTCT	TACATAGTGGTGCCCCCTGA
COL1A1	ACGGCTGCACGAGTCACAC	GGCAGGCGGGAGGTCTT
THBS1	GACGCCTGCCCCATCAAT	TCTGTACCCCTCCTCCACAG
Cytl1	TCGGAGCCCTCGTTGGA	TCCTCCACAATGCTACGGC
IL-1beta	CACTTACATTGTCACCAGAGAACC	ATCGTGCACATAAGCCTCGT
ACAN	TGGGAACCAGCCTATACCCCAG	TGGGAACCAGCCTATACCCCAG
SOX9	TCTCGCTTCAGGTCAGCCTTG	GCATGAGCGAGGTGCACTC
CD47	CCTGAAATCAGAAGAGGGCCA	AGTCTCTGTATTGCGGCGTG
IL1-alpha	TCTCTAAAGCTACAGCCTCTCCT	TTTGGCCATCTTGACTTCAAACC
IL-6	CCACCGGGAACGAAA	TCT CCT GGG GGT ATT
ICAM1	AGCTTCGTGTCCTGTATGGC	TTTTCTGGCCACGTCCAGTT

Table 27: Primer sequences used for qRT-PCR.

4.20 Statistical analysis

Statistical analysis, excluding that for scRNaseq data, was conducted using either GraphPad Prism Version 10. Unless otherwise stated in the figure legends, two-tailed

unpaired Student's *t* test was used for statistical analysis. Data are shown as data ± SEM, and a P-value of less than 0.05 was considered statistically significant. *P < 0.05; **P < 0.01; ***P < 0.001; ****P < 0.0001.

5 Results

5.1 Site-specific periodontal bone remodeling across ontogenetically distinct skeletal compartments in MPN

To investigate whether bones of different developmental origins exhibit distinct remodeling responses in myeloproliferative neoplasms, we performed a systematic whole-body imaging analysis using ^{18}F-fluorodeoxyglucose (FDG) positron emission tomography combined with computed tomography (PET/CT) from patients with myelofibrosis (primary MF, n = 5; post-ET MF, n = 2) (Figure 6A,B, Supplementary Table 1).

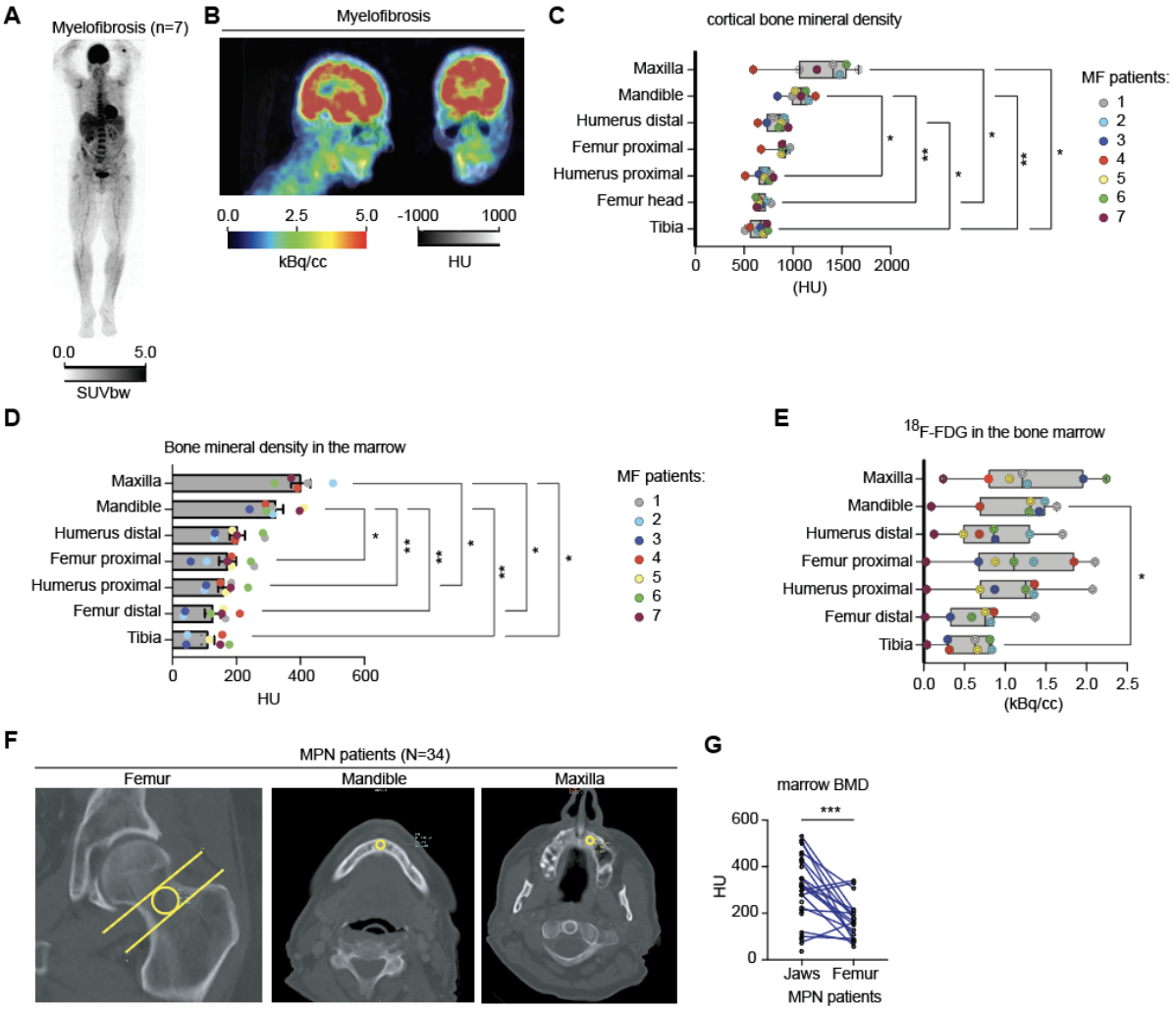

Figure 6: Ontogeny-dependent skeletal alterations in myelofibrosis across neural crest- and mesoderm-derived bones.

(A–B) Representative ^{18}F-FDG PET/CT scans from patients diagnosed with myelofibrosis (total n = 7; primary MF n = 5, post-ET MF n = 2).

(C) Quantitative intra-individual analysis of cortical bone mineral density in neural crest–derived and mesoderm-derived skeletal sites in MF patients (color-coded). Bone density values are reported in Hounsfield units (HU). Statistical comparisons were performed using one-way ANOVA followed by Tukey's post hoc test.
(D) Intra-patient comparison of marrow-associated bone mineral density between neural crest–derived and mesoderm-derived bones in MF patients (color-coded), expressed in Hounsfield units (HU). Statistical significance was assessed by one-way ANOVA with Tukey's post hoc correction.
(E) Whole-body evaluation of metabolic activity across different skeletal regions in MF patients (n = 7, color-coded). Statistical analysis was conducted using one-way ANOVA followed by Tukey's multiple comparison test.
(F) Representative computed tomography (CT) images from retrospective radiological analyses showing quantification of marrow bone mineral density in jawbones compared with the femur in the same cohort of MPN patients (n = 34). Statistical evaluation was performed using a paired two-tailed Student's t-test. Data acquisition was carried out by Dr. Aleksandar Kargaliev, Department of Diagnostic and Interventional Radiology, RWTH Aachen Hospital.
A), B), D), F), G) was previously included in Atakhanov S., Ghezzi I., Tejeda H. *et al.* BioRxiv 2026[54] .

Quantitative assessment of cortical and marrow-associated bone mineral density (BMD) of distinct skeletal sites of the same MF patients revealed a marked increase in both periodontal bones (Figure 6C,D). Across this cohort, neural crest–derived jaw bones consistently exhibited the highest BMD values, whereas mesoderm-derived long bones, particularly the tibia, showed substantially lower BMD. These findings uncover preferential periodontal bone remodeling in MF and emphasize the necessity of evaluating ontogeny-dependent bones in MPNs.

We next examined marrow metabolic activity using FDG uptake as a surrogate measure (Figure 6E). Jawbones showed more FDG signal than distal part of the femur and tibia, suggesting that aberrant bone remodeling is coupled with preferential infiltration of metabolically active hematopoietic cells in the periodontal tissues.

In line with this, performing CT analysis of an independent MPN cohort (n=34) showed significant increase in marrow-associated BMD in the jawbones than femur (Figure 6F, Supplementary Table 2), supporting the hypothesis that periodontal tissue shows distinct severity in bone remodeling than long bones.

5.2 Population-level evidence for bone degeneration in MPN

Although clinical imaging modalities allow robust quantification of regional osteosclerosis and metabolic changes, they are limited in their ability to resolve trabecular microarchitecture and dynamic bone resorption processes.

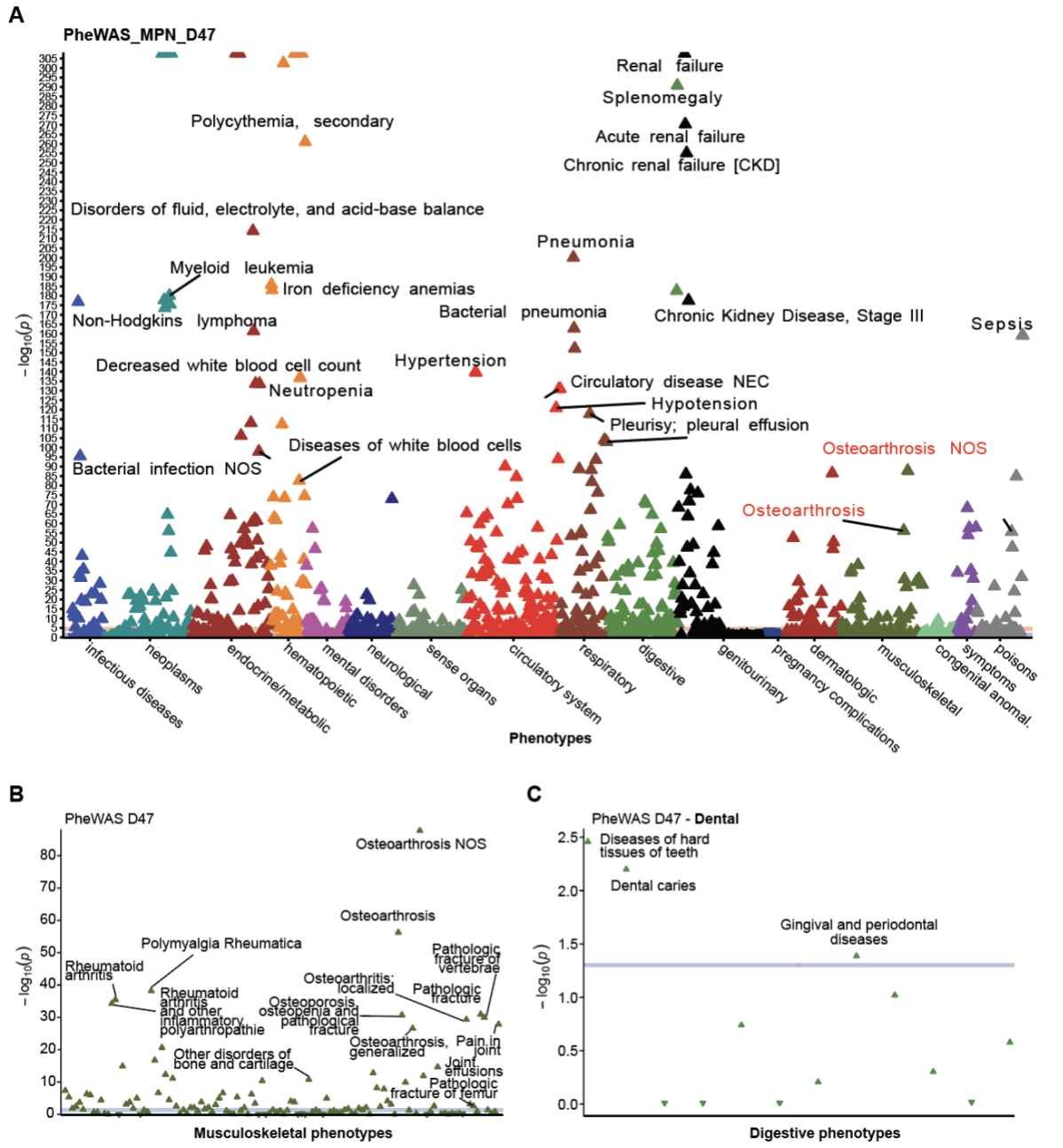

Figure 7: Population-based study reveals significant association of bone destructive and dental phenotypes in MPN patients.

(A-C) Phenome-wide association study from UK Biobank (UKBB) with all phenotypes (A), musculoskeletal (B) and digestive (C) phenotypes highly associated with MPN individuals (n=2,548; ICD-10 D47). Data was provided by Prof. Carolin V. Schneider, Department of

Gastroenterology, Metabolic Diseases and Intensive Care (RWTH Aachen Hospital). A-C) was previously included in Atakhanov S., Ghezzi I., Tejeda H. *et al.* BioRxiv 2026[54] .

To overcome the limitations of imaging-based analyses and to assess skeletal degeneration at the population level, we leveraged data from the UK Biobank, comprising approximately 500,000 participants. Within this dataset, 2,548 individuals diagnosed with MPN (ICD-10 code D47) were identified and subjected to a phenome-wide association study (PheWAS). Among all significantly enriched disease categories, osteoarthrosis ranked as one of the most strongly associated musculoskeletal phenotypes in individuals with MPN (Figure 7A). When restricting the analysis specifically to musculoskeletal traits, significant associations emerged with a broad range of bone-destructive conditions, including rheumatoid arthritis, osteoarthritis, vertebral and femoral pathological fractures, osteoporosis, osteopenia, joint pain, and disorders affecting bone and cartilage (Figure 7B).

Given the pronounced remodeling observed in periodontal bone by imaging, we further examined dental and oral phenotypes within the UK Biobank cohort. Disorders affecting tooth hard tissues, dental caries, as well as gingival and periodontal diseases were all significantly overrepresented in individuals with MPN (Figure 7C).

Collectively, these data demonstrate that MPN-associated skeletal pathology is not uniform but instead engages both osteosclerotic and bone-destructive programs. Notably, periodontal bone emerges as a previously underrecognized skeletal compartment with disproportionate disease involvement, highlighting the need to consider craniofacial niches when studying bone remodeling and inflammatory pathology in MPNs.

5.3 Single-cell mapping of hematopoietic and stromal cells from the developmentally distinct bones in myelofibrosis

Our imaging and population-level analyses uncovered striking ontogeny-dependent differences in bone remodeling and metabolism in MF, identifying periodontal bone as a uniquely affected skeletal niche. To define the cellular basis of these site-specific phenotypes, we performed scRNAseq of matched iliac crest bone marrow biopsies and extracted teeth.

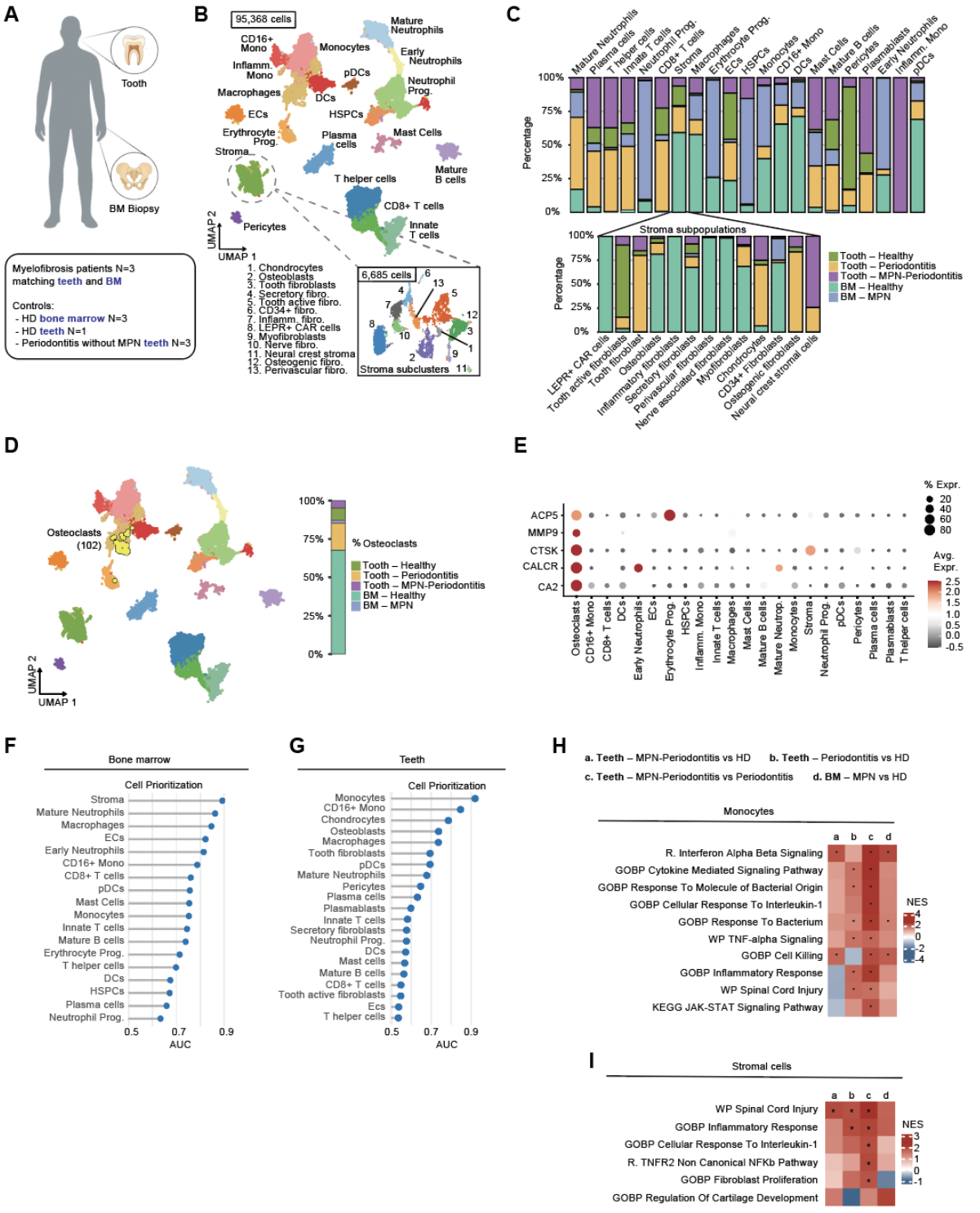

Figure 8: Single-cell mapping of bone marrow and periodontal niches reveals cell type-specific perturbations in myelofibrosis.

(A) Overview of the study design illustrating patient cohorts, anatomical sampling sites, and experimental workflow for intra-individual single-cell RNA sequencing of matched bone marrow (BM) and dental specimens from myelofibrosis (MF) patients (n=3). The study design also includes healthy donor controls (n=1) and periodontitis-only controls (n=3) where applicable. Schematic created with ChatGPT.

(B) Uniform Manifold Approximation and Projection (UMAP) visualization of the integrated single-cell transcriptomic dataset containing 95,368 cells obtained from paired BM and tooth samples. The inset highlights higher-resolution clustering of 6,685 stromal cells, which were further subdivided into 13 transcriptionally defined subpopulations.
(C) Relative representation of annotated cell populations across tissues and experimental conditions.
(D) UMAP visualization of the integrated dataset highlighting identification of an osteoclast subpopulation (n = 102 cells) within the macrophage compartment, together with its distribution across tissues and conditions.
(E) Dot plot depicting the five most enriched osteoclast-associated marker genes, demonstrating selective expression within the osteoclast cluster.
(F–G) Cell prioritization analysis of all annotated cell types in BM (F) and dental tissues (G), identifying cell populations most transcriptionally affected by MF pathology relative to healthy controls.
(H–I) Functional pathway enrichment analysis of differentially expressed genes in monocytes (H) and stromal cells (I) across multiple comparisons:
(a) MPN-associated periodontitis versus healthy dental tissue,
(b) Periodontitis without MPN versus healthy dental tissue,
(c) MPN-associated periodontitis versus periodontitis without MPN, and
(d) MPN bone marrow versus healthy bone marrow.
Pathway enrichment was conducted using Reactome, Gene Ontology (GO), WikiPathways, KEGG, BioCarta, and PID databases. Computational analyses were performed by Dr. Hector Tejeda Mora, Department of Developmental Biology, Erasmus Medical Center. A-I) was previously included in Atakhanov S., Ghezzi I., Tejeda H. *et al.* BioRxiv 2026[54] .

We identified JAK2V617F-mutant MF patients (n=3) undergoing pre-transplant evaluation, who routinely receive dental screening to exclude infection risk prior to alloHSCT. The extracted teeth due to periodontitis in combination with matching BM biopsies used for fibrosis grading, provided a unique opportunity to dissect hematopoietic–stromal crosstalk in ontogenetically distinct skeletal compartments. To establish appropriate baselines, MF BM was compared to biopsies from age-matched individuals (n=3) undergoing hip replacement. For periodontal tissues, we analyzed one patient with caries but intact periodontium (n=1) as a healthy reference and periodontitis patients without hematologic malignancies (n=3) to delineate the specific contribution of the MPN clone to periodontal remodeling (Figure 8A, Supplementary Table 3).

We profiled 95,368 cells from sort-enriched bone marrow and dental samples across all conditions (Figure 8B,C). Clustering and dimensionality reduction analysis enabled us to manually annotate 20 clusters corresponding to progenitor population (hematopoietic stem and progenitor cells), myeloid cells (neutrophil progenitors, early

and mature neutrophils, dendritic cells, plasmacytoid dendritic cells, mast cells, monocytes, CD16+ monocytes, macrophages, erythrocyte progenitors), lymphoid cells (mature B cells, plasma cells, T helper cells, CD8+ T cells, innate T cells) and non-hematopoietic stromal cells, also referred to as niche cells (endothelial cells, stromal cells and pericytes). To delineate the stromal heterogeneity, we subclustered 6,685 stromal cells into chondrocytes, osteoblasts, tooth fibroblasts, secretory fibroblasts, tooth active fibroblasts, CD34+ fibroblasts, inflammatory fibroblasts, LepR+ CXCL12 abundant reticular (CAR) cells, myofibroblasts, nerve-associated fibroblasts, neural crest stromal cells, osteogenic fibroblasts and perivascular fibroblasts. Given the importance of osteoclasts in bone resorptive phenotype, annotation with higher granularity enabled us to capture osteoclast subpopulation within the macrophage cluster (Figure 8D,E).

We leveraged Augur[55], a high-dimensional machine-learning framework that quantifies cell-type–specific separability between conditions using the area under the receiver operating characteristic curve (AUC) as a perturbation score. This approach enabled us to identify bone marrow and dental cell populations that were most transcriptionally responsive to MPN-driven injury compared with healthy controls. Because stromal cell recovery was limited in MPN bone marrow (Figure 8C), we applied Augur to the combined BM stromal compartment. In contrast, periodontal samples showed sufficient stromal diversity to enable subcluster-level analysis, allowing identification of the stromal lineages most perturbed in MPN. Across both bone marrow and teeth, myeloid and stromal populations consistently ranked among the top three most transcriptionally perturbed cell types in MPN (Figure 8F,G). In MPN teeth, monocytes, $CD16^{+}$ monocytes, and macrophages were the most perturbed hematopoietic populations, whereas chondrocytes, osteoblasts, and tooth fibroblasts exhibited the strongest transcriptional alterations among stromal lineages.

To further interrogate the myeloid and stromal compartments, we performed pathway enrichment analysis in monocytes and stromal cells across all four conditions. When comparing periodontitis with MPN to periodontitis without MPN (condition C), the top 10 most significantly enriched pathways in monocytes revealed a markedly inflammatory and activated transcriptional state, characterized by interferon-α/β signaling, response to interleukin-1, TNF-α and JAK–STAT signaling, alongside

broader activation programs including cytokine-mediated signaling, response to bacterium, cell killing, and spinal cord injury–associated pathways (Figure 8H). In the corresponding stromal compartment, the same comparison showed significant upregulation of spinal cord injury, inflammatory and fibroblast proliferation pathways, indicating a robust fibro-inflammatory activation state in MPN jaws (Figure 8I). Notably, regulation of cartilage development was selectively elevated in MPN conditions in both teeth and bone marrow, pointing to a shared, disease-specific osteochondral injury across ontogenetically distinct skeletal niches.

5.4 Dissecting the transcriptional profile of monocytes and cellular interactions in the periodontal niche

In line with the pathway enrichment analysis, differentially expressed gene (DEG) analysis revealed inflammatory genes upregulated in monocytes in different inflammatory conditions (Figure 9A-D). Monocytes in MPN-Periodontitis condition in comparison to periodontitis teeth significantly upregulated pro-inflammatory genes (*ANKRD22, GBP5, OSM, CD274, PIM1*), suggesting that the MPN monocytes amplify local periodontal inflammation by driving an elevated pro-inflammatory phenotype of monocytes beyond that observed in periodontitis alone (Figure 9C). Meanwhile, MPN monocytes in the bone marrow in comparison to healthy control showed fibrosis-associated markers (*CD38, SLAMF7, PTH2R*), suggesting their fibrogenic potential in the bone marrow of MPN individuals (Figure 9D).

CellChat-based cellular crosstalk in the MPN-Periodontitis teeth in comparison to periodontitis samples without MPN revealed that these niche cells (endothelial cells and stromal subclusters) engage in selective and robust interactions with osteoclasts specifically under MPN conditions (Figure 9E). Moreover, osteoclasts from MPN-Periodontitis patients exhibited heightened signaling activity both as senders and receivers compared with osteoclasts from periodontitis patients without MPN, indicating an MPN-specific amplification of stromal–osteoclast communication.

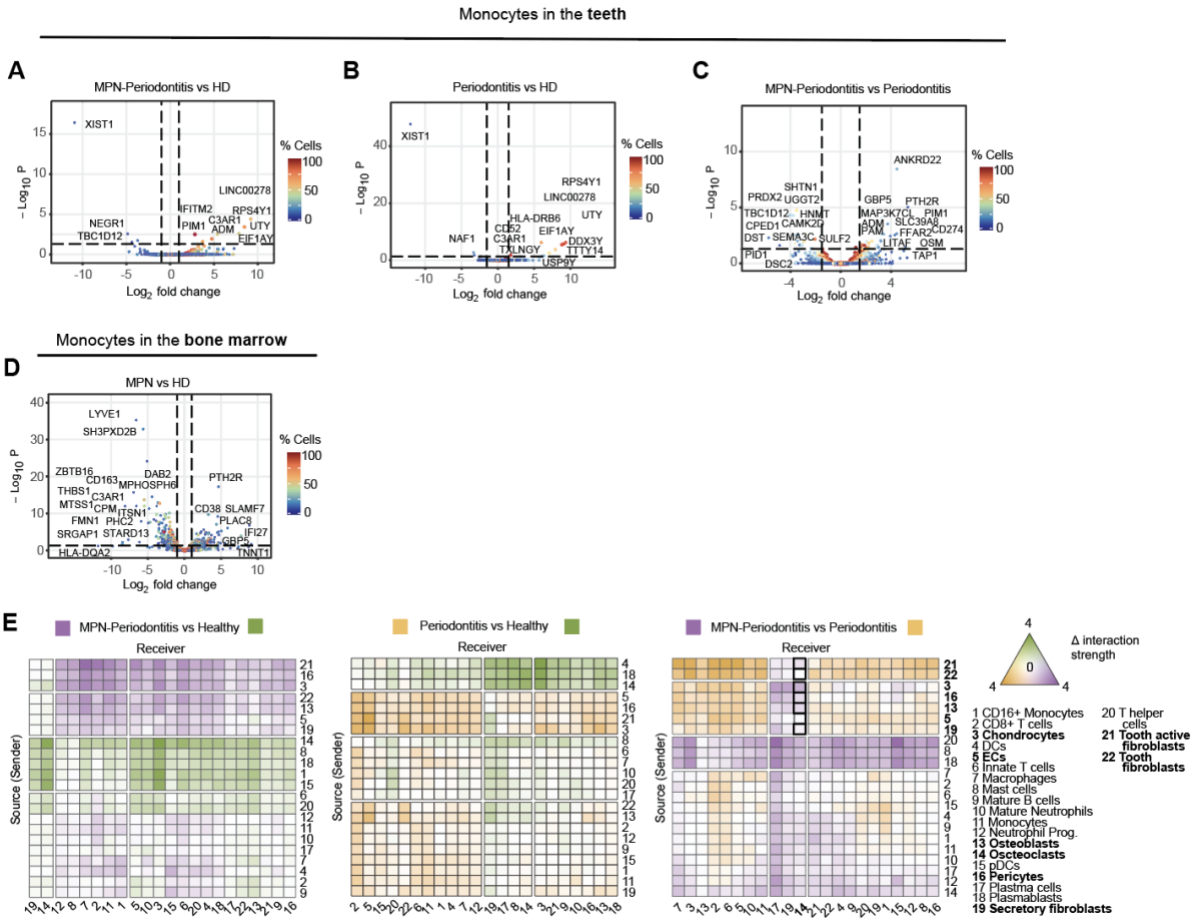

Figure 9: Enhanced inflammatory gene expression and cellular communication in MPN-associated periodontal pathology.

(A–D) Volcano plots illustrating differentially expressed genes (DEGs) in monocytes across multiple comparisons: MPN-associated periodontitis versus healthy donor (HD) in dental tissue (A), periodontitis without MPN versus healthy donor in dental tissue (B), MPN-associated periodontitis versus periodontitis without MPN in dental tissue (C), and MPN versus healthy donor in bone marrow samples (D).
(E) Analysis of cell–cell communication networks in patient-derived dental biopsies, comparing the indicated experimental conditions (color-coded). Bioinformatic analyses were conducted by Dr. Hector Tejeda Mora, Department of Developmental Biology, Erasmus Medical Center. A-E) was previously included in Atakhanov S., Ghezzi I., Tejeda H. *et al.* BioRxiv 2026[54] .

5.5 Single-cell analysis of paired teeth and bone marrow biopsies uncovers divergent cellular programs across ontogenetically distinct skeletal niches in myelofibrosis

We next asked whether MPN monocytes adopt distinct transcriptional states across different skeletal environments. To address this, we performed DEG analysis on monocytes isolated from pelvic bone and teeth of the same MF patients, providing, for the first time, a direct view of how a clonal hematopoietic population is transcriptionally

tuned across ontogenetically distinct skeletal niches within individual MF patients (Figure 10A). Overall, monocytes from BM and teeth displayed remarkably similar transcriptional profiles (Figure 10B), consistent with the idea that circulating MPN monocytes maintain a conserved transcriptional identity as they transit between tissues. However, a discrete set of site-specific genes emerged. In the BM, monocytes upregulated the complement pathway (*C1QC*), underlining the integral role of the complement system in MF. In contrast, monocytes in the periodontal niche induced genes associated with inflammation, tissue infiltration and periodontitis progression (*CCL2, TNFRSF10C, MIR3945HG*), together with markers indicative of monocyte-to-macrophages differentiation (*ADGRE2*, also EMR2 or CD312). These findings suggest that while MPN monocytes retain a shared transcriptional profile in both tissues, they upregulate certain gene signatures in response to external inflammation (periodontitis) that enable their infiltration into the periodontal niche and promote its inflammatory and osteolytic remodeling.

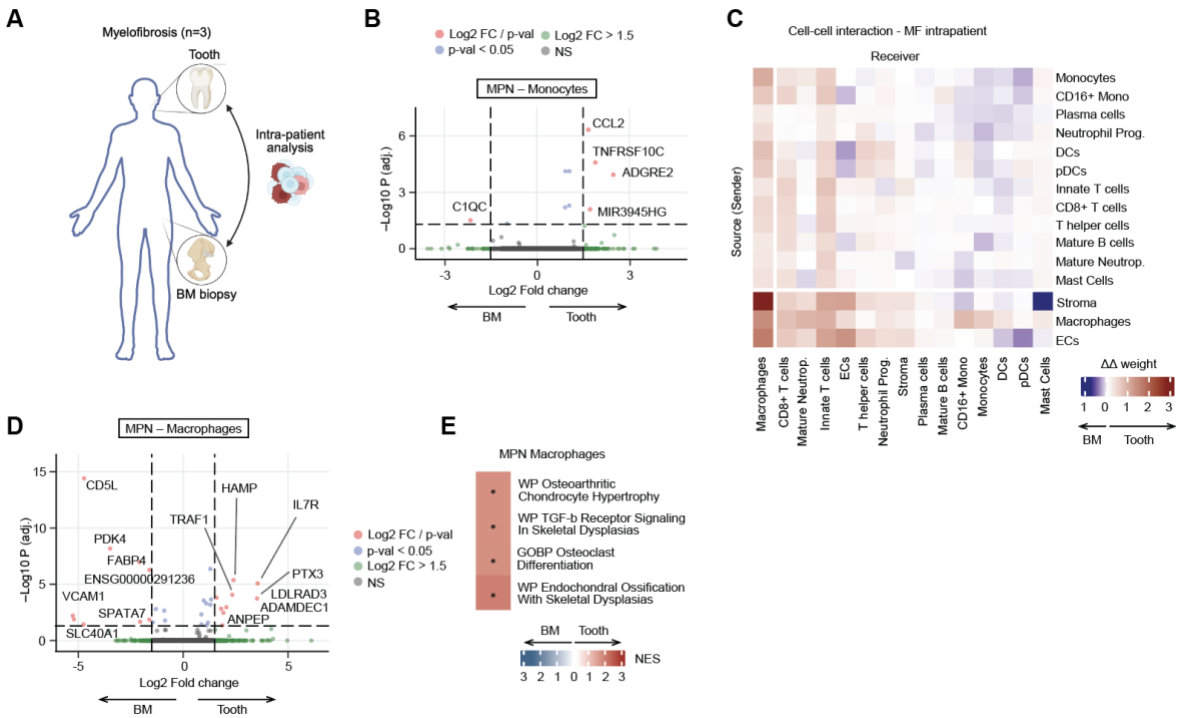

Figure 10: Intra-patient comparison reveals niche-specific transcriptional and communication programs in mesoderm and neural crest tissues in myelofibrosis.

(A) Diagram illustrating the intra-individual study design used to analyze cellular programs in matched dental and bone marrow biopsy samples obtained from the same myelofibrosis (MF) patients (n = 3). Created in BioRender. Goetz, K. (2026) https://BioRender.com/xopcbt9
(B) Volcano plot showing differentially expressed genes in monocytes identified from intra-patient comparisons between dental tissue and bone marrow samples from the same MF individuals.

(C) Cell–cell communication networks inferred from paired samples, highlighting interactions in dental tissue (red) and bone marrow (blue) derived from the same MF patients.
(D) Volcano plot depicting differential gene expression in macrophages from intra-patient comparisons between dental and bone marrow compartments in MF individuals.
(E) Pathway enrichment analysis of macrophage transcriptional programs comparing dental tissue (red) and bone marrow (blue) within the same MF patients. Bioinformatic analyses were performed by Dr. Hector Tejeda Mora, Department of Developmental Biology, Erasmus Medical Center. B-E) was previously included in Atakhanov S., Ghezzi I., Tejeda H. *et al.* BioRxiv 2026[54] .

We next applied CellChat to dissect cell–cell communication networks in the BM and periodontal tissues of the same individuals. Macrophages exhibited substantially greater outgoing and incoming signaling activity in the periodontium compared with the bone marrow, with the strongest interactions occurring between macrophages and periodontal stromal cells (Figure 10C). Differential expression analysis of tooth-resident macrophages revealed elevated expression of genes associated with tissue infiltration, migration, and inflammation (including *HAMP, PTX3, IL7R, LDLRAD3* and *TRAF1*; Figure 10D). Consistent with this activated state, pathway analysis showed significant upregulation of bone-destructive programs in the periodontal niche, including osteoarthritic chondrocyte hypertrophy, osteoclast differentiation, and endochondral ossification associated with skeletal dysplasias (Figure 10E). As we also identified an osteoclast subcluster within the macrophage compartment (Figure 8D,E), this further supports the transcriptional shift of macrophages toward osteoclastogenic differentiation. These results reveal that the periodontal niche elicits a uniquely potent activation state in MPN macrophages, driving inflammatory and bone-destructive programs. This niche-specific cellular interaction positions the macrophage–stromal crosstalk as a potential driver of the periodontal remodeling in the MPN-affected jaws.

5.6 Murine JAK2 knock-in model demonstrates post-PV MF phenotype

To directly test whether JAK2V617F mutant clones in MPN alone, in the absence of any other underlying disease, are sufficient to drive both osteosclerosis and osteoporosis, we isolated whole bone marrow (BM) cells from Cre-inducible JAK2V617F or JAK2WT donors, mixed 1:1 with wild-type (WT) competitor cells and competitively transplanted into lethally irradiated WT recipient mice (Figure 11A). As early as 4 weeks post-transplantation, recipients of JAK2V617F BM developed a

robust PV phenotype, characterized by elevated erythrocyte, leukocyte and platelet counts, together with increased hemoglobin and hematocrit levels (Figure 11B,C). By 20 weeks post-transplantation, JAK2V617F mice progressed to overt myelofibrosis, manifested by marked splenomegaly, reduced BM cellularity and viability, and declining hemoglobin and hematocrit levels (Figure 11B-E). Concomitantly, hematopoietic differentiation was profoundly skewed, with depletion of long- and short-term hematopoietic stem cells (HSCs) and expansion of $Lin^{-}Sca1^{+}c\text{-}Kit^{+}$ (LSK) cells dominated by multipotent progenitors (MPPs) (Figure 11F). Within the committed progenitor compartment, granulocyte–macrophage progenitors (GMPs) were markedly expanded at the expense of megakaryocyte–erythroid progenitors (MEP) (Figure 11G). Given that GMPs represent a major source of osteoclast precursors, this expansion might be a predisposition for an increased osteoclastogenic potential within the fibrotic BM. Histological analysis (reticulin staining) of tibias further confirmed post PV-MF development (Figure 11H). Together with splenomegaly, these changes are indicative of a shift towards extramedullary hematopoiesis.

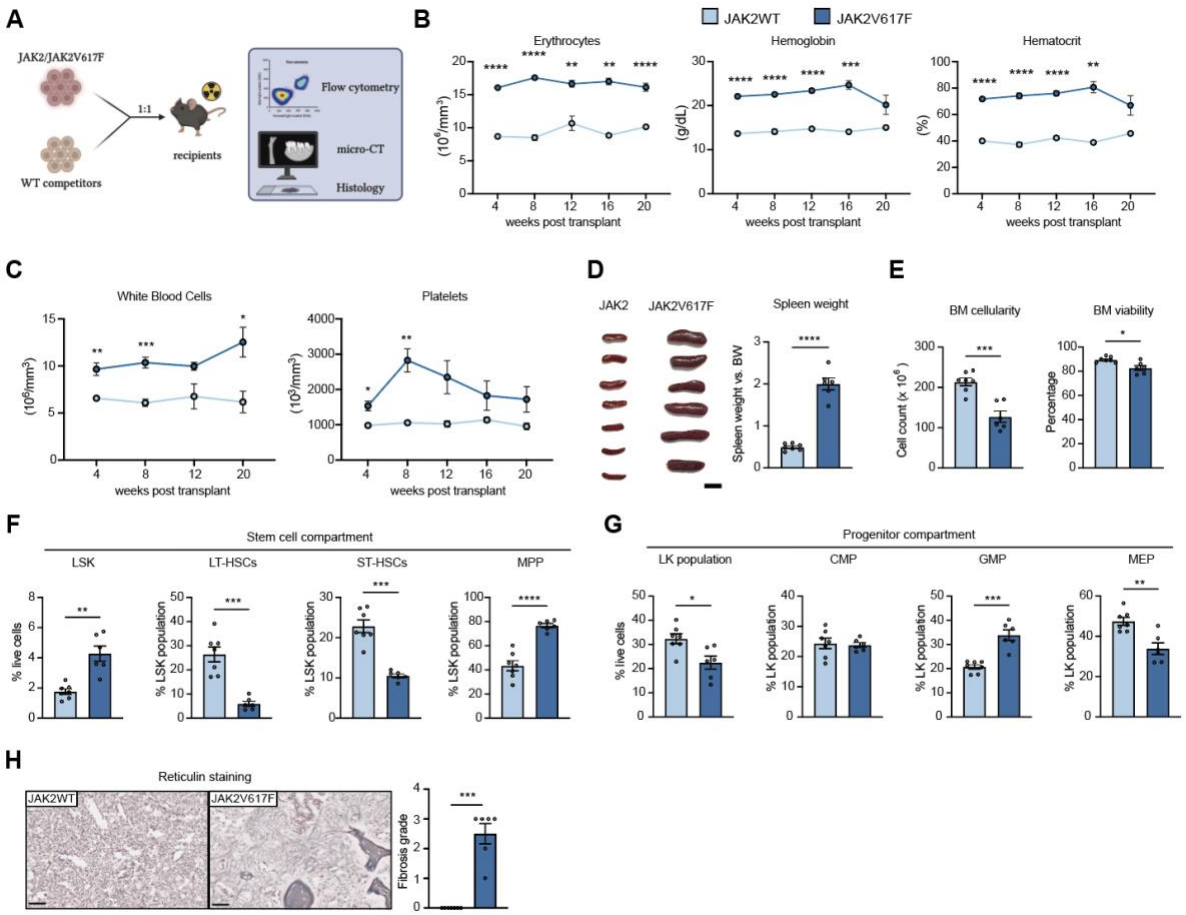

Figure 11: JAK2 murine model recapitulates the clinical post-PV myelofibrosis phenotype.

(A) Schematic representation of the murine competitive bone marrow transplantation model. Whole bone marrow cells isolated from JAK2WT or JAK2V617F donor mice were combined at a 1:1 ratio with wild-type (WT) competitor bone marrow and transplanted into lethally irradiated WT recipient animals. Peripheral blood samples were collected at four-week intervals for flow cytometric analysis, whereas micro–computed tomography (μCT) and histopathological assessments were conducted at 20 and 24 weeks after transplantation. Created in BioRender. Goetz, K. (2026) https://BioRender.com/qcyscry

(B–C) Serial analysis of peripheral blood parameters following transplantation (n = 6 mice per group), demonstrating development of a polycythemia vera (PV)-like phenotype (B) and increased myeloproliferative activity (C). Statistical evaluation was performed using two-way ANOVA with Sidak's multiple-comparison correction.

(D) Representative images of spleens and quantification of spleen weight normalized to body weight (BW) at the experimental endpoint. Scale bar, 1 cm.

(E) Total bone marrow cellularity and proportion of viable bone marrow cells measured at the termination of the experiment.

(F) Flow cytometric analysis of the hematopoietic stem cell (HSC) compartment isolated from mesoderm-derived bones at the endpoint, including $Lin^{-}Sca1^{+}cKIT^{+}$ (LSK) cells, long-term HSCs (LT-HSCs), short-term HSCs (ST-HSCs), and multipotent progenitors (MPPs) in JAK2WT and JAK2V617F mice (n = 6).

(G) Flow cytometric characterization of hematopoietic stem and progenitor cell (HSPC) populations from mesoderm-derived bones at sacrifice, including $Lin^{-}Sca1^{-}cKIT^{+}$ (LK) cells,

common myeloid progenitors (CMPs), granulocyte–macrophage progenitors (GMPs), and megakaryocyte–erythroid progenitors (MEPs) in JAK2WT and JAK2V617F mice (n = 6). **(H)** Representative reticulin-stained BM sections (left) and quantification of reticulin fibrosis grade (right) in JAK2WT and JAK2V617F mice. Scale bar, 100 µm. B-H) was previously included in Atakhanov S., Ghezzi I., Tejeda H. *et al.* BioRxiv 2026[54] .

5.7 *In vivo* model further confirms that MPN alone simultaneously drives two opposing skeletal outcomes: osteosclerosis and bone loss

To resolve how these hematopoietic alterations translate into bone pathology, we performed high-resolution micro–computed tomography (µCT) of mesoderm-derived long bones (femur) and neural crest–derived craniofacial bones (maxilla and mandible). The femur was subdivided into anatomically distinct proximal, distal and growth plate regions, enabling spatial resolution of bone remodeling patterns that are obscured by whole-bone analyses (Figure 12A).

µCT analysis revealed pronounced region-specific differences in bone remodeling within the same bone (femur). JAK2V617F mice developed pronounced osteosclerosis selectively in the proximal femur (Figure 12B,C), whereas the distal region remained largely unaffected (Figure 12D). Although bone volume was increased in the proximal femur, the trabeculae were thinner, indicating that bone resorption remains active even in osteosclerotic marrow. At the same time, the number of trabeculae was markedly increased, suggesting excessive new bone formation.

In contrast, the growth plate region exhibited pronounced bone loss, characterized by decrease in bone volume, thinner trabeculae and resulting in a modest shortening of the femur (Figure 12E-G). This spatial segregation suggests that regions closely coupled to hematopoietic and stromal activity, such as the growth plate and metaphysis, are selectively vulnerable to MPN-driven remodeling. Together, these findings demonstrate that osteosclerosis and bone loss coexist within the same bone but are compartmentalized into distinct, functionally defined niches.

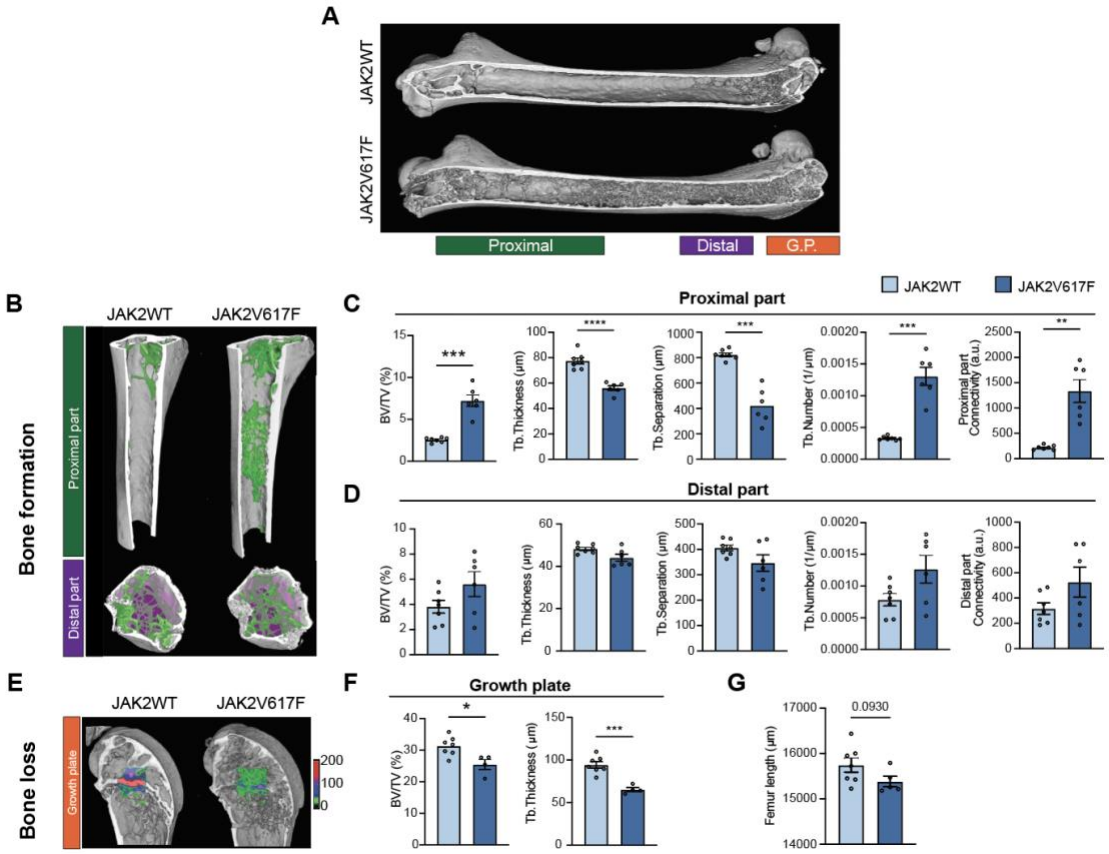

Figure 12: A single oncogenic clone can give rise to two opposing niche-dependent skeletal phenotypes within the same bone.

(A) Representative three-dimensional reconstructions from micro–computed tomography (µCT) highlighting selected anatomical regions of the murine femur for the analysis (n = 6 mice per group).
(B–D) Representative µCT-based 3D images of the femur (B) and quantitative analysis of trabecular (Tb.) bone parameters in the proximal (C) and distal (D) femoral regions.
(E–F) Three-dimensional µCT reconstruction of the femoral growth plate region (E) and corresponding quantification of trabecular bone characteristics within this area (F).
(G) Measurement and three-dimensional assessment of femoral length.
Micro–computed tomography analyses were performed by Dr. Marta Rizk, Department of Orthodontics, RWTH Aachen Hospital. A-G) was previously included in Atakhanov S., Ghezzi I., Tejeda H. *et al.* BioRxiv 2026[54] .

5.8 MPN alone contributes to periodontal disease

To assess whether the identified remodeling mechanisms also affect periodontal tissue integrity, we examined jawbones at 20 and 24 weeks following transplantation. At the 24 week time point, mutant animals exhibited marked periodontal bone deterioration in both jaws, with substantially greater involvement of the maxilla (Figure 13A,B), consistent with population-level associations between MPN and periodontal disease (Figure 7C). In the mandible, bone loss was predominantly confined to the

area surrounding the first molar, whereas the maxilla displayed widespread alveolar resorption affecting all molars, with particularly severe destruction between the first and second molars. Concordantly, the periodontal ligament (PDL), the connective tissue anchoring the tooth to the alveolar bone, was significantly enlarged beneath the first maxillary molar, while the corresponding mandibular region showed bone loss without appreciable PDL expansion (Figure 13C,D).

Histopathological assessment further revealed extensive neovascularization within the PDL of both jaws, accompanied by pronounced disorganization of fibroblast orientation between dentin and alveolar bone (Figure 13E). Such architectural disruption is expected to compromise tooth stability and predispose to eventual tooth loss.

Immunophenotyping of jawbone tissues by flow cytometry demonstrated robust infiltration of myeloid cells, with elevated monocyte frequencies that correlated with a progressive increase in osteoclast numbers over time in both the maxilla and mandible (Figure 13F–J). Additionally, circulating mutant $CD45.1^{+}CD45.2^{-}CD11b^{+}$ myeloid cells were significantly enriched in peripheral blood (Figure 13K), supporting the notion that osteoclast expansion may originate from the neoplastic hematopoietic clone and actively contribute to periodontal disease progression.

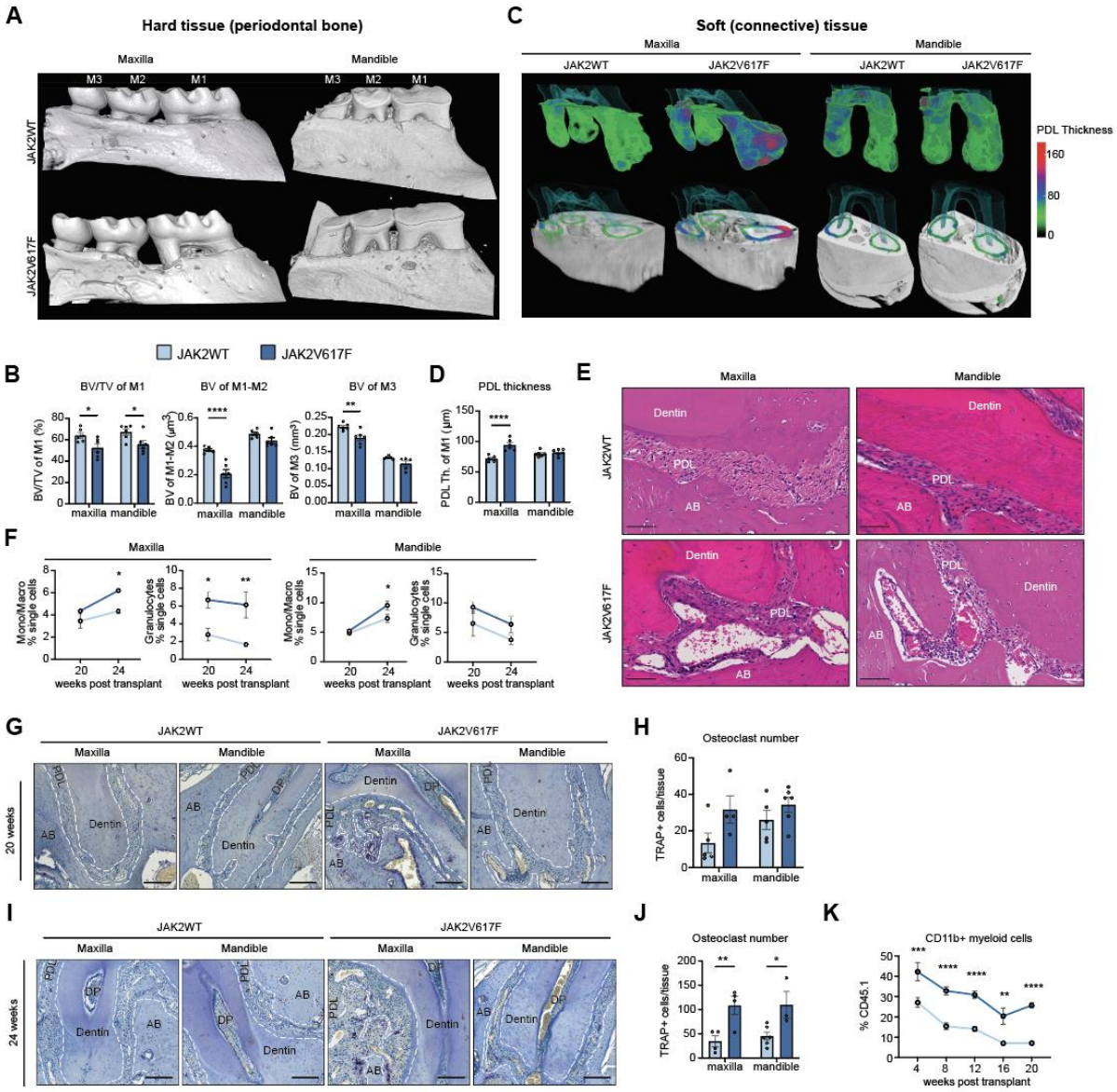

Figure 13: MPN drives periodontal bone remodeling.

(A–B) Representative three-dimensional micro–computed tomography (μCT) reconstructions of maxillary and mandibular bones from JAK2WT and JAK2V617F mice (n = 6) (A), together with quantitative analysis of bone volume in defined regions of interest including molar 1 (M1), the inter-molar space between molars 1 and 2 (M1–M2), and molar 3 (M3) (B) at 24 weeks after transplantation. μCT analyses were performed by Dr. Marta Rizk, Department of Orthodontics, RWTH Aachen Hospital.
(C–D) Representative three-dimensional μCT images showing periodontal ligament (PDL) thickness beneath molar 1 in the maxilla and mandible of JAK2WT and JAK2V617F mice (C), along with quantitative measurements (D) at 24 weeks post-transplantation. μCT analyses were performed by Dr. Marta Rizk, Department of Orthodontics, RWTH Aachen Hospital.
(E) Representative hematoxylin and eosin (H&E) staining of periodontal ligament regions in maxillary and mandibular tissues from JAK2WT and JAK2V617F mice. Scale bar, 100 μm.
(F) Flow cytometric quantification of myeloid cell populations in maxillary and mandibular tissues over time, including monocytes/macrophages ($CD11b^{+}Gr1^{-}$) and granulocytes

(CD11b^{+}Gr1^{+}), in JAK2WT and JAK2V617F mice (n = 6). Statistical analysis was performed using two-way ANOVA with Sidak's multiple-comparison correction.
(G–J) Representative tartrate-resistant acid phosphatase (TRAP) staining of periodontal tissues and quantification of TRAP-positive osteoclasts per tissue area in JAK2WT and JAK2V617F mice at 20 weeks (G–H) and 24 weeks (I–J) following transplantation. Scale bar, 50 µm. PDL, periodontal ligament; DP, dental pulp; AB, alveolar bone. Statistical comparisons were conducted using two-way ANOVA with Sidak's correction.
(K) Flow cytometric analysis of circulating mutant myeloid cells (CD45.1^{+}CD45.2^{-}CD11b^{+}) in peripheral blood over time. Data were analyzed using two-way ANOVA followed by Sidak's multiple-comparisons test. A-K) was previously included in Atakhanov S., Ghezzi I., Tejeda H. *et al.* BioRxiv 2026[54] .

5.9 Single-cell RNA sequencing to dissect the hematopoietic programs underlying the MPN-driven periodontitis

To dissect the mechanism of JAK2V617F-driven periodontal remodelling, we performed scRNA-seq on sorted cells from maxillae and mandibles of JAK2V617F and control mice (Figure 14A). Across conditions, we profiled 15,790 cells spanning the major cellular constituents of the periodontium, generating a comprehensive single-cell mapping of murine maxillary and mandibular tissues. Unsupervised clustering and dimensionality reduction identified 11 major populations comprising 45 subclusters, including neurons (immature, mature neurons, olfactory sensory neurons, sensory-related neurons, CD36+ olfactory neurons), endothelial cells (arterial, sinusoidal, vascular, olfactory, inflammatory endothelial cells and developing arterial endothelial cells), epithelial (specialized, gingival, secretory, progenitor epithelium, ameloblasts, enamel forming ameloblasts, solitary chemosensory cells), stromal cells (progenitor stroma, neural crest MSCs, fibroblasts, neuroendocrine cells, chondrocytes, osteoblasts), hematopoietic progenitor cells (pro-/pre-B cells, B cell progenitors, EBM progenitors), B cells (mature, proliferating, naive, memory, immature B cells, plasma cells), T cells (regulatory, CD8+ T cells, natural killer cells, T helper cells), monocytes/macrophages/dendritic cells (Ly6C+ macrophages, Ly6C+ monocytes, proliferating monocytes, cDC1, cDC2) and neutrophils (neutrophil progenitors, neutrophils, proliferating neutrophils) (Figure 14B-D).

We next applied Augur to rank cell states most perturbed by MPN-driven periodontal remodelling. Mono/macrophage/dendritic cell (mono/macro/DC) populations and stromal cells emerged as the two most responsive compartments (Figure 14E), consistent with our patient-derived data (Figure 8G).

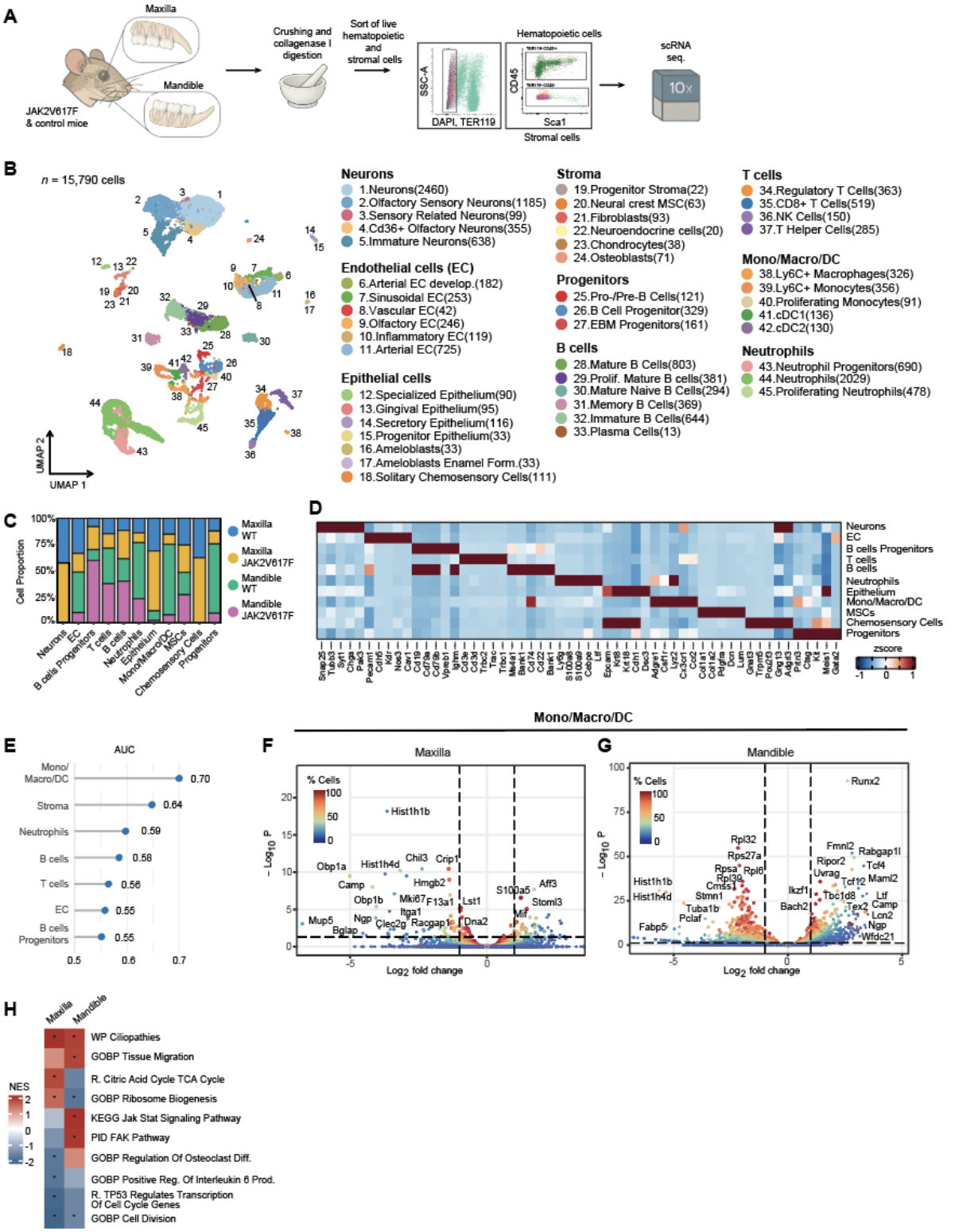

Figure 14: Single-cell characterization of the hematopoietic cells in the MPN-driven periodontal remodeling.

(A) Schematic representation of the workflow for isolation and enrichment of hematopoietic and stromal cell populations from maxillary and mandibular bones of JAK2WT and JAK2V617F mice for single-cell RNA sequencing analysis. Schematic created with ChatGPT.

(B) UMAP visualization of the integrated single-cell transcriptomic dataset derived from both jawbones under JAK2WT and JAK2V617F conditions, comprising 15,790 cells segregated into 45 transcriptionally distinct subclusters based on high-resolution annotation.
(C) Distribution of broadly annotated cell populations across experimental conditions.
(D) Mean expression levels of the top five marker genes defining the major cellular populations.
(E) Cell-type prioritization analysis using Augur across broadly defined cell populations from both jawbones, identifying the cell types most transcriptionally affected in JAK2V617F samples relative to JAK2WT controls. AUC, area under the curve.
(F–G) Volcano plots showing differentially expressed genes in monocyte/macrophage/dendritic cell populations from the maxilla (F) and mandible (G), comparing JAK2V617F and JAK2WT conditions.
(H) Pathway enrichment analysis of mono/macro/DC populations in maxillary and mandibular tissues comparing JAK2V617F and JAK2WT conditions. Functional enrichment was performed using Reactome, Gene Ontology (GO), WikiPathways, KEGG, BioCarta, and PID databases.
Bioinformatic analyses were carried out by Dr. Hector Tejeda Mora, Department of Developmental Biology, Erasmus Medical Center. A-H) was previously included in Atakhanov S., Ghezzi I., Tejeda H. *et al.* BioRxiv 2026[54] .

DEG analysis of mono/macro/DC populations revealed striking site-specific transcriptional reprogramming. In the maxilla, these cells exhibited significant upregulation of osteoclastogenic genes (*Stoml3, MIF*), accompanied by downregulation of osteogenic programs (*Bglap, Chil3, Crip1*) and cell-cycle–associated genes (*Mki67*), indicating a shift toward a resorptive, non-proliferative state (Figure 14F). In contrast, mono/macro/DCs from the mandible displayed a distinct transcriptional signature characterized by broad downregulation of ribosomal genes (*Rpl32, Rps27a, Rpsa, Rpl6, Rpl39*) alongside upregulation of inflammatory, lineage-priming, and fate-determining transcriptional regulators (*Tcf4, Tcf12, Lcn2, Ngp, Maml2*) (Figure 14G). Pathway enrichment analysis further revealed increased signatures associated with ciliopathies, tissue migration, mitochondrial and ribosomal metabolism, coupled with suppression of pathways regulating osteoclast differentiation, positive regulation of interleukin-6 production, TP53-dependent cell-cycle control, and cell division (Figure 14H).

5.10 Periodontal stromal cells adopt ectopic chondrogenic fate in response to mutant hematopoiesis

Given that neuronal cells represented the most abundant niche population recovered in our murine scRNAseq dataset, we next focused on characterizing neuronal

responses in greater detail. Pathway-level analysis of neuronal transcriptional profiles revealed strong enrichment of oxidative phosphorylation, mitochondrial metabolic activity, inflammatory signaling cascades, neuropathic pathways, and proteasome-mediated degradation of GLI1 (Figure 15A). These alterations are consistent with prior reports describing neuropathic features associated with myeloproliferative neoplasms[56], supporting the presence of disease-induced neuronal stress and dysfunction.

We subsequently examined periodontal stromal cells, which emerged as the second most transcriptionally perturbed compartment based on Augur prioritization. Ontogeny-specific markers confirmed that stromal cells within the periodontal compartment originate from neural crest progenitors and are therefore developmentally distinct from stromal populations in axial and appendicular skeletons, which derive from mesodermal lineages (Figure 15B). This ontogenetic distinction highlights fundamental biological differences between craniofacial bones and long bones.

Comparative transcriptional analyses uncovered pronounced regional divergence in stromal cell responses between the maxilla and mandible. Stromal cells from the maxilla exhibited marked suppression of osteogenic gene programs, including *Bglap, Bglap2, Bmp4, Ptch1, Ptn,* and *Tgfbi*. In parallel, these cells upregulated fibro-inflammatory genes (such as *Nfkb1, Fmod, Col9a2,* and *Thbs1*), pro-osteoclastogenic mediators (including *Ccn2* and *Omd*), and a suite of genes typically associated with chondrocytes (*Acan, Cytl1, Cnmd, Chadl, Mia, Matn1, Snorc,* and *Mmp13*) (Figure 15C). In contrast, mandibular stromal cells displayed reduced expression of inflammatory and stress-response regulators (including *Nfkbia, Tnfrsf12a, Dusp1,* and *Pdpn*), alongside diminished expression of structural musculoskeletal genes such as *Sparcl1* and *Mustn1*. Instead, mandibular stromal cells preferentially upregulated pathways supporting myeloid cell recruitment and vascular stabilization, including *Cxcl12, Igf1, Angpt1,* and *Adgrg6* (Figure 15D), in agreement with our histological and immunophenotypic observations.

These regional differences were further supported by pathway enrichment analyses, which demonstrated enhanced extracellular matrix remodeling, activation of endochondral ossification programs associated with skeletal dysplasia, and

enrichment of inflammatory and fibrotic signaling in maxillary stromal cells. Concurrently, pathways related to cellular stress adaptation, including responses to nutrient deprivation and nonsense-mediated RNA decay, were suppressed (Figure 15E).

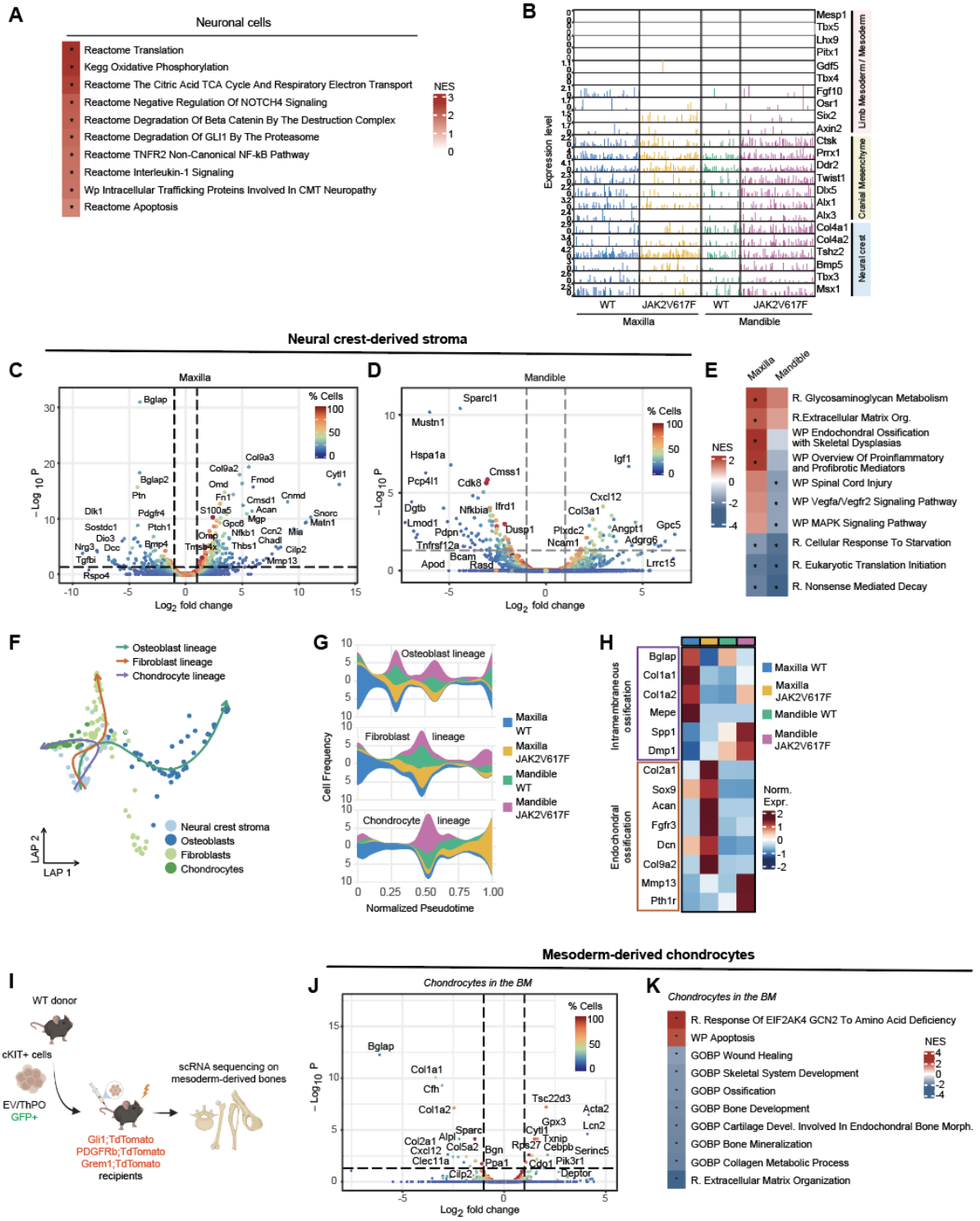

Figure 15: Single-cell profiling of periodontal stromal cells in MPN identifies shared osteochondral injury programs across ontogenetically distinct skeletal compartments.

(A) Functional pathway enrichment analysis of neuronal populations from the maxilla comparing JAK2V617F and JAK2WT conditions. Enrichment analysis was conducted using Reactome, Gene Ontology (GO), WikiPathways, KEGG, BioCarta, and PID databases.
(B) Tracksplot showing the expression patterns of neural crest–, cranial mesenchyme–, and mesoderm-associated marker genes in maxillary and mandibular tissues under both JAK2WT and JAK2V617F conditions.
(C–D) Volcano plots depicting differentially expressed genes in stromal cell populations from the maxilla (C) and mandible (D), comparing transcriptional profiles between JAK2V617F and JAK2WT samples.
(E) Pathway enrichment analysis of stromal cell populations in maxillary and mandibular tissues comparing JAK2V617F and JAK2WT conditions. Functional enrichment was performed using Reactome, Gene Ontology (GO), WikiPathways, KEGG, BioCarta, and PID databases.
(F) Trajectory analysis of stromal subpopulations from jawbone tissues using Slingshot, illustrating inferred lineage relationships overlaid on dimensionality reduction embeddings.
(G) Stream plot visualization showing condition-dependent changes in stromal lineage dynamics, with pseudotime trajectories normalized across experimental groups.
(H) Comparative analysis of ossification-related gene expression signatures in stromal cells from maxillary and mandibular tissues across conditions.
(I) Experimental design of the murine thrombopoietin (ThPO)-induced myelofibrosis model. c-Kit–enriched hematopoietic stem cells from wild-type donors were lentivirally transduced with ThPO or empty vector (EV) and transplanted into inducible CreER;tdTomato reporter mice (Gli1;tdTomato, Pdgfrb;tdTomato, and Grem1;tdTomato). After tamoxifen administration and lethal irradiation, donor cells were infused intravenously. TdTomato-positive stromal cells were isolated from mesoderm-derived skeletal sites for single-cell RNA sequencing, while tibial samples from the same cohorts were subjected to Visium spatial transcriptomic analysis. Data was re-analyzed from our previously published study[33]. Created in BioRender. Goetz, K. (2026) https://BioRender.com/zig5rs1
(J) Volcano plot showing differential gene expression in chondrocyte populations from mesoderm-derived bones (including femur, tibia, hip, and spine) comparing fibrotic (ThPO) and control (EV) conditions.
(K) Pathway enrichment analysis of mesoderm-derived chondrocytes comparing fibrotic (ThPO) and control (EV) conditions. Functional enrichment was performed using Reactome, Gene Ontology (GO), WikiPathways, KEGG, BioCarta, and PID databases.
Bioinformatic analyses were performed by Dr. Hector Tejeda Mora, Department of Developmental Biology, Erasmus Medical Center. A-H) and J-K) was previously included in Atakhanov S., Ghezzi I., Tejeda H. *et al.* BioRxiv 2026[54] .

The unexpected activation of chondrocyte-associated transcriptional programs within maxillary stromal cells prompted further investigation. Under physiological conditions, the maxillary periodontal bone develops exclusively through intramembranous ossification and does not contain chondrocytes. However, the consistent enrichment of chondrocyte markers and endochondral ossification signatures across both patient-derived and murine datasets suggested a pathological deviation in stromal cell fate.

To explore this further, we performed trajectory inference and pseudotime analyses of stromal subpopulations, which identified three neural crest–derived differentiation trajectories corresponding to osteoblastic, fibroblastic, and chondrogenic lineages (Figure 15F). While osteoblast and fibroblast trajectories were present under all experimental conditions, the chondrogenic trajectory emerged exclusively in the context of JAK2V617F-driven hematopoietic stress (Figure 15G). This finding indicates that ectopic chondrogenesis represents a disease-induced stromal response to mutant hematopoiesis.

To characterize the ossification programs underlying this fate shift, we curated gene signatures associated with intramembranous and endochondral bone formation. In control conditions, maxillary stromal cells retained a craniofacial-specific intramembranous ossification program. In contrast, stromal cells exposed to JAK2V617F-mutant hematopoiesis adopted a chondrocyte-like transcriptional state and activated endochondral ossification machinery within the periodontal niche (Figure 15H).

Given the pronounced defects observed in femoral growth plates (Figure 12E,F) and our prior single-cell analyses demonstrating expansion of a proliferative chondrocyte trajectory during murine myelofibrosis[33], we next examined whether mesoderm-derived chondrocytes exhibit analogous pathological reprogramming. To this end, we reanalyzed previously published scRNA sequencing datasets generated from sorted TdTomato^{+} stromal cells obtained using three independent Cre-reporter lines (Pdgfrb;tdTomato, Gli1;tdTomato, and Grem1;tdTomato). These datasets encompass both thrombopoietin (ThPO)-induced marrow fibrosis and control conditions (Figure 15I).

Focusing specifically on the chondrocyte compartment, differential expression analysis revealed substantial suppression of osteogenic and bone-supportive genes, including *Bglap, Col1a1, Clec11a,* and *Sparc*, along with reduced expression of the key hematopoietic niche factor *Cxcl12* (Figure 15J). Simultaneously, these chondrocytes upregulated fibro-inflammatory and immunomodulatory programs, such as *Acta2, Lcn2, Tsc22d3, Cytl1,* and *Txnip*, consistent with an injury-associated chondrocyte phenotype. Notably, this transcriptional signature closely mirrored that of the ectopic neural crest–derived chondrocytes identified in the maxillary periodontal

niche, including shared downregulation of *Bglap* and induction of *Cytl1*, genes known to suppress osteogenesis and promote osteoclastogenesis[57]. These findings suggest convergence toward a common osteochondral injury response despite distinct developmental origins.

Pathway enrichment analysis further supported this interpretation, revealing broad suppression of skeletal development, ossification, and cartilage programs involved in endochondral bone formation, alongside activation of apoptotic pathways characteristic of degenerative chondrogenesis observed in osteoarthritis (Figure 15K). Together, these data provide a mechanistic framework linking aberrant chondrocyte states to bone-destructive remodeling in myelofibrosis and establish pathological chondrogenesis as a shared feature across ontogenetically distinct skeletal compartments.

5.11 Ectopic periodontal chondrocytes in MPN interact with myeloid cells via Thbs1-CD47 axis

After delineating cell-intrinsic transcriptional changes and lineage shifts in the most affected cellular compartments during MPN-associated periodontal remodeling, we next investigated how these alterations influence intercellular communication within the periodontal microenvironment. To systematically reconstruct cell–cell interaction networks, we applied CellChat to datasets from both maxillary and mandibular tissues (Figure 16A,B). This analysis revealed prominent communication hubs within the neuronal and endothelial compartments under JAK2V617F-driven conditions, characterized by markedly increased signaling intensity. In combination with the previously observed enrichment of inflammatory and neuropathic pathways (Figure 15A), these results point toward a highly active neurovascular signaling axis contributing to periodontal pathology in MPN.

In addition, stromal populations in both jaws emerged as major outgoing signaling centers, indicating that they function as key orchestrators of pathogenic niche interactions during disease progression (Figure 16A,B). Given this dominant signaling role, we examined whether stromal cells actively shape myeloid behavior through defined ligand–receptor interactions.

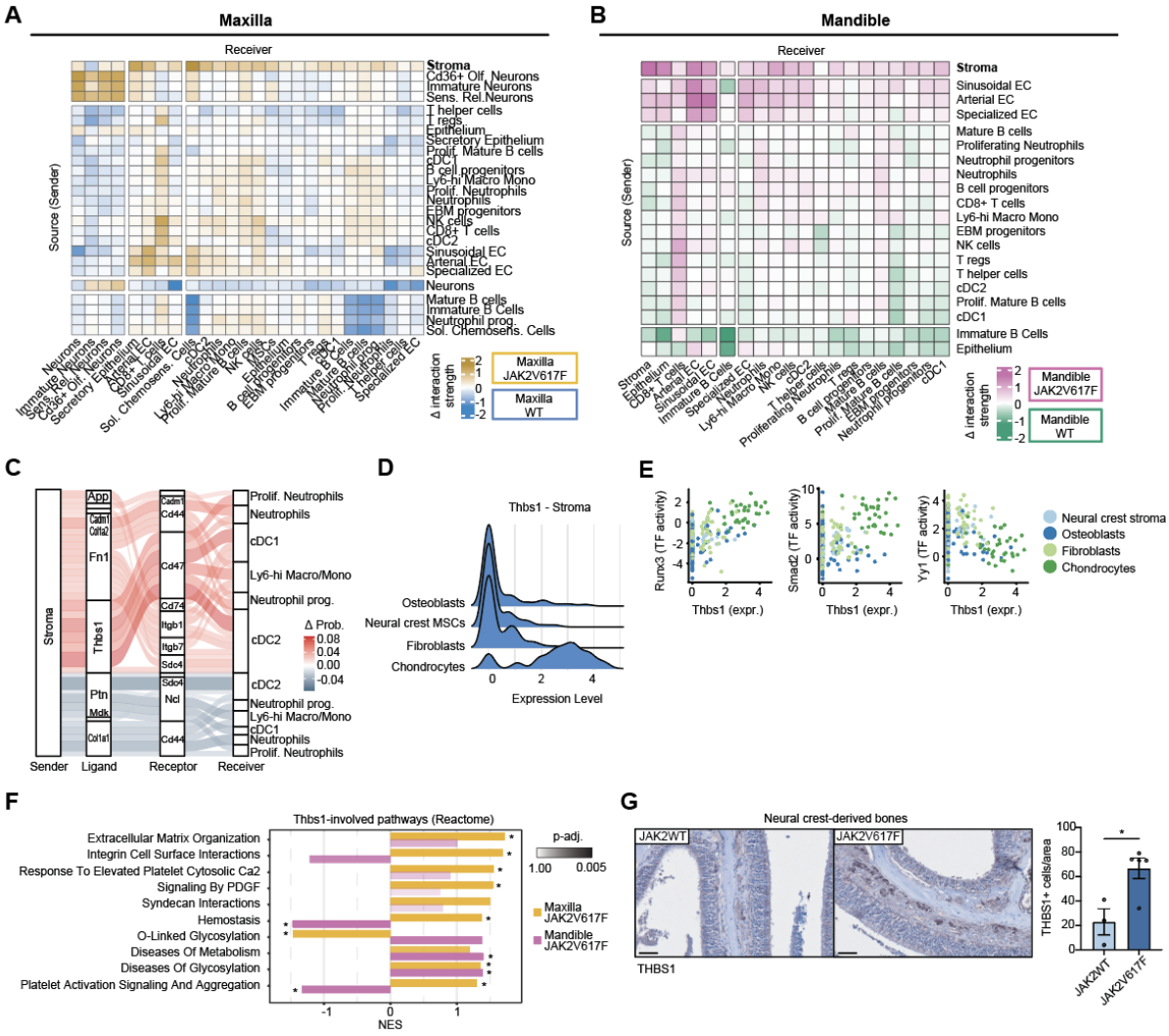

Figure 16: Ectopic periodontal osteochondral stromal cells interact with myeloid cells via Thrombospondin 1 (Thbs1)-CD47 axis.

(A–B) CellChat-derived intercellular communication networks inferred from paired maxillary (A) and mandibular (B) tissues, comparing signaling interactions between JAK2V617F and JAK2WT conditions.
(C) Predicted ligand–receptor interactions between maxillary stromal cells (sender population) and myeloid cells (receiver population), displayed according to changes in mean interaction probability between JAK2V617F and JAK2WT samples.
(D) Expression profile of thrombospondin-1 (Thbs1) across transcriptionally defined stromal subpopulations in the maxilla.
(E) Transcription factor regulatory analysis of murine neural crest–derived stromal subclusters, illustrating transcription factors (TF) positively or negatively associated with normalized *THBS1* expression.
(F) Pathway enrichment analysis of THBS1-associated signaling pathways comparing JAK2V617F and JAK2WT conditions in maxillary and mandibular tissues. Functional enrichment was performed using the Reactome database. Bioinformatic analyses were conducted by Dr. Hector Tejeda Mora, Department of Developmental Biology, Erasmus Medical Center.
(G) Representative images of THBS1 immunostaining in maxillary bone from JAK2WT and JAK2V617F mice, with quantification of THBS1-positive cells normalized to tissue area. Scale

bars, 50 μm. A-G) was previously included in Atakhanov S., Ghezzi I., Tejeda H. *et al.* BioRxiv 2026[54] .

Interaction modeling identified a strong and selective communication axis between stromal and myeloid cells mediated by thrombospondin-1 (Thbs1) and its receptor CD47 (Figure 16C). *Thbs1* transcripts were substantially elevated in maxillary stromal cells during periodontal bone remodeling (Figure 15C), consistent with earlier observations implicating *Thbs1* in aberrant mutant megakaryocyte-stromal interactions in myelofibrosis patients[32].

Subcluster-level analysis of stromal populations demonstrated that *Thbs1* expression was particularly enriched within the ectopic chondrocyte-like cells (Figure 16D), identifying these injury-associated stromal cells as a principal source of pathogenic signaling within the periodontal niche. To further elucidate upstream regulatory mechanisms, we employed ColecTRI to infer transcription factor networks associated with *Thbs1* expression. RUNX3 and SMAD2, downstream mediators of TGF-β signaling, showed positive associations with *Thbs1* expression in chondrocytes, whereas YY1 exhibited a negative correlation (Figure 16E). Functional enrichment analysis of Thbs1-high chondrocytes revealed activation of extracellular matrix remodeling pathways, integrin-dependent cell adhesion programs, platelet calcium signaling responses, and metabolic stress pathways (Figure 16F), collectively consistent with a pro-fibrotic and maladaptive stromal phenotype.

To confirm these transcriptional findings at the protein level, we assessed Thbs1 expression within periodontal tissue sections. In the maxilla, Thbs1-positive cells were prominently localized in subendosteal and peritrabecular regions (Figure 16G), supporting the involvement of Thbs1-expressing stromal populations within the peritrabecular niche during MPN-associated periodontal remodeling.

5.12 Thbs1 upregulation in mesoderm-derived bones identifies a unifying remodeling axis in myelofibrosis

Because chondrocytes derived from neural crest and mesoderm-origin bones displayed a convergent osteochondral injury signature (Figure 15C,J), we next investigated whether induction of Thbs1 in stromal populations represents a shared remodeling response across skeletal compartments in myelofibrosis. To test this, we

revisited our previously generated scRNAseq datasets from the ThPO overexpression model and corresponding empty vector (EV) controls (Figure 15I). In these datasets, TdTomato^{+} stromal cells were isolated from mesoderm-derived skeletal sites, including femur, tibia, pelvis, and vertebrae, allowing detailed characterization of mesoderm-derived stromal remodeling during fibrotic transformation.

Within 17 transcriptionally defined stromal subclusters, *Thbs1* expression was broadly upregulated under myelofibrotic conditions. The most pronounced induction was observed in CXCL12-abundant reticular (CAR1/2) cells, a fibroblast subset (FB2), and multiple osteolineage clusters (OLC1–3) (Figure 17A). Importantly, both chondrocytes and pre-chondrocyte populations exhibited particularly strong *Thbs1* expression in fibrotic marrow, reinforcing the notion that stromal cells across ontogenetically distinct bones converge toward a Thbs1-high osteochondral injury state. In the craniofacial context, this aligns with the emergence of ectopic Thbs1-expressing chondrocytes following periodontal injury.

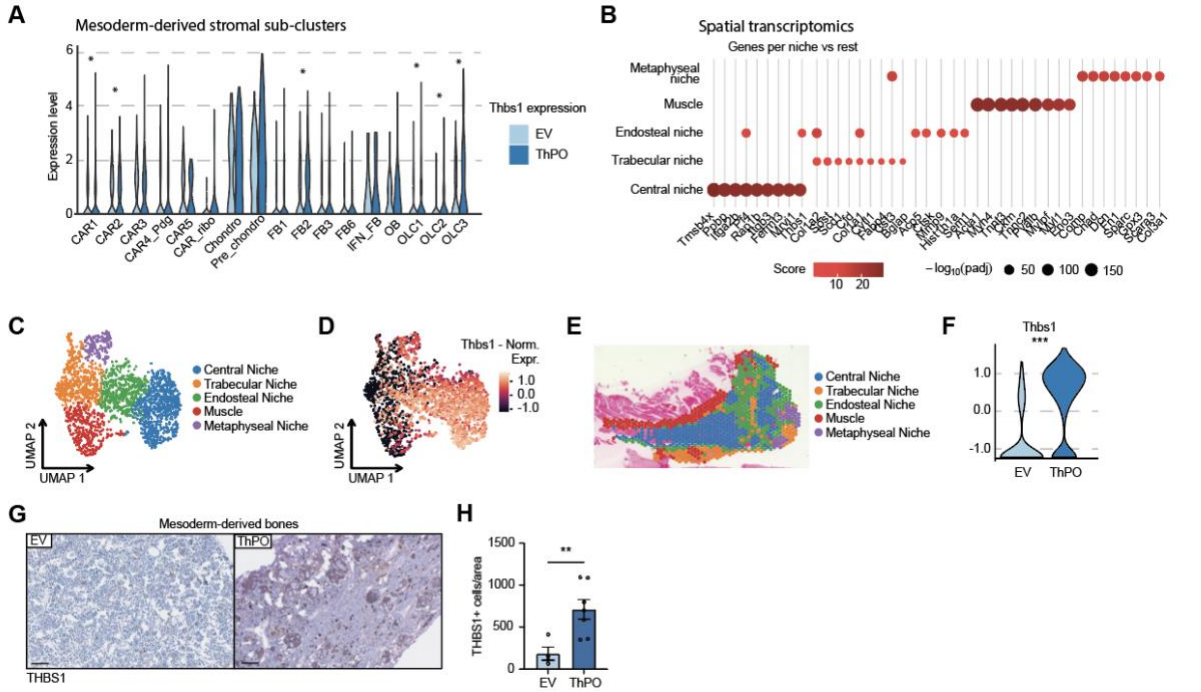

Figure 17: Conserved Thbs1 upregulation across mesoderm-derived stromal niches in myelofibrosis.

(A) Single-cell RNA sequencing analysis showing THBS1 expression across 17 transcriptionally defined stromal subpopulations in mesoderm-derived bones under fibrotic (ThPO) and control (EV) conditions. Analysis was performed by Dr. Hector Tejeda Mora, Department of Developmental Biology, Erasmus Medical Center.

(B) Mean expression levels of marker genes defining five spatially annotated domains identified by Visium spatial transcriptomics. Spatial transcriptomic analysis was performed by Lina Schmidt, Institute of Cell and Tumor Biology, RWTH Aachen Hospital.
(C–D) UMAP visualization of integrated Visium spatial transcriptomics datasets from tibial samples of ThPO-treated and control (EV) mice (n = 3 per group), highlighting five major spatial regions (C) and their associated Thbs1 expression patterns (D).
(E) Representative overlay of hematoxylin and eosin (H&E) staining with spatial domain annotations in tibial sections derived from Visium spatial transcriptomics (n = 3 per group).
(F) Spatial distribution of Thbs1 expression across tibial tissue sections under fibrotic (ThPO) and control (EV) conditions, based on Visium spatial transcriptomics analysis.
(G–H) Representative immunostaining of Thbs1 in tibial bone sections from fibrotic (ThPO) and control (EV) groups (G), along with quantification of Thbs1-positive cells normalized to tissue area (H). Scale bars, 50 µm. A-H) was previously included in Atakhanov S., Ghezzi I., Tejeda H. *et al.* BioRxiv 2026[54] .

To determine the anatomical distribution of Thbs1 expression, we analyzed Visium spatial transcriptomics data generated from the same ThPO and control cohorts. Unbiased clustering resolved five spatially distinct marrow domains: central marrow, trabecular region, endosteal zone, metaphysis, and muscle-adjacent areas (Figure 17B,C). *Thbs1* transcripts were preferentially enriched within central, endosteal, and metaphyseal compartments (Figure 17C,D). Integration with hematoxylin–eosin–stained sections localized the Thbs1-enriched endosteal region to the growth plate and metaphyseal areas, and was markedly elevated in ThPO-induced fibrosis (Figure 17E,F).

Protein-level validation confirmed increased numbers of Thbs1-positive cells in mesoderm-derived bones during myelofibrosis. In long bones, *Thbs1* expression was prominent within the fibrotic interstitium and was also detected at high levels in dysplastic megakaryocytes, consistent with prior reports linking *Thbs1* to inflammaging and myeloid skewing[58].

Taken together, these findings demonstrate that Thbs1 upregulation represents a conserved stromal response across developmentally distinct skeletal compartments in MPN.

5.13 Systemic and stage-dependent activation of the Thbs1 axis in human MPN

To evaluate the translational relevance of Thbs1 signaling, we next examined its expression patterns and functional interactions in human samples. Using our human scRNAseq dataset derived from dental tissues, we assessed *Thbs1* expression across nine stromal subpopulations. Tooth fibroblasts, previously identified as the third transcriptionally perturbed stromal subset in MPN (Figure 8G), displayed significantly elevated *Thbs1* expression specifically in MPN samples, whereas neither periodontitis alone nor healthy controls showed comparable induction (Figure 18A). A neural crest–derived stromal subset also demonstrated a tendency toward increased *Thbs1* expression under MPN conditions. Cell–cell communication analysis also revealed that *Thbs1*-expressing tooth fibroblasts engaged in selective and strengthened interactions with osteoclast populations uniquely in the MPN setting (Figure 9E).

Ligand–receptor modeling identified conserved stromal-to-myeloid communication through Thbs1–CD36 and Thbs1–CD47 axes within human periodontal tissues (Figure 18B), mirroring observations in murine models. These findings support a conserved role for Thbs1-mediated stromal–myeloid crosstalk in MPN-associated periodontal bone remodeling.

To determine whether Thbs1 upregulation also occurs in mesoderm-derived skeletal sites in humans, we analyzed pelvic bone marrow biopsies from MPN patients. Due to limited stromal recovery in human single-cell MF datasets, we performed immunohistochemical staining for Thbs1 on formalin-fixed, paraffin-embedded bone marrow sections from MPN patients (n=7) and healthy donors (n=3). Control marrow samples exhibited preserved architecture with normal adipocyte content and minimal Thbs1 staining. In contrast, fibrotic marrow samples displayed reduced cellularity, extensive fibrosis, and marked accumulation of Thbs1-positive cells (Figure 18C,D).

To investigate whether Thbs1 signaling extends beyond local skeletal niches, we quantified circulating Thbs1 and its receptor partner CD47 in plasma from MPN patients and healthy controls using ELISA. Both proteins were significantly elevated in the peripheral blood of MPN patients (Figure 18E–G), indicating that the Thbs1–CD47 axis is not confined to local bone microenvironments but is systemically active. These

data suggest that circulating Thbs1 may function as a mediator linking hematopoietic pathology to skeletal remodeling.

Collectively, these observations demonstrate that Thbs1 is increased both locally within stromal niches and systemically in MPN. Importantly, Thbs1-positive stromal populations emerge in both neural crest–derived and mesoderm-derived bones across murine and human disease contexts.

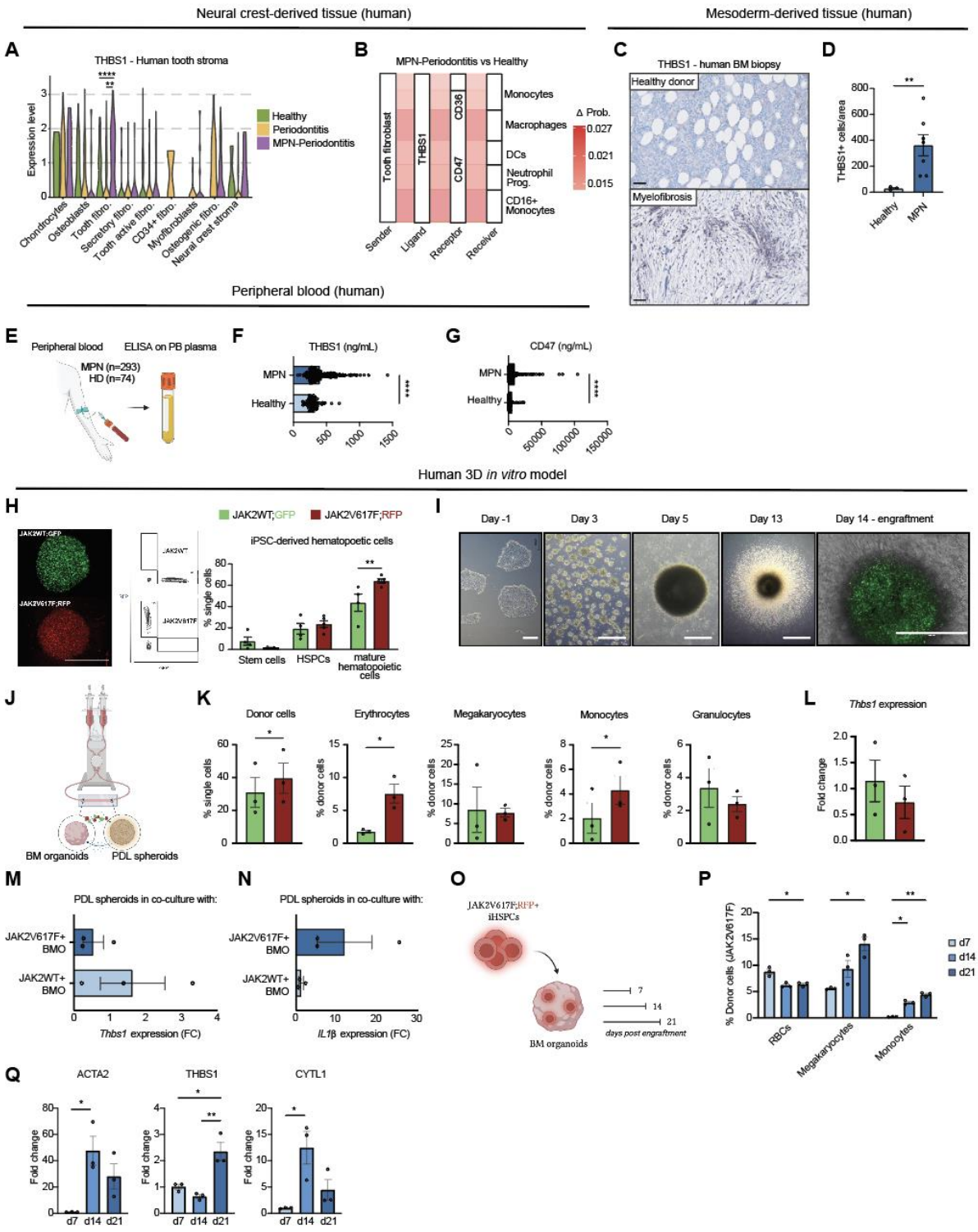

Figure 18: Human validation of Thbs1 as a central mediator of MPN-associated stromal remodeling across ontogenetically distinct tissues.

(A) *Thbs1* expression levels across nine transcriptionally defined periodontal stromal subpopulations derived from human tooth biopsies of MPN-associated periodontitis (n = 3), periodontitis without MPN (n = 3), and healthy control samples (n = 1). Stromal subclusters are arranged according to Augur-based cell-state prioritization from left to right.
(B) Predicted ligand–receptor interactions between patient-derived tooth fibroblast populations (sender cells) and myeloid cells (receiver cells). Interaction strength is displayed

based on changes in mean interaction probability between MPN-associated periodontitis (n = 3) and healthy controls (n = 1). Bioinformatic analyses were performed by Dr. Hector Tejeda Mora, Department of Developmental Biology, Erasmus Medical Center.
(C–D) Representative immunostaining of Thbs1 in bone marrow biopsy specimens from MPN patients (n = 7) and healthy donors (n = 3) (C), together with quantification of THBS1-positive cells normalized to tissue area (D). Scale bars, 50 µm.
(E) Diagram illustrating the experimental workflow for peripheral blood collection from MPN patients (n = 293) and healthy individuals (n = 74) for plasma-based ELISA measurements. Created in BioRender. Atakhanov, S. (2026) https://BioRender.com/julw4sm
(F–G) Plasma protein levels of Thbs1 (F) and its interaction partner CD47 (G) measured by ELISA in MPN patients and healthy controls.
(H) Immunofluorescence imaging and representative flow cytometry plots of JAK2V617F;RFP (red) and isogenic JAK2WT;GFP (green) induced pluripotent stem cells (iPSCs), including their directed differentiation toward hematopoietic lineages. Scale bar, 1000 µm. Statistical analysis was performed using two-way ANOVA with Sidak's multiple-comparisons test.
(I) Representative images showing differentiation, maturation, and engraftment of HD353.6 iPSC-derived bone marrow organoids with fluorescently labeled donor cells. Scale bars, 500 µm and 1000 µm.
(J) Schematic representation of the microfluidic organ-on-a-chip platform enabling co-culture of bone marrow organoids with periodontal ligament (PDL) fibroblast spheroids. Created in BioRender. Goetz, K. (2026) https://BioRender.com/hgoumrj
(K–L) Flow cytometric quantification of donor-derived hematopoietic cells (K) and quantitative RT-PCR analysis of *Thbs1* expression (L) in bone marrow organoids seven days following co-culture with PDL fibroblast spheroids. Red bars indicate JAK2V617F;RFP-derived cells, and green bars represent JAK2WT;GFP-derived cells.
(M–N) Quantitative RT-PCR measurements of *Thbs1* (M) and *IL1β* (N) expression in PDL fibroblast spheroids after seven days of co-culture with bone marrow organoids on the microfluidic platform, using organoids engrafted with either JAK2V617F;RFP or JAK2WT;GFP hematopoietic stem and progenitor cells.
(O) Experimental scheme of a three-dimensional in vitro model in which JAK2V617F;RFP-positive iPSCs were differentiated into $CD34^+$ cells and introduced into mature iPSC-derived bone marrow organoids. Organoids were collected at 7, 14, and 21 days following engraftment. Created in BioRender. Goetz, K. (2026) https://BioRender.com/050nfps
(P) Flow cytometric analysis showing frequencies of donor-derived JAK2V617F;RFP-positive erythroid cells, megakaryocytes, and monocytes isolated from bone marrow organoids at 7, 14, and 21 days post-engraftment. Statistical analysis was performed using two-way ANOVA with Tukey's post hoc test.
(Q) Quantitative RT-PCR analysis of gene expression in bone marrow organoid-derived cells collected at 7, 14, and 21 days after engraftment. Statistical evaluation was conducted using one-way ANOVA with Tukey's post hoc correction. A-D), F-I), K-N) and P-Q) were previously included in Atakhanov S., Ghezzi I., Tejeda H. *et al.* BioRxiv 2026[54] .

To determine when during disease evolution Thbs1 induction occurs, we utilized a human bone marrow organoid system previously validated to recapitulate structural and functional features of human bone marrow[53,59]. Organoids were generated using the HD353.6 induced pluripotent stem cell (iPSC) line. To model MPN *in vitro*, we

introduced a previously described patient-derived JAK2V617F iPSC line and its CRISPR-corrected isogenic control (JAK2WT)[46]. For lineage tracking, mutant iPSCs were labeled with RFP and controls with GFP using lentiviral transduction and differentiated into $CD34^+$ hematopoietic stem and progenitor cells (iHSPCs). As expected, JAK2V617F-derived iHSPCs exhibited increased proliferative capacity and altered maturation compared with controls (Figure 18H).

Purified fluorescent $CD34^+$ iHSPCs were engrafted into mature bone marrow organoids (Figure 18I). To model systemic tissue communication, bone marrow organoids were co-cultured with periodontal ligament (PDL) fibroblast spheroids in a microfluidic multi-organ platform, allowing interaction via soluble factors and migratory cells while maintaining physical tissue separation (Figure 18J). PDL fibroblasts were derived from healthy donor wisdom teeth and immortalized to establish a stable human cell line.

After seven days of co-culture, organoids engrafted with JAK2V617F cells displayed increased donor expansion and skewed differentiation toward erythroid and monocytic lineages, recapitulating early polycythemia vera–like features, including monocytosis (Figure 18K). At this early stage, however, *Thbs1* expression within bone marrow organoids remained unchanged between mutant and wild-type conditions (Figure 18L). Similarly, PDL fibroblasts exposed to mutant-engrafted organoids developed a pro-inflammatory transcriptional signature but did not upregulate *Thbs1* (Figure 18M,N). These findings suggest that initial myeloproliferation is insufficient to trigger Thbs1 induction.

We therefore performed longitudinal analyses of organoids engrafted with JAK2V617F cells at 7, 14, and 21 days to capture stage-dependent niche remodeling (Figure 18O). Early time points were dominated by erythroid expansion, consistent with a PV-like phenotype (Figure 18P). With prolonged exposure, however, differentiation progressively shifted toward megakaryocytic and monocytic lineages, two cell types implicated in fibrotic remodeling[32]. Transcriptomic analysis at later stages revealed induction of fibrosis-associated markers, including *ACTA2, THBS1*, and the pathological chondrocyte-related gene *CYTL1*, coinciding with features resembling secondary myelofibrosis (Figure 18Q). Together, these data indicate that *Thbs1* upregulation represents a late-stage, niche-intrinsic response to sustained mutant

hematopoietic stress rather than an immediate consequence of early myeloproliferation.

Overall, the consistent emergence of Thbs1 across developmentally distinct skeletal sites in both murine and human tissues identifies this molecule as a unifying mediator of myelofibrosis-associated skeletal remodeling and a promising candidate for therapeutic targeting.

5.14 Therapeutic targeting of Thbs1 mitigates MPN phenotype in human organoid models

After establishing Thbs1 as a shared stromal mediator bridging osteosclerotic and osteoporotic remodeling across developmentally distinct skeletal compartments, we next tested whether therapeutic interference with Thbs1 signaling could ameliorate the MPN phenotype. Prior studies have described a short peptide, LSKL, derived from the latency-associated peptide (LAP) of TGF-β, which selectively disrupts THBS1-dependent activation of TGF-β without directly blocking canonical TGF-β signaling pathways[60]. Given the enrichment of the extracellular matrix and TGF-β–associated transcriptional programs in Thbs1-expressing stromal populations (Figure 16E,F), we employed LSKL as a pharmacologic inhibitor of Thbs1 activity.

To evaluate its functional impact, we co-engrafted equal numbers of JAK2V617F;RFP and CRISPR-corrected JAK2WT;GFP iHSPCs into mature human bone marrow organoids and subsequently treated them with LSKL or vehicle control (Figure 19A). Under vehicle conditions, mutant cells rapidly established a dominant MPN-like phenotype, characterized by expansion of progenitor compartments, increased erythroid output, and accumulation of megakaryocytic and monocytic populations (Figure 19B). Remarkably, LSKL treatment selectively reduced the frequency of JAK2V617F mutant HSPCs and mitigated erythroid expansion while preserving the wild-type competitor cells. Transcriptomic profiling demonstrated coordinated suppression of fibrotic and inflammatory genes, including *ACTA2, COL1A1,* and *IL1β*, together with reduced expression of *THBS1* and *CD47* (Figure 19C). In addition, chondrogenic markers such as *ACAN* and *SOX9* were diminished, indicating attenuation of the aberrant osteochondral programs that accompany disease

progression. Collectively, these findings indicate that Thbs1 blockade restrains mutant clonal expansion and dampens stromal fibrotic and inflammatory activation.

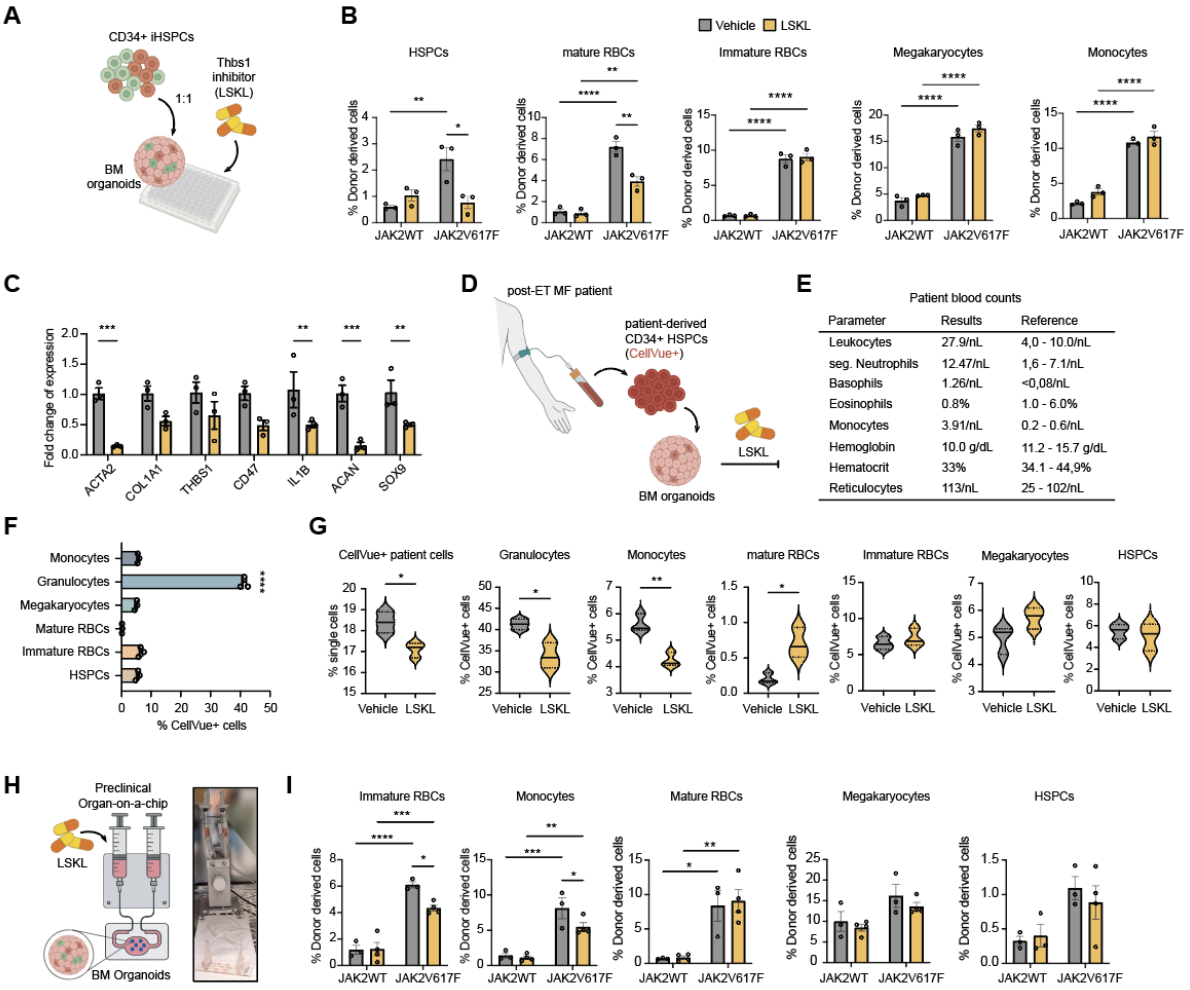

Figure 19: Pharmacological inhibition of Thbs1 suppresses mutant hematopoiesis and fibrosis in human bone marrow organoid model.

(A) Overview of the in vitro bone marrow organoid treatment experiment. Fully differentiated human iPSC-derived bone marrow organoids were competitively engrafted with JAK2V617F;RFP$^+$ and isogenic JAK2WT;GFP$^+$ hematopoietic stem and progenitor cells (iHSPCs) at equal proportions (1:1) and subsequently exposed to the THBS1 inhibitor LSKL or vehicle control under static culture conditions for seven days. Schematic created with ChatGPT.

(B) Flow cytometric quantification of donor-derived hematopoietic populations from bone marrow organoids treated with LSKL or vehicle, showing the relative contribution of mutant and wild-type competitor cells. Statistical analysis was performed using two-way ANOVA with Tukey's post hoc test.

(C) Quantitative RT-PCR analysis of gene expression in bone marrow organoid-derived cells following treatment with LSKL or vehicle control. Statistical comparisons were conducted using two-way ANOVA with Sidak's correction.

(D) Schematic representation of treatment studies using patient-derived primary cells. CD34$^+$ cells isolated from peripheral blood mononuclear cells of a patient with post–essential

thrombocythemia myelofibrosis were labeled with CellVue dye and engrafted into mature iPSC-derived bone marrow organoids, followed by static treatment with LSKL or vehicle for seven days. Schematic created with ChatGPT.
(E) Clinical hematologic parameters of the post-ET MF patient at the time of peripheral blood collection.
(F) Flow cytometric analysis of CellVue-labeled patient-derived cells in vehicle-treated bone marrow organoids, demonstrating a predominance of CD34-derived granulocytic differentiation 7 days after engraftment. Statistical significance was assessed using one-way ANOVA with Dunnett's multiple comparison test.
(G) Flow cytometric evaluation of patient-derived hematopoietic cells following treatment with LSKL or vehicle control.
(H) Diagram of a perfusion-based organ-on-a-chip platform for preclinical drug testing. Bone marrow organoids engrafted with JAK2V617F;RFP and JAK2WT;GFP $CD34^+$ cells were maintained under continuous flow conditions, with LSKL or vehicle administered via the microfluidic circulation system. Schematic created with ChatGPT.
(I) Flow cytometric analysis of hematopoietic lineage output in the organ-on-a-chip model under vehicle or LSKL treatment, showing contributions of mutant and wild-type competitor cells. A-I) was previously included in Atakhanov S., Ghezzi I., Tejeda H. *et al.* BioRxiv 2026[54] .

To assess translational relevance, we next performed *ex vivo* experiments using primary $CD34^+$ hematopoietic stem and progenitor cells obtained from a patient with post–essential thrombocythemia myelofibrosis (post-ET MF) being positive for CALR, MPL and ASXL1 mutations. The patient exhibited marked leukocytosis with granulocytic predominance, circulating blasts, and severe microcytic anemia (Figure 19D,E). Patient-derived $CD34^+$ cells were fluorescently labeled and engrafted into mature bone marrow organoids, followed by treatment with LSKL or vehicle. In vehicle-treated organoids, patient cells reproduced the clinical phenotype, showing strong granulocytic bias and impaired erythroid maturation (Figure 19F). In contrast, LSKL exposure significantly reduced the proportion of patient-derived mutant cells, accompanied by a decrease in granulocytic and monocytic populations (Figure 19G). Notably, erythroid differentiation partially recovered under Thbs1 inhibition, suggesting correction of anemia-associated defects. These results demonstrate that targeting Thbs1 can attenuate pathological myeloid expansion and partially restore erythropoietic balance in primary patient cells.

Because the above experiments relied on static drug exposure, we next developed a microfluidic organ-on-a-chip platform to better simulate systemic drug delivery. In this setup, bone marrow organoids competitively engrafted with JAK2V617F and JAK2WT cells (1:1 ratio) were cultured within a perfusion-enabled chamber, allowing LSKL or vehicle to be delivered exclusively through continuous flow (Figure 19H). Consistent

with static conditions, vehicle-treated organoids developed a robust mutant-driven phenotype marked by expansion of erythroid, monocytic, megakaryocytic, and progenitor populations (Figure 19I). Importantly, perfusion-based LSKL administration significantly suppressed this phenotype, including reduction of erythroid and monocytic outputs. These findings confirm that Thbs1 inhibition effectively constrains mutant hematopoietic dominance under physiologically relevant delivery conditions and highlight the organ-on-a-chip system as a powerful preclinical platform for therapeutic evaluation.

Taken together, these data establish Thbs1 antagonism as a strategy capable of selectively limiting mutant clonal expansion while mitigating fibrosis-associated stromal reprogramming and inflammatory remodeling in MPN.

5.15 Combined JAK2 and Thbs1 inhibition simultaneously ameliorates osteosclerotic and osteoporotic remodeling in two ontogenetically distinct bones

Because bone marrow organoids do not recapitulate a fully mature bone compartment, we next assessed whether Thbs1 inhibition could influence fibrotic progression and skeletal pathology *in vivo*. Clinically approved JAK inhibitors predominantly suppress mutant hematopoietic signaling but fail to ameliorate stromal fibrosis and are therefore not considered disease-modifying. We hypothesized that dual targeting of the malignant hematopoietic clone and the fibrotic niche, via combined JAK2 inhibition (fedratinib) and Thbs1 antagonism, would provide enhanced therapeutic efficacy.

To test this, we utilized our competitive transplantation model of myelofibrosis, in which secondary fibrotic transformation occurs between 16 and 20 weeks post-transplantation (Figure 11B). This interval was defined as the treatment window. Lethally irradiated recipient mice were reconstituted with a mixture of JAK2V617F/JAK2WT cells together with wild-type competitor cells and monitored until week 16. Animals were then randomized to receive vehicle, fedratinib alone, LSKL alone, or a combination of fedratinib and LSKL for either four or eight weeks (Figure 20A).

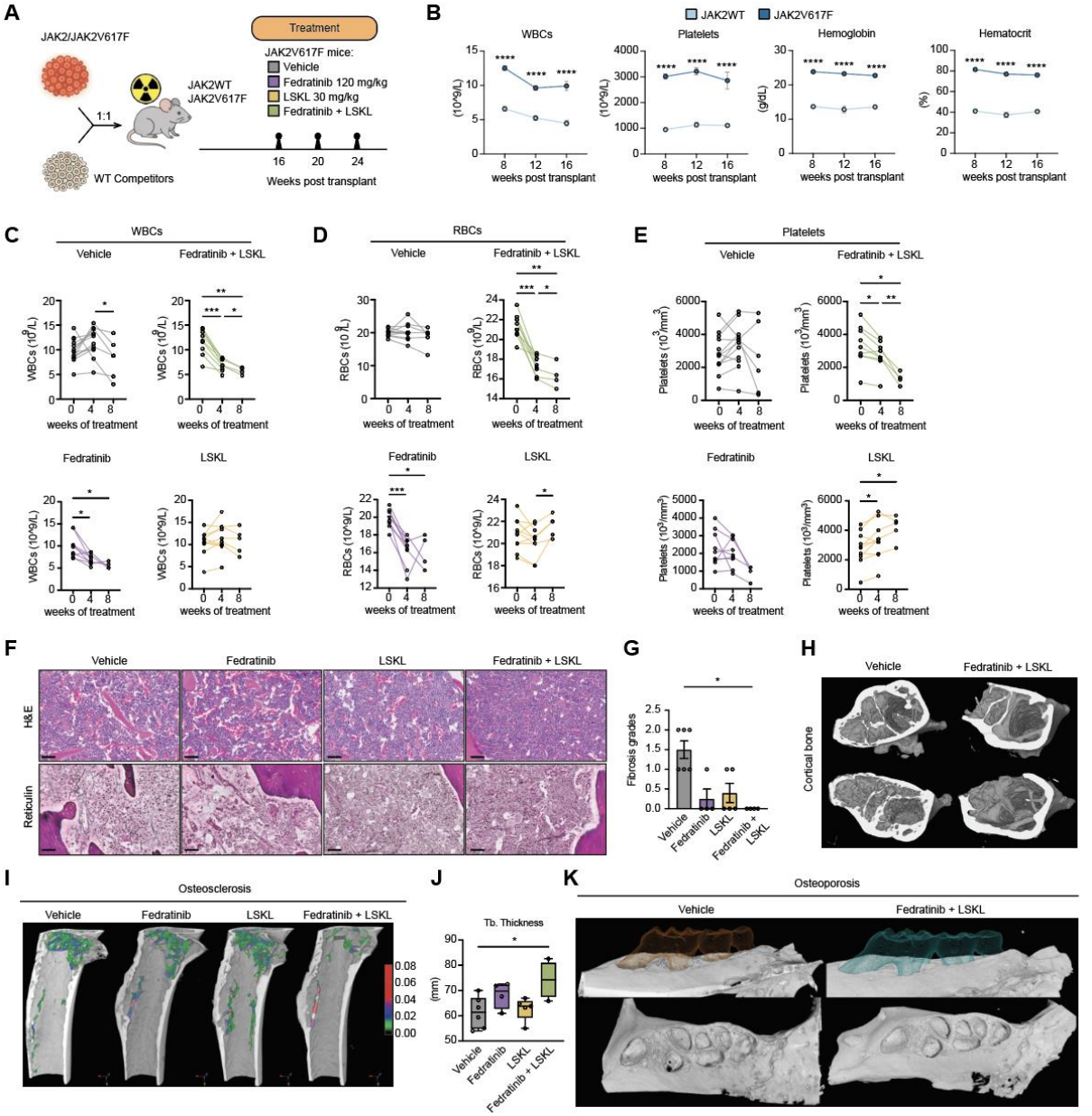

Figure 20: Combined inhibition of stromal Thbs1 and hematopoietic JAK2 restores the bone phenotypes across ontogenetically distinct bones in myelofibrosis.

(A) Schematic representation of the in vivo treatment strategy. Lethally irradiated recipient mice were competitively reconstituted with a 1:1 mixture of JAK2V617F/JAK2WT and wild-type competitor bone marrow cells. Peripheral blood parameters were monitored every four weeks beginning at week 4 after transplantation. At 16 weeks post-transplantation (designated as treatment initiation), JAK2V617F mice were assigned to receive vehicle (n=6), Fedratinib (n=4), LSKL (n=5), or combined Fedratinib and LSKL (n=4) until weeks 20 and 24 post-transplantation (corresponding to 4 and 8 weeks of treatment). Animal experiments were conducted by Dr. Ian Ghezzi, German Cancer Research Center. Schematic created with ChatGPT.

(B) Longitudinal hematologic measurements prior to treatment initiation, showing white blood cell (WBC) counts, platelet levels, hemoglobin, and hematocrit values in JAK2V617F and JAK2WT mice (n=5 per group). Statistical analysis was performed using two-way ANOVA with Sidak's multiple-comparisons test.

(C–E) Temporal analysis of hematologic parameters following therapy (4 or 8 weeks of treatment; corresponding to 20 and 24 weeks post-transplantation), including WBC counts (C), red blood cell (RBC) counts (D), and platelet levels (E). Each data point represents an individual mouse. Statistical comparisons were performed using two-way ANOVA with Tukey's post hoc test.
(F) Representative hematoxylin and eosin (H&E) and reticulin staining of tibial bone sections from mice after 8 weeks of treatment. Scale bars, 50 μm.
(G) Quantification and grading of bone marrow fibrosis based on reticulin staining in mice treated for 8 weeks with vehicle (n=6), Fedratinib (n=4), LSKL (n=5), or combined Fedratinib and LSKL (n=4). Statistical significance was assessed using the Kruskal–Wallis test.
(H–I) Three-dimensional micro-computed tomography (μCT) reconstructions of femoral cortical (H) and trabecular (I) bone following 8 weeks of treatment.
(J) Quantitative assessment of trabecular (Tb.) thickness in the proximal femur of 8-week treated mice. Statistical analysis was performed using one-way ANOVA with Holm–Sidak correction.
(K) Representative 3D μCT reconstruction of maxillary bone architecture after 8 weeks of treatment. μCT analysis was performed by Dr. Marta Rizk, Department of Orthodontics (RWTH Aachen Hospital). A-K) was previously included in Atakhanov S., Ghezzi I., Tejeda H. *et al.* BioRxiv 2026[54] .

At treatment initiation, JAK2V617F mice displayed a pronounced myeloproliferative phenotype characterized by elevated leukocyte, platelet, erythrocyte, hemoglobin, and hematocrit levels (Figure 20B). In vehicle-treated animals, leukocyte counts progressively declined, consistent with evolution toward secondary myelofibrosis (Figure 20C). While single-agent therapies exerted partial effects, only the combined fedratinib and LSKL regimen produced a durable and significant reduction in erythrocytes, leukocytes, and platelets throughout the treatment period (Figure 20C-E). Platelet normalization was particularly notable and was observed exclusively in the combination group.

Histological examination of bone marrow sections demonstrated restoration of vascular architecture and reduction of dysplastic megakaryocyte clustering in mice receiving dual therapy (Figure 20F). Reticulin staining further confirmed that progression of secondary myelofibrosis was fully prevented only in the combination-treated cohort (Figure 20G).

Micro–computed tomography analysis of the femur revealed that dual inhibition also corrected abnormal bone remodeling. The proximal femur, previously identified as the most severely affected region (Figure 12C), exhibited normalization of both osteosclerotic and osteoporotic alterations. Improvements included reduced cortical

thinning, decreased trabecular accumulation within the marrow cavity, and increased trabecular thickness (Figure 20H-J). Moreover, combined treatment mitigated alveolar bone loss in the maxilla and restored periodontal bone integrity (Figure 20K).

Together, these data demonstrate that targeting Thbs1 in conjunction with JAK2 inhibition exerts disease-modifying effects, simultaneously restraining mutant hematopoiesis, limiting fibrotic niche remodeling, and correcting pathological skeletal changes across developmentally distinct bone compartments.

5.16 Periodontitis exacerbates JAK2V617F-driven hematopoiesis and accelerates pre-fibrotic remodeling

After demonstrating that MPN alone is sufficient to induce periodontal pathology, we next investigated whether chronic periodontitis reciprocally influences JAK2V617F-driven hematopoiesis. As an initial population-level approach, we interrogated the UK Biobank dataset and identified 1,596 individuals with chronic periodontitis (ICD-10 code K05). Phenome-wide association analysis revealed strong enrichment of distinct cancer types and neoplastic conditions among these individuals. While head and neck malignancies showed the most significant associations, myeloid neoplasms, including myeloproliferative diseases, were also markedly overrepresented in patients with chronic periodontitis (Figure 21A). These findings support the concept of bidirectional interaction between chronic periodontal inflammation and MPN.

To explore causality, we employed a murine transplantation model. A mixture of 20% JAK2WT or JAK2V617F-mutant cKIT$^+$ cells and 80% wild-type competitor cells was transplanted into lethally irradiated WT recipients. Eight weeks post-transplantation, after full hematopoietic reconstitution, we induced experimental periodontitis using coil spring for three weeks as an orthodontic tooth movement model, with sham-treated animals serving as controls. Following coil spring removal, mice entered a resolution phase, allowing assessment of both inflammatory challenge and recovery dynamics (Figure 21B).

Peripheral blood analysis confirmed that mutant mice developed a polycythemia vera–like phenotype, characterized by elevated erythrocyte counts, hemoglobin, and hematocrit levels (Figure 21C). Importantly, erythrocytosis was further enhanced in

mutant mice subjected to periodontitis compared to sham-treated counterparts. Examination of the myeloid compartment revealed expansion of CD11b^{+} myeloid cells and Ly6C^{high} monocytes during the inflammatory phase (Figure 21D), indicating that periodontal inflammation promotes myeloid populations in the mutant mice known to contribute to fibrotic progression.

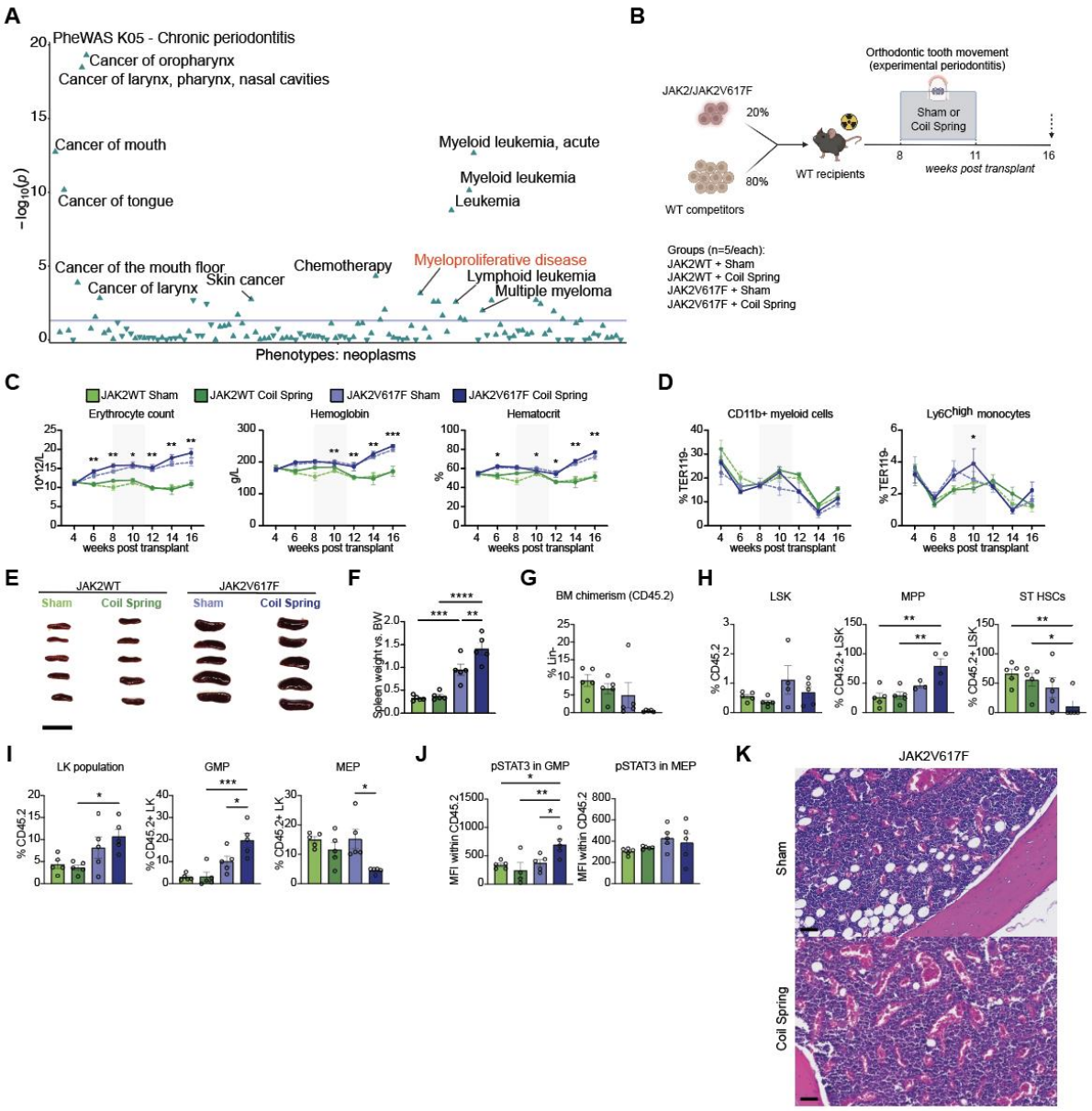

Figure 21: Murine reciprocal effect of periodontitis on mutant hematopoietic cells in MPN.

(A) Phenome-wide association study from UK Biobank (UKBB) focusing on cancer phenotypes of chronic periodontitis patients (n=1,596; ICD-10 K05). Data was provided by Prof. Carolin Schneider, Department of Gastroenterology, Metabolic Diseases and Intensive Care (RWTH Aachen Hospital).
(B) Experimental design of the murine competitive transplantation assay. cKIT+ cells from JAK2WT or JAK2V617F donors were mixed 1:5 with wild-type (WT) competitor cells and

transplanted into lethally irradiated WT recipient mice. 8 weeks after transplant, mice received coil spring (to mimic experimental periodontitis) or sham (only composite) for three weeks. Later, the coil spring was removed and mice lived for the next 5 weeks. Peripheral blood was collected every two weeks post-transplantation. n=5 mice per group. Created in BioRender. Goetz, K. (2026) https://BioRender.com/68r5f4b
(C) Flow cytometry analysis of longitudinal peripheral blood myeloid cells, including monocytes, following transplantation (n = 5 mice per group). Data were analyzed by two-way ANOVA followed by Tukey's multiple-comparisons test. Significance showing the comparison of JAK2V617F versus JAK2WT mice in the coil spring group. Grey bar represents the time of the coil spring duration.
(D) Longitudinal peripheral blood counts following transplantation (n = 5 mice per group). Data were analyzed by two-way ANOVA followed by Tukey's multiple-comparisons test. Significance showing the comparison of JAK2V617F versus JAK2WT mice in the coil spring group. Grey bar represents the time of the coil spring duration.
(E-F) Spleen size **(E)** and spleen weight versus body weight (BW) **(F)** at sacrifice. Scale bar, 1cm. Two-way ANOVA with post-hoc Tukey test was used.
(G) Flow cytometry analysis of bone marrow chimerism (CD25.2+CD45.1- donor cells) within the lineage negative fraction (Lin-) at the time of sacrifice. Two-way ANOVA with post-hoc Tukey test was used.
(H) Flow cytometric quantification of the CD45.2 donor-derived hematopoietic stem cell (HSC) compartment in the bone marrow at the time of sacrifice, including Lin-Sca1+cKIT+ (LSK), short term HSCs (ST-HSCs) and multipotent progenitors (MPPs). n=5 mice per group. Two-way ANOVA with post-hoc Tukey test was used.
(I) Flow cytometric quantification of the CD45.2 donor-derived hematopoietic stem and progenitor cell (HSPC) compartment from the bone marrow at the time of sacrifice, including Lin-Sca1-cKIT+ (LK), granulocyte-macrophage progenitor (GMP), megakaryocyte-erythrocyte progenitor (MEP). n=5 mice per group. Two-way ANOVA with post-hoc Tukey test was used.
(J) Mean fluorescence intensity (MFI) of phosphorylated STAT3 within the CD45.2 GMP and MEP fractions at the time of sacrifice. n=5 mice per group. Two-way ANOVA with post-hoc Tukey test was used.
(K) Representative H&E images comparing the bone marrow of JAK2V617F sham versus JAK2V617F coil spring group at the time of sacrifice. n=5 mice per group. Scale bar, 50µm.

16 weeks post transplant, spleen weights were significantly increased in mutant mice exposed to periodontitis in comparison to sham-treated mutant mice, suggesting enhanced extramedullary hematopoiesis and worsening of splenomegaly (Figure 21E,F). Within the bone marrow stem and progenitor compartment (Lin- population), frequencies of $CD45.2^+$ donor-derived cells were reduced in JAK2V617F mice following coil-spring treatment (Figure 21G). However, detailed immunophenotyping revealed marked shifts in lineage composition. Among donor-derived $Lin^-Sca1^+cKIT^+$ (LSK) cells, multipotent progenitors (MPPs) were expanded, whereas short-term HSCs were reduced in mutant mice exposed to periodontal inflammation (Figure 21H). In the $Lin^-Sca1^-cKIT^+$ (LK) compartment, overall progenitor frequencies increased,

with granulocyte–macrophage progenitors (GMPs) specifically expanded in coil spring-treated mutant mice, while megakaryocyte–erythroid progenitors (MEPs) were significantly diminished (Figure 21I). Notably, GMPs, but not MEPs, displayed elevated phosphorylated STAT3 levels, consistent with activation of JAK2V617F-dependent signaling pathways (Figure 21J).

Histological analysis of bone marrow sections from mutant mice of both sham and coil spring groups revealed reduced adipocyte content and increased neovascularization in mice exposed to periodontitis, features characteristic of early pre-fibrotic marrow remodeling (Figure 21K).

Collectively, these findings demonstrate that chronic periodontal inflammation acts as a secondary inflammatory insult that reshapes the hematopoietic stem and progenitor compartment and promotes early fibrotic transformation of the bone marrow. These data provide experimental evidence for bidirectional crosstalk between periodontitis and MPN progression.

5.17 A novel human organ-on-a-chip model fully recapitulates interactions between malignant hematopoiesis and periodontal disease

To mechanistically model how periodontal inflammation influences mutant hematopoiesis and promotes fibrotic transformation in a human setting, we established a three-dimensional human multi-organ microfluidic platform. This system was designed to recapitulate cross–organ communication between inflamed periodontal tissue and bone marrow under controlled perfusion conditions.

Human iPSC-derived BM organoids were competitively engrafted with equal proportions of JAK2WT;GFP and JAK2V617F;RFP hematopoietic stem and progenitor cells (1:1 ratio). These organoids were co-cultured on a microfluidic chip with periodontal ligament (PDL) fibroblast spheroids placed in a physically separate chamber. PDL spheroids were either left untreated (control) or stimulated with IL-1α to mimic inflammatory periodontal conditions (Figure 22A,B). The physical separation of BM organoids and PDL spheroids allowed interaction exclusively through circulating factors and migrating immune cells, enabling real-time tracking of fluorescently labeled

hematopoietic populations under homeostatic and inflammatory conditions (Figure 22C).

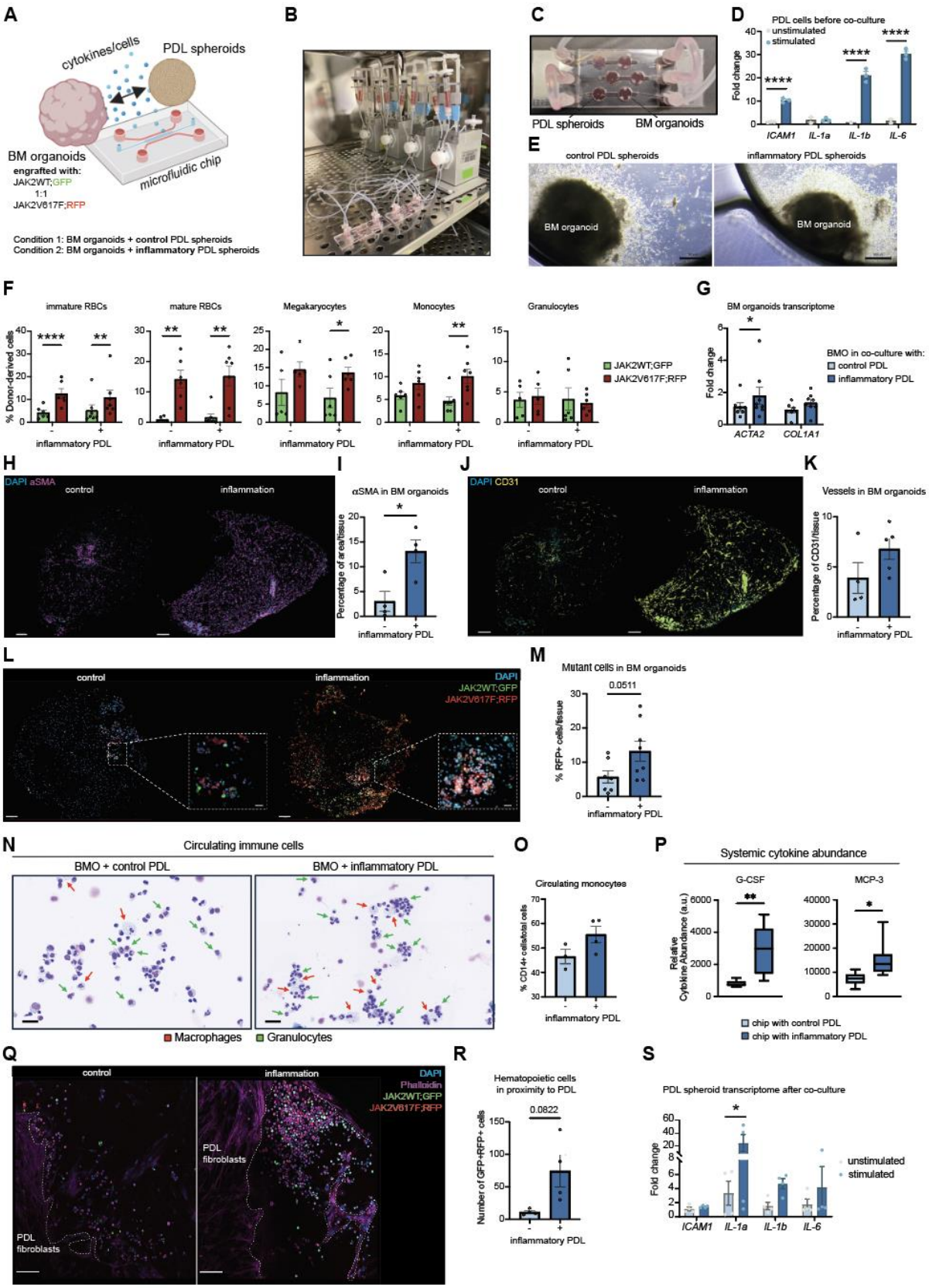

Figure 22: Novel 3D multi-organ-on-a-chip recapitulates the bidirectional interaction between periodontal inflammatory conditions and MPN.

(A) Representative image of the microfluidic experiment showing the fluidic unit with the chip. Created in BioRender. Atakhanov, S. (2026) https://BioRender.com/tkjcmrc

(B) Schematic overview of the experimental set up. Mature BM organoids were competitively engrafted with JAK2V617F;RFP and JAK2WT;GFP iPSC-derived CD34+ cells. Periodontal ligament (PDL) fibroblast spheroids were unstimulated (control) or IL1a (10ng/mL) stimulated (inflammatory) before placement on the microfluidic chip. Both BM organoids and PDL spheroids were co-cultured on the microfluidic chip for 7 days.
(C) Representative image of the microfluidic chip, showing wells with BM organoids and separate wells with PDL spheroids, enabling them to interact only via the circulatory cytokines and chemokines as well as BM organoids-derived hematopoietic cells.
(D) qRT-PCR of inflammatory markers from PDL fibroblasts stimulated with IL-1a (10ng/mL) for 48h prior to the co-culture experiment. Unstimulated PDL fibroblasts were used as control. Two-way ANOVA with Sidak's multiple comparisons test was used.
(E) Representative images of BM organoid-derived egress of hematopoietic cells in different conditions. Scale bars, 500µm.
(F) Flow cytometry analysis of donor-derived hematopoietic cells from the BM organoids co-cultured with either control and inflammatory PDL spheroids. Green bar represents the cells derived from JAK2WT;GFP donor. Red bars represent the cells derived from JAK2V617F;RFP donor. Two-way ANOVA with Sidak's multiple comparisons test was used.
(G) qRT-PCR of fibrotic markers from BM organoids co-cultured with either control or inflammatory PDL spheroids. Two-way ANOVA with Sidak's multiple comparisons test was used.
(H-I) Representative CODEX multiplex images of BM organoids stained with aSMA antibodies **(H)** and the quantification of the aSMA+ cells per area **(I)**. Scale bars, 100µm.
(J-K) Representative CODEX multiplex images of BM organoids stained with CD31 antibodies **(J)** and the quantification of the CD31+ cells per area **(K)**. Scale bars, 100µm.
(L-M) Representative BM organoid images demonstrating BM chimerism **(L)** and the quantification of the JAK2V617F;RFP+ cells per area **(M)**. Scale bars, 100µm and 20µm.
(N) Representative cytospin images of the circulating hematopoietic cells in the system. Red arrows show macrophages, green arrows show granulocytes. Scale bars, 20µm.
(O) Quantification CD14+ monocytes from the cytospin images.
(P) Analysis of human cytokine array with quantifications of relative abundance of G-CSF and MCP-3 from the conditioned medium.
(Q-R) Representative immunofluorescence images on the microfluidic chip demonstrating the myeloid infiltration of the well with PDL spheroids **(Q)** and the qquantification of GFP+RFP+ hematopoietic cells in close proximity to PDL spheroids **(R)**. Scale bar, 100µm.
(S) qRT-PCR of inflammatory markers from PDL fibroblast spheroids after the co-culture experiment. Two-way ANOVA with Sidak's multiple comparisons test was used.
Data was generated by Lucas Greven as part of his master thesis under my supervision.

Prior to the co-culture experiment, PDL fibroblast spheroids were stimulated with IL-1α to induce an inflammatory phenotype in the periodontal stromal cells (Figure 22D). The BM organoids demonstrated functional hematopoiesis, including active immune cell release into the circulating medium (Figure 22E). Notably, exposure to inflammatory PDL spheroids induced a marked increase in hematopoietic cell egress from the BM organoids, consistent with an emergency myelopoiesis response triggered by peripheral inflammation. Immunophenotypic analysis of the bone marrow

compartment confirmed a dominant erythroid bias of JAK2V617F-mutant cells (Figure 22F). Importantly, however, megakaryocyte and monocyte populations, key drivers of fibrotic remodeling[32,61], were selectively expanded in the presence of inflammatory PDL spheroids.

Transcriptomic profiling of fibrotic markers revealed significant upregulation of *ACTA2*, but not *COL1A1,* under inflammatory co-culture conditions (Figure 22G), indicative of early stromal activation and matrix remodeling. Co-detection by indexing (CODEX) multiplex imaging further confirmed increased αSMA and CD31 expression in BM organoids exposed to inflammatory PDL spheroids (Figure 22H-K), consistent with perivascular activation and enhanced angiogenesis. These findings closely mirror the vascular alterations and pre-fibrotic phenotype observed in our murine model.

Since mutant JAK2V617F cells were fluorescently tagged, we were able to directly assess their behavior under inflammatory stress. Periodontal inflammation strongly promoted expansion of RFP-labeled mutant hematopoietic cells within the BM organoids (Figure 22L,M), supporting the concept that peripheral inflammatory stimuli aggravate clonal dominance.

Given the perfusion-based design of the microfluidic system, we next investigated immune cell circulation between compartments. Conditioned medium derived cells were collected and subjected to cytospin preparation followed by Diff-Quick staining. Numerous immune cells were detected under both conditions; however, monocyte numbers were substantially increased in the inflammatory setting (Figure 22N,O). This observation recapitulates the elevated peripheral monocyte frequencies under periodontal inflammation observed in our murine model (Figure 21D) and supports the physiological relevance of the platform.

Cytokine profiling of cell-free conditioned medium revealed significant elevation of G-CSF and MCP-3 in chips containing inflammatory PDL spheroids (Figure 22P), consistent with enhanced myeloid mobilization and recruitment signals. Moreover, spatial analysis demonstrated accumulation of hematopoietic cells in close proximity to the inflamed PDL spheroids (Figure 22Q,R), indicating directed migration toward the inflammatory niche. Finally, qRT-PCR of the PDL fibroblast spheroids seven days after co-culture experiment confirmed their persistent inflammatory phenotype (Figure

22S). This finding reinforces the concept of mutant myeloid cell infiltration into neural crest–derived stromal tissues during periodontal inflammation.

6 Discussion

This thesis uncovers a previously unrecognized bidirectional interplay between MPNs and periodontal disease. It identifies Thbs1+ stromal populations as a unifying mediator of pathological skeletal remodeling across ontogenetically distinct bones in fibrosis in MPN. By integrating population-level analyses, murine models, single-cell multi-omics, spatial transcriptomics, and human organoid systems, this work provides mechanistic insight into how mutant hematopoiesis reshapes distant skeletal niches and, conversely, how periodontal inflammation feeds back to aggravate malignant hematopoiesis and accelerate fibrotic transformation.

6.1 MPN as a systemic skeletal disease

Although MF has long been recognized as a disease of the bone marrow, skeletal involvement has traditionally been studied in the femur. However, the skeletal consequences of JAK2V617F-driven malignant hematopoiesis remain insufficiently explored, despite mounting evidence that the mutant clone profoundly alters bone homeostasis[32,35]. Primary and secondary MF have traditionally been defined by bone marrow fibrosis and osteosclerosis, fostering the prevailing assumption that bone loss is largely absent in these disorders[34]. Yet, large epidemiological studies reveal an apparently contradictory increase in osteoporosis and fracture susceptibility across the broader spectrum of MPNs. In fact, a nationwide population-based study by Farmer and colleagues analyzed patients newly diagnosed with ET, PV and chronic myeloid leukemia (CML) across Danish hospitals between 1980 and 2010[62]. Their findings demonstrated that individuals with chronic MPNs have a significantly elevated risk of osteoporotic fractures compared with age-matched controls from the general population. The cumulative fracture incidence was reported at 3.01% for ET, 4.74% for PV, and 4.64% for CML patients, underscoring the clinically relevant skeletal fragility associated with these hematologic disorders. In a separate large-scale analysis including 18,171 MPN patients and 29,042 matched controls, female sex, Asian ethnicity, and a Charlson Comorbidity Index greater than 3% emerged as

independent predictors of fracture risk[63]. With respect to MF specifically, Usman and colleagues reported that osteoporosis was present in more than half of MF patients within a cohort of 2.4 million individuals with myeloid malignancies who underwent screening with a dual-energy x-ray absorptiometry (DEXA) scan, underscoring the profound impact of fibrotic disease on bone health[64]. Strikingly, fracture risk appears to correlate with fibrotic and JAK2-mutant disease states[38]. This observation suggests that increased bone density or osteosclerotic remodeling does not necessarily confer structural integrity and that excessive bone formation can coexist with, or perhaps even predispose to, skeletal fragility. Similar patterns are observed in related myeloid malignancies such as myelodysplastic syndromes (MDS) and chronic myelomonocytic leukemia (CMML), where bone loss, fractures, and inflammatory arthropathies are common[65]. Even at the stage of CHIP, premalignant mutations have been shown to promote inflammatory bone destruction[45]. These observations raise a fundamental paradox: a solitary oncogenic hematopoietic clone present in pre-malignant and overt myelofibrosis stages can be associated with both bone loss and aberrant *de novo* bone formation (osteosclerosis). Moreover, these opposing phenotypes may vary across anatomical sites and, in some instances, coexist within the same skeletal compartment. However, above-mentioned association-based studies do not address the directionality and mechanistic insights into the bone pathology in MPNs. Current conceptual models of MPN pathophysiology do not adequately account for this heterogeneity, nor do they sufficiently address the contribution of osteochondral lineage dynamics to skeletal remodeling in disease.

By integrating high resolution imaging, sequencing approaches and 3D *in vitro* models, we show that MPN induces both shared and niche-specific cellular programs across ontogenetically distinct skeletal compartments. In mesoderm-derived long bones, classical osteosclerosis develops within the marrow niche. However, this occurs in parallel with active trabecular thinning and growth plate–associated bone loss, revealing that osteoclast-mediated resorption remains functionally intact even within an osteosclerotic environment. These findings provide a mechanistic explanation for why bone loss has been underappreciated in MPNs: osteosclerosis masks ongoing, spatially restricted bone destruction rather than replacing it.

Building on our previous work[33], this data supports a model of niche-dependent stromal cell plasticity in MF. Under homeostatic conditions, osteolineage cells reside within the peritrabecular niche and sustain balanced bone turnover. Upon fibrotic injury, these cells become activated and redistribute from the growth plate toward the diaphysis (proximal part), where they drive excessive bone deposition, resulting in osteosclerotic remodeling. Despite the presence of osteoclast activity in the diaphysis, evidenced by trabecular thinning in proximal regions, the accumulation of activated osteolineage stromal cells within the peritrabecular niche appears to outcompete local resorptive capacity, thereby shifting the remodeling balance towards *de novo* bone formation. At the same time, depletion of osteolineage support from the growth plate niche creates a microenvironment with enhanced osteoclastogenesis. This imbalance is further intensified by the expansion of GMP (osteoclast precursors), ultimately leading to marked growth plate–associated bone loss. This thesis uncovered the mechanism of MPN-associated osteoarthritis development. Future studies have to dissect the mechanism of JAK2V617F mutant clone-driven osteoclast differentiation and its crosstalk with niche-dependent stromal cells.

Recent work by Romeo et al. revealed the existence of a specialized subset of osteoclast-lineage cells that associate with the vasculature and contribute to angiogenic remodeling rather than classical bone resorption[66]. These vessel-associated osteoclasts (VAOs) localize adjacent to blood vessels and support vascular patterning during skeletal growth, demonstrating the existence of osteoclast heterogeneity and their close interaction with vasculature. In the context of MF, we observed robust neo-angiogenesis within both peritrabecular and periodontal bone niches, accompanied by dysregulated osteoclastogenic signals and expansion of inflammatory myeloid progenitors. Given the prominent vascular remodeling and abundance of osteoclast-lineage cells in MPN-affected bone, it is plausible that VAO-like populations are recruited or expanded under chronic mutant hematopoietic stress, where they may participate in both angiogenesis and pathological remodeling. This raises the intriguing possibility that MPN-driven bone disease involves not only conventional bone-associated osteoclasts (BAO) but also vessel-associated subsets that link aberrant myeloid clonal activity to vascular and stromal reorganization, thereby contributing to the complex skeleton phenotypes observed across ontogenetically distinct niches.

The study by Kim et al. provides important mechanistic evidence that clonal hematopoiesis can directly induce anatomically restricted bone loss[67]. By integrating human genetic analyses with murine bone marrow transplantation models, the authors demonstrated that hematopoietic loss-of-function mutations in DNMT3A or TET2 result in significant trabecular bone reduction, particularly within the distal femoral metaphysis. Mechanistically, mutant myeloid cells displayed increased secretion of interleukin-20 (IL-20), a cytokine that promotes osteoclastogenesis and can be therapeutically targeted to reverse mutant clone–driven osteoporotic changes. These findings are in line with our observations of region-specific skeletal remodeling in JAK2V617F-driven disease. In both patient imaging and murine models, the proximal femur was characterized by osteosclerotic remodeling associated with stromal activation and osteolineage redistribution, whereas the distal femur and tibia exhibited comparatively reduced bone mineral density, indicating stronger vulnerability to osteolytic processes. Future investigations will be required to delineate how niche-specific stromal plasticity interacts with inflammatory myeloid clones during fibrotic progression.

6.2 Periodontal bone as a uniquely sensitive skeletal niche

This thesis demonstrates the profound involvement of periodontal bone in MPN. While previous investigations have largely focused on bone remodeling in mesoderm-derived bones, the impact of a hematologic malignancy itself on jaw and periodontal structures has remained largely unexplored. A central conceptual contribution of this work is the recognition that skeletal remodeling driven by JAK2V617F-mutant hematologic malignancy is not confined to axial and appendicular bones but also extends to the craniofacial skeleton. By revealing extensive remodeling within the maxilla and mandible in the context of JAK2V617F-driven MPN, our findings expose an unrecognized facet of interactions between hematologic cancer with ontogenetically distinct bones.

The embryonic development of the skeleton is a tightly regulated process, where different ontogeny of the stromal cells determines the formation of the anatomically distinct skeletal sites: neural crest cells give rise to clavicle and craniofacial bones, while mesoderm-derived cells to axial and appendicular bones.

Neural crest cells arise during early embryogenesis through a tightly regulated sequence of developmental events involving neural induction, lineage specification, epithelial-to-mesenchymal transition (EMT), and migration[68]. During gastrulation, signaling gradients establish the three germ layers. The ectoderm is patterned into: a) neural ectoderm, which forms the neural plate, and b) non-neural ectoderm, which forms epidermis. Intermediate signaling levels from BMP, Wnt, and FGF pathways specify a border region between these two domains known as the neural plate border. Cells in this region are fated to become neural crest cells. After delamination, neural crest cells migrate along defined pathways throughout the embryo and differentiate into diverse cell types depending on location: craniofacial bone, melanocytes and peripheral neurons as well as glia.

Such intrinsic developmental programs of neural crest, which differ from the mesoderm-derived bones, likely extend beyond embryogenesis and may influence postnatal tissue behavior, rendering craniofacial bones uniquely responsive to injury, inflammation, or age-associated diseases. In this context, we show that neural crest-derived neuronal cells in the periodontal tissue play a role in bone remodeling upon MPN. We demonstrate profound neuropathic phenotype and neurovascular inflammation in the periodontal bone, which might contribute to bone destructive phenotype. In line with our findings of neuroinflammation, Arranz et al. also showed that JAK2V617F-mutant HSCs in MPN trigger bone marrow sympathetic neuropathy and loss of associated Schwann cells, which leads to depletion of Nestin$^+$ mesenchymal stromal cells (MSCs) that normally restrain HSC behavior. Mechanistically, this niche damage was linked to IL-1β produced by mutant HSCs, and functional experiments demonstrated that depleting Nestin$^+$ cells (or their CXCL12 production) expanded mutant HSCs and accelerated disease, whereas neuroprotective/sympathomimetic approaches limited mutant HSC expansion[56]. Furthermore, Isern et al. then clarified a key developmental point: the Nestin$^+$ MSC population in long-bone marrow is largely neural crest–derived, quiescent, and specialized for HSC niche function, including high Cxcl12 output that supports HSC recruitment/retention. In contrast, mesoderm-derived Nestin$^-$ MSCs are more proliferative, contribute primarily to fetal skeletogenesis/endochondral programs, and rapidly lose MSC activity after birth[69].

Besides neuronal cells, our data demonstrate profound periodontal stromal cell perturbation in MPN. Across matched human samples and complementary murine models, macrophage–stromal communication emerged as a dominant axis of pathology in the jaw, coinciding with strong osteochondral activation and the striking appearance of chondrocyte-like stromal states. Importantly, these chondrogenic states emerged specifically in response to JAK2V617F-driven hematopoietic stress, supporting the concept of a single oncogenic hematopoietic clone driving niche-intrinsic periodontal stromal reprogramming as a hallmark of MF-associated craniofacial disease. In parallel, mesoderm-derived chondrocytes in long bones underwent analogous pathological rewiring on a transcriptional level, pointing to a shared osteochondral “injury” phenotype. Besides convergent phenotype across ontogenetically distinct bones, some differences were also seen. Neural crest-derived periodontal stromal cells underwent lineage plasticity toward ectopic chondrocytes, contributing to impaired osteogenesis and severe bone loss.

This pattern aligns with a growing body of evidence that stromal cell behavior upon injury is strongly constrained by developmental origin and anatomical position. A recent study[70] directly demonstrates that fibroblasts of different embryologic origins possess intrinsic, site-dependent fibrotic potential, with neural crest–derived facial fibroblasts exhibiting reduced dermal scarring compared with mesoderm-derived counterparts, mediated by a ROBO2–EID1 program that dampens pro-fibrotic transcriptional activity.

In line with our data showing ectopic chondrogenesis in response to mutant hematopoiesis, another study on craniofacial periosteal stem cells (PSCs) provides a mechanistic precedent: PSCs are specialized for intramembranous bone formation under homeostasis, yet can acquire endochondral bone-forming competence after injury, demonstrating that craniofacial stromal cells can switch between ossification programs upon stress[71]. This injury-enabled endochondral ossification machinery offers a highly relevant analogy to our finding that neural crest–derived periodontal stromal cells adopt a metaphyseal-like/chondrogenic transcriptional state under JAK2V617F hematopoietic stress.

Consistent with this paradigm, emerging jaw-injury literature supports the notion that craniofacial tissues can activate chondrogenic programs in response to damage, even

when such programs are not prominent in the homeostatic state. The recent study from Shi et al. on jaw pathology reports widespread tissue-level remodeling coupled to abnormal activation of Col2a1-associated (cartilage-linked) signaling, alongside vascular/lymphatic dysfunction in the injured jaw context, highlighting that craniofacial injury can be accompanied by a shift toward chondrogenic molecular signatures[72]. This injury-enabled endochondral ossification machinery offers a highly relevant analogy to our finding that neural crest–derived periodontal stromal cells adopt a metaphyseal-like/chondrogenic transcriptional state under JAK2V617F hematopoietic stress. In MF, disease and bone outcome is not dictated by a uniform interaction between mutant hematopoietic clones with the stromal compartment, but rather determined by stromal populations whose baseline epigenetic and transcriptional states are pre-patterned by ontogeny.

Moreover, both clinical imaging in MPN patients and μCT analyses in mice demonstrate that the maxilla is disproportionately affected compared with the mandible. We propose two non-mutually exclusive explanations: first, the maxilla's greater porosity and vascularization may facilitate enhanced infiltration and retention of circulating osteoclast precursors; second, distinct embryological programs imprint differences in stromal remodeling capacity. Although both bones derive from neural crest–derived ectoderm, the maxilla originates from the maxillary prominence of the first pharyngeal arch and forms a highly trabeculated intramembranous bone, whereas the mandible develops in association with Meckel's cartilage and acquires a thicker cortical architecture. The preferential maxillary bone involvement and its PDL area expansion as a compensatory response show that access (vascular entry), identity (ontogeny), and stress (mutant hematopoiesis) jointly determine site-specific craniofacial bone outcome.

Taken together, MF drives a spatially segregated and niche-dependent stromal remodeling program in which a solitary oncogenic hematopoietic clone can simultaneously drive *de novo* bone formation (osteosclerosis) and bone loss across ontogenetically distinct bones, coordinated by a shared osteochondral injury state. This shared chondrocyte-driven phenotype provides a unifying explanation for MPN-associated bone loss (arthritis, and periodontal disease) and reveals chondrocytes as central effectors of myelofibrosis-induced skeletal pathology.

6.3 Thrombospondin 1 as a unifying therapeutic target for two opposing skeletal outcomes: osteosclerosis and bone loss

A central mechanistic insight of this work is the identification of thrombospondin-1 as a unifying stromal mediator linking mutant hematopoiesis to niche remodeling across ontogenetically distinct skeletal compartments. Our data demonstrate consistent upregulation of Thbs1 in neural crest–derived periodontal stroma and mesoderm-derived bone marrow niches in both murine and human myelofibrosis, indicating that Thbs1 represents a conserved stromal injury response to chronic hematopoietic stress. Moreover, Thbs1 protein level is significantly elevated in the peripheral blood plasma of MPN patients potentially mediated by circulating platelets as well as remnants of stromal cells through leaky vasculature in the bone marrow[73].

In mesoderm-derived bones, we showed that Thbs1 is highly expressed in multiple key stromal subclusters. Our group has previously identified OLC3 as an injury-activated stromal progenitor population that gives rise to osteo-, chondro-, and fibroblast-primed trajectories during fibrotic remodeling[33]. Together with OLC1 and OLC2, these cells define an NCAM1^{+} peritrabecular stromal compartment that expands in myelofibrosis. The selective enrichment of Thbs1 within these peritrabecular stromal populations underscores a critical role for the trabecular/endosteal niche, particularly in the proximal femur, in orchestrating pathological stromal–myeloid crosstalk that associates fibrosis with bone loss.

Consistent with this role, Thbs1 has been broadly implicated in “inflammaging” and myeloid bias of HSCs. Ramalingam et al.[58] identify Thbs1 as a key regulator of inflammatory aging within hematopoietic stem cells (HSCs)and introduce a transcriptomics-based way to quantify “inflammaging” in stem cells. In mice, Thbs1 deletion was sufficient to suppress HSC “inflammaging”, preserving HSC fitness (self-renewal, reduced myeloid skewing) and preventing anemia with age. Notably, Thbs1 loss also correlated with broader healthspan improvements, including reduced systemic inflammatory cytokines and improved bone mineral density, suggesting Thbs1 sits at an actionable node connecting chronic inflammation, hematopoietic dysfunction, and skeletal aging.

Furthermore, Thbs1 was shown to play a central role in other cancer types. Daubon et al.[74] demonstrated that *Thbs1* expression increases with glioma progression and is transcriptionally induced through TGFβ–SMAD3 signaling, a pathway also enriched in our fibrotic stromal populations. Functionally, Thbs1 depletion in glioma reduced tumor invasion and growth, even in the context of anti-angiogenic therapy, highlighting its role as a key regulator of the tumor microenvironment. Importantly, pharmacological blockade of Thbs1–CD47 interactions using a peptide antagonist suppressed invasive behavior, and CD47 knockdown phenocopied these effects, establishing this signaling axis as therapeutically targetable. These findings closely align with our results showing Thbs1-CD47 axis mediating stromal-immune crosstalk across ontogenetically distinct bones. Moreover, our data also show that Thbs1 inhibition, particularly in combination with JAK2 blockade (fedratinib), reduces vascular remodeling and stromal activation in myelofibrosis.

Consistent with our findings of stromal cell-derived Thbs1, Weng et al.[75] also identified Thbs1 in the solid tumor microenvironment in mice implanted with B16–F10 melanoma cells, murine MC38 colon adenocarcinoma and murine MBP1 ovarian tumor cells. This study showed that Thbs1 is a driver of $CD8^+$ T-cell exhaustion through CD47 engagement, activating calcineurin–NFAT signaling and inducing TOX and inhibitory receptors. Critically, disrupting the Thbs1–CD47 axis partially restores sensitivity to immune checkpoint blockade and cytotoxic therapies, positioning the pathway as an immunotherapy-relevant target.

Emerging evidence indicates that Thbs1 is also an active contributor to myeloid malignancy progression and microenvironmental dysfunction. A recent study from Prummer *et al*.[76] demonstrated that Thbs1 is highly expressed in myelodysplastic syndromes (MDS), where it interacts with CD47 and shapes the immunosuppressive microenvironment, thereby promoting disease progression.

Besides cancer, Thbs1 plays a role in organ fibrosis, too. Thbs1 is a multifunctional matricellular protein that acts as a key regulator of TGFβ activation and represents a central mediator of fibrotic tissue remodeling[77]. Unlike global TGFβ inhibition, which disrupts physiological homeostasis, Thbs1 provides a disease-specific mechanism by converting latent TGFβ into its active form through direct binding to the latency-associated peptide (LAP) complex. This interaction disrupts the inhibitory LAP–TGFβ

complex and enables receptor signaling, thereby promoting extracellular matrix deposition, myofibroblast activation, and tissue fibrosis. The upregulation of Thbs1 has been implicated in multiple fibrotic diseases, including diabetic nephropathy, liver fibrosis, cardiac fibrosis, pulmonary vascular remodeling, and hematologic malignancies such as multiple myeloma[78]. It inhibits tissue regeneration, ultimately contributing to progressive organ dysfunction.

Pharmacological inhibition of Thbs1, when combined with clinically approved JAK inhibition, not only attenuates myeloproliferation, but also halts fibrotic progression and restores bone homeostasis. Strikingly, this combinational therapy simultaneously corrects stromal cell-mediated osteosclerosis and mutant hematopoietic clone-mediated osteoporosis, two opposing skeletal pathologies that co-exist within the same bone in myelofibrosis. Thus, our study uncovers Thbs1 as a central node linking hematopoietic malignancy, osteochondral injury and aberrant bone remodeling, providing a therapeutic avenue to normalize bone marrow fibrosis and skeletal pathology in MPN.

Although the Thbs1 antagonist LSKL has shown efficacy across fibrotic models, its limited pharmacokinetic properties limit direct clinical translation. From a therapeutic perspective, the development of stable inhibitors capable of selectively disrupting the Thbs1–CD47 interaction represents an attractive approach. Notably, next-generation Thbs1 inhibitors with improved pharmacokinetic properties, including SRI-35241[79] and the peptide TAX2[80], have recently emerged. While LSKL blocks Thbs1-TGFβ interaction, TAX2 selectively blocks Thbs1–CD47 signaling. TAX2 peptide has demonstrated efficacy in preclinical solid cancer models, and is in preparation to enter the phase Ia/b clinical trials for ovarian cancer[81].

Together, these advances suggest that pharmacological disruption of Thbs1 represents a promising therapeutic strategy in myelofibrosis. The clinical development of TAX2, in particular, raises the possibility of repurposing Thbs1-targeted therapies to achieve clinical disease modification in myelofibrosis.

6.4 Reciprocal interaction of periodontal inflammation in JAK2V617F-driven MPN

Recent work has begun to challenge the traditional paradigm that periodontitis is primarily a bacteria-driven disease by demonstrating that systemic inflammation alone can promote oral pathology. A large population-based analysis using UK Biobank data showed that elevated systemic inflammatory tone, measured by circulating C-reactive protein and genetically modulated IL-6 signaling, was associated with increased prevalence of tooth loss, bleeding gums, and periodontal disease indicators, supporting a directional link from systemic inflammation to oral pathology independent of local infection[82]. These associations align our data and suggest that periodontal disease can arise as a consequence of systemic immune dysregulation and highlight the importance of studying organ–organ crosstalk in inflammatory diseases. This conceptual shift is particularly relevant in myeloproliferative neoplasms, where chronic systemic inflammation driven by mutant hematopoietic cells directly reshapes periodontal tissues. Yet, whether periodontitis can reciprocally aggravate myeloproliferation and accelerate fibrotic development is incompletely understood.

To address the causality and directionality, murine models of experimental periodontitis play an essential role. Experimental periodontitis in mice is most commonly modeled using either ligature-induced or orthodontic coil spring–based approaches, which differ in their mechanisms yet recapitulate key aspects of periodontal pathology.

The ligature model induces disease through mechanical plaque accumulation and bacterial dysbiosis around the tooth, resulting in rapid inflammation, immune cell infiltration, and alveolar bone loss, thereby modeling infection-driven periodontal disease. For example, Li *et al*.[40] showed that oral inflammation using ligature-induced periodontitis is not confined to the gingiva: it propagates a durable “trained” program in the healthy bone marrow HSPC compartment, characterized by epigenetic rewiring and a sustained shift toward production of inflammation-primed myeloid cells. Strikingly, the authors showed that the periodontitis-trained state can be transferred by bone marrow transplantation into naïve recipients, which then display heightened inflammatory responsiveness and worse outcomes when challenged with inflammatory arthritis. Mechanistically, IL-1 signaling in hematopoietic progenitors is

required for this maladaptive training, positioning the IL-1 axis as a driver of periodontitis-to-systemic inflammatory “memory”. Haacke et al.[83] extended the trained-immunity framework from myelopoiesis to osteoclast precursor biology. In a ligature-induced periodontitis (LIP) model, prior induction of trained immunity (e.g., β-glucan) expands and functionally reprograms bone marrow osteoclast precursor (OCP) populations, creating a bias toward exaggerated osteoclast differentiation. As a result, the same periodontal challenge triggers greater inflammatory bone loss.

In contrast, the coil spring model applies continuous mechanical force that induces sterile inflammation, periodontal ligament remodeling, and osteoclast activation without reliance on bacterial accumulation. While both models produce bone resorption and inflammatory responses, the coil spring system more closely mimics chronic, low-grade inflammation and allows controlled induction and resolution phases, making it particularly suitable for studying inflammation-driven periodontal remodeling independent of microbial triggers. For example, Rizk et al.[50] demonstrated that mechanical orthodontic force applied using a coil spring induces extensive remodeling of periodontal tissues through a sterile inflammatory process characterized by spatially coordinated bone resorption and formation. Sustained force generates compression and tension zones within the periodontal ligament, triggering inflammatory signaling, vascular remodeling, and recruitment of immune cells, followed by osteoclast-mediated bone resorption and osteoblast-driven regeneration of alveolar bone. This dynamic remodeling reshapes the periodontal ligament architecture and surrounding bone microenvironment, providing a reproducible model of chronic and sterile inflammation–induced periodontal disease and tissue restructuring.

To investigate the impact of peripheral inflammatory stress on JAK2V617F-mutant hematopoiesis, we established a novel experimental framework using an orthodontic coil spring model in JAK2V617F-driven myeloproliferative disease. Previous studies have demonstrated that a three-week application of orthodontic force is sufficient to induce robust periodontal inflammation, bone remodeling, and tissue destruction that closely resemble features of chronic periodontitis[49]. Based on these observations, we applied coil spring stimulation for three weeks to establish sustained periodontal inflammation followed by a resolution phase, enabling assessment of how mutant

hematopoietic cells respond to inflammatory stress and subsequent recovery. This model therefore provides a controlled and physiologically relevant platform to investigate the bidirectional interaction between sterile peripheral inflammation and JAK2V617F-driven hematopoiesis, and represents a valuable tool to study disease comorbidities beyond infection-dependent paradigms.

Our data demonstrated that chronic experimental periodontitis elevates myelomonocytic cells in peripheral blood of MPN mice, suggesting the migration of these osteoclast precursors to the inflammatory site and contributing to enhanced periodontal resorption. Periodontal inflammation significantly elevated splenomegaly, enhanced extramedullary hematopoiesis and rewired mutant bone marrow hematopoiesis. In line with our findings, Li *et al*.[40] showed that experimental periodontitis may alter even the healthy stem cell compartment in the bone marrow. Overall, we show that periodontitis as an additional systemic inflammatory stimulus can aggravate mutant hematopoiesis and prime bone marrow for an early fibrotic transformation. Future investigations should focus on elucidating the molecular characteristics and underlying mechanisms by which mutant hematopoietic cells respond to periodontal inflammation.

6.5 Modeling disease comorbidities using a human organ-on-a-chip platform

Recent studies described a bioengineered human bone marrow niche within a 3D microenvironment in a perfusion-based system. For example, Ronaldson-Bouchard *et al.* described a sophisticated multi-organ microphysiological platform that integrates vascularized tissue niches, including engineered bone marrow–like environments, within a perfused organ-on-a-chip system[84]. Importantly, the engineered bone marrow niche incorporates stromal and vascular components that support hematopoietic cells within a three-dimensional architecture, representing a major advance over conventional two-dimensional culture systems by better recapitulating spatial organization and microenvironmental signaling cues. However, limitations of this model remain regarding faithful modeling of hematopoiesis. Although the system reproduces structural features of tissue niches, sustained release and maintenance of functional hematopoietic cells from the bone marrow niche remains challenging.

Another study by Ma *et al*. established a microengineered *in vitro* platform on a chip that models bone marrow pathology in B-cell acute lymphoblastic leukemia (B-ALL), enabling investigation of how niche architecture and genetic diversity within the bone marrow microenvironment contribute to treatment resistance[85]. Their next study creating a preclinical-trial-on-a-chip enables monitoring of CAR-T cell functionality against human leukemia[86].

A major technical advance of this work is the development of a human multi-organ-on-a-chip platform using iPSC-derived bone marrow organoids that enables mechanistic investigation of systemic disease comorbidities (MPN and periodontal disease) and inter-organ communication in a controlled experimental setting. By integrating human iPSC-derived bone marrow organoids with periodontal ligament fibroblast spheroids under microfluidic perfusion, this system recapitulates physiologically relevant circulation-mediated signaling between distant tissues. Unlike conventional *in vitro* models that study single tissue compartments in isolation or in static condition, this platform captures dynamic bidirectional communication between hematopoietic and peripheral stromal niches, thereby providing a powerful framework to dissect how systemic inflammation reshapes bone marrow hematopoiesis and disease progression.

In this iPSC-derived bone marrow organoid model, primary patient-derived donor cells can be tracked using membrane dyes such as CellVue[87]. However, rapid proliferation of primary hematopoietic cells leads to progressive dilution of the fluorescent label over successive cell divisions, limiting long-term lineage tracing and clonal fate mapping for studies culturing BM organoids for more than a week. To overcome this limitation, we generated isogenic iPSC lines harboring either the JAK2V617F mutation or CRISPR-repaired wild-type JAK2, which were stably labeled by lentiviral fluorescent reporters (RFP and GFP). This strategy enables durable tracking of mutant and control donor cells independent of proliferative history and allows longitudinal assessment of clonal behavior. Using this system, we could precisely monitor how mutant hematopoietic cells respond to periodontal inflammatory stimuli and investigate their contribution to microenvironmental remodeling and disease progression in a controlled human model.

We demonstrate that periodontal inflammation is sufficient to induce emergency myelopoiesis, enhance hematopoietic egress, and promote expansion of mutant JAK2V617F hematopoietic cells within the bone marrow niche. Inflammatory periodontal signals triggered stromal activation, angiogenic remodeling, and early fibrotic transcriptional programs in bone marrow organoids, closely mirroring the pathological features observed in our murine models. Moreover, the platform enabled direct visualization of immune cell migration and revealed increased monocyte trafficking toward inflamed periodontal tissues, highlighting a mechanistic basis for the systemic amplification of inflammation. These findings provide experimental evidence supporting a bidirectional relationship between local tissue inflammation and clonal hematopoiesis, suggesting that peripheral inflammatory conditions may actively exacerbate myeloproliferative disease progression.

Beyond modeling disease interactions, this organ-on-a-chip system represents a versatile preclinical platform for therapeutic evaluation under physiologically relevant conditions, including perfusion-based drug delivery and longitudinal monitoring of cellular responses. By capturing complex hematopoietic–stromal and inter-organ crosstalk in a human context, this approach bridges the gap between simple *in vitro* cell culture models and murine *in vivo* studies. More broadly, it establishes a framework for studying systemic disease networks and identifies organ-to-organ communication as a critical determinant of human pathology in chronic inflammatory and neoplastic disorders.

Collectively, this human multi-organ-on-a-chip system faithfully recapitulates the reciprocal interactions observed in our murine experiments and provides a physiologically relevant platform to study how systemic inflammatory conditions exacerbate mutant hematopoiesis and promotes early fibrotic transformation. This established model can be used for future mechanistic interrogation of human disease comorbidities and offers a powerful tool for translational studies.

7 Conclusion

This thesis challenges the prevailing view of cancer-driven bone remodeling as a unidirectional process and shows that a solitary oncogenic hematopoietic clone can simultaneously drive pathological bone formation and active bone destruction in a niche- and development-dependent manner across distinct skeletal compartments.

The developmental origin of stromal cells is increasingly recognized as a key determinant of tissue injury responses, yet how cancer exploits ontogenetic stromal diversity to remodel tissues postnatally in aging-associated diseases remains poorly understood. Using JAK2V617F-driven myeloid neoplasms as a paradigmatic model, we uncover an unexpected skeletal plasticity that extends beyond the classical osteoclast-centered explanation of osteosclerosis. In an interdisciplinary approach, this work provides clear mechanistic answers to each of the stated aims in the introduction part and collectively establishes a new framework for understanding skeletal pathology in clonal hematopoietic disease.

Through integrated patient imaging, population-level studies, murine transplantation models, single-cell transcriptomics, and human organoid systems, this thesis shows that mutant hematopoiesis alone is sufficient to induce spontaneous periodontal bone loss, establishing periodontitis as a direct and previously underrecognized comorbidity of clonal myeloid disease (MPN). Upon myelofibrosis, mesoderm-derived bone remodeling demonstrated niche-dependent phenotype: fibrotic stromal activation promotes osteosclerosis proximally, while distal regions display increased susceptibility to osteolytic remodeling.

A key insight of this work is that skeletal outcome is determined by developmental origin and niche context. Neural crest–derived maxillary stromal cells exhibit marked lineage plasticity, aberrantly activating chondrogenic and endochondral programs in response to hematopoietic stress, whereas mesoderm-derived chondrocytes undergo parallel pathological reprogramming. Across ontogenetically distinct compartments, a shared osteochondral injury state emerges, accompanied by amplified myeloid–stromal crosstalk and niche-specific osteoclastogenesis.

Mechanistically, Thrombospondin-1 (Thbs1) is identified as a unifying stromal mediator linking osteosclerosis to bone loss across neural crest– and mesoderm-derived bones. Pharmacological inhibition of Thbs1, particularly in combination with clinically approved JAK2 blockade, attenuates mutant clonal dominance, reduces fibrosis and angiogenesis, and normalizes pathological bone remodeling *in vivo* and in human bone marrow organoid systems.

Importantly, the relationship between MPN and periodontitis is bidirectional. While mutant hematopoiesis drives periodontal pathology, systemic periodontal inflammation in an orthodontic tooth movement model reciprocally aggravates MPN by enhancing mutant clonal expansion, emergency myelopoiesis, splenomegaly, and early fibrotic marrow remodeling. These findings establish a pathogenic feedback loop between oral inflammation and myelofibrosis (and thus bone remodeling) progression.

Finally, this work establishes a novel human multi-organ-on-a-chip platform that models bone marrow–periodontal crosstalk under perfused conditions. This system recapitulates inflammatory hematopoietic rewiring and provides a translational framework for studying disease comorbidities and for preclinical evaluation of anti-fibrotic therapeutic strategies.

Collectively, these findings redefine the skeletal dimension of clonal hematopoiesis, position periodontal bone as a highly vulnerable niche in MPN, and provide both mechanistic insight and therapeutic direction for targeting fibrosis-associated bone pathology.

8 Supplementary Informations

Patient Number	Diagnosis	MF grading	Gender	Driver mutation status
1	PMF	MF1	F	CALR pos
2	PMF	MF2	M	JAK2 pos
3	PMF	MF 2-3	F	JAK2 pos
4	PMF	MF2	M	triple negative
5	PMF	MF3	F	CALR pos
6	post-ET MF	MF3	M	CALR pos
7	post-ET MF	MF3	F	JAK2 pos

Supplementary Table 1: Characteristics of myelofibrosis patient cohort for the whole-body PET/CT imaging.

Patient number	Diagnosis	Driver Mutation	Fibrosis (p=primary, s=secondary)	Fibrosis grade
1	PMF	JAK2V617F	p	2
2	PMF	JAK2V617F	p	2-3
3	post-ET MF	JAK2V617F	s	1
4	PMF	JAK2V617F	p	3
5	PMF	CALR	p	3
6	PMF	JAK2V617F	p	2
7	PMF	JAK2V617F	p	3
8	postET-MF	JAK2V617F	s	3
9	PMF	JAK2V617F	p	3
10	PMF	JAK2V617F	p	3
11	PMF	JAK2V617F	p	3
12	PMF	JAK2V617F	p	3
13	post-ET MF	CALR	s	2
14	post-ET MF	MPL	s	2
15	MDS/MPN	triple negative	s	1
16	post-ET MF	triple negative	s	2

17	PMF	JAK2V617F	p	2
18	post-PV MF	JAK2V617F	s	2
19	post-ET MF	JAK2V617F	s	1
20	PMF	CALR	p	3
21	MDS/MPN	triple negative	s	0
22	PMF	MPL	p	2-3
23	PMF	JAK2V617F	p	2-3
24	post-ET MF	CALR	s	3
25	PMF + sAML	MPL	p	3
26	post-ET MF	CALR	s	1
27	PMF	CALR	p	1
28	MDS/MPN	JAK2V617F	s	2-3
29	post-PV MF	triple negative	s	1-2
30	post-ET MF	JAK2V617F	s	3
31	PMF	CALR	p	3
32	sAML	JAK2V617F + MPL	s	3
33	post-PV MF	JAK2V617F	s	2
34	post-ET MF	CALR	s	2

Supplementary Table 2: Characteristics of MPN patient cohort for the retrospective radiological CT scans.

Group	Patient Nr.	Hematol. Diagnosis	Mutation	Fibrosis	Fibrosis grade	Dental diagnosis	Isolated Teeth	Jawbone
MPN	1	PMF	JAK2V617F	p	2	Periodontitis, furcation involvement	37	Mandible

	2	PMF	JAK2V617F	p	2-3	Periodontitis, furcation involvement	36	Mandible
	3	post-ET MF	JAK2V617F	s	1	Apical periodontitis	15	Maxilla
Healthy for BM	4	negative, hip replacement						
	5	negative, hip replacement						
	6	negative, hip replacement						
Periodontitis	7	negative				Chronic Periodontitis	22, 23, 24, 26, 43, 42, 41, 31, 32, 33	Maxilla and mandible
	8	negative				Chronic Periodontitis	26, 37, 35, 47, 45	Maxilla and mandible
	9	negative				Chronic and Apical Periodontitis	15, 36, 47	Maxilla and mandible
Healthy for Teeth	10	negative				Caries, periodontium intact	17, 46, 47	Maxilla and mandible

Supplementary Table 3: Characteristics of patient cohort for single-cell RNA sequencing study.

9 List of Figures

10 List of Tables

11 Appendix

Abbreviations	*Full text*
3D	Three dimensional
AGM	Aorta-gonad-mesonephros
allo-HSCT	Allogeneic hematopoietic stem cell transplantation
AML	Acute myeloid leukemia
ANOVA	Analysis of variance
bFGF	Basic fibroblast growth factor
BM	Bone marrow
BMD	Bone mineral density
BMO	Bone marrow organoid
BMP4	Bone morphogenic protein 4
CALR	Calreticulin
CAR cells	CXCL12-abundant reticular cells
CD	Cluster of differentiation
cDNA	Complementary desoxyribonucleic acid
CHIP	Clonal hematopoiesis of indeterminate potential
CLP	Common lymphoid progenitor
CMP	Common myeloid progenitor
CODEX	Co-Detection by Indexing
CT	Computed tomography
DAPI	4',6-diamidino-2-phenylindole
DEG	Differentially expressed genes
DNAse	Deoxyribonuclease
EB	Embryoid body
EHT	Endothelial-to-hematopoietic transition
ELISA	Enzyme-linked immunosorbent assay
EPO	Erythropoietin
EPOR	Erythropoietin receptor
ET	Essential thrombocythemia
EV	Empty vector
FACS	Fluorescence-activated cell sorting
FCS	Fetal calf serum
FFPE	Formalin-fixed paraffin-embedded
FLT3-L	FMS-like tyrosine kinase ligand
G-CSF	Granulocyte colony-stimulating factor
GFP	Green fluorescent protein
H&E	Hematoxylin and eosin
HSC	Hematopoietic stem cell
HSPC	Hematopoietic stem and progenitor cell
HU	Hounsfield unit
IL	interleukin

iPSC	Induced pluripotent stem cell
IPSS	International Prognostic Scoring System
JAK2	Janus kinase 2
LAA	L-ascorbic acid
LSK	Lineage-Sca1+cKIT+
LSKL	Leucine-serine-lysine-leucine
M-CSF	Macrophage colony-stimulating factor
MCP 3	Monocyte chemotactic protein 3
MDS	Myelodysplastic syndrome
MEP	Megakaryocyte-erythrocyte progenitor
MF	Myelofibrosis
MPL	Myeloproliferative leukemia virus oncogene
MPN	Myeloproliferative neoplasm
MPP	Multipotent progenitor
MSC	Mesenchymal stromal cell
NiTi	Nickel-titanium
PDL	Periodontal ligament
PET/CT	Positron emission tomography / computed tomography
PFA	Paraformaldehyde
PheWAS	Phenome-wide association analysis
PMF	Primary myelofibrosis
PV	Polycythemia vera
qRT-PCR	Quantitative real-time polymerase chain reaction
RBC	Red blood cell
RFP	Red fluorescent protein
ROCK	Rock inhibitor Y-27632
ROI	Region of interest
RT	Room temperature
SCF	Stem cell factor
scRNA-seq	Single-cell RNA sequencing
SEM	Standard error of mean
SMA	Smooth muscle actin
SPF	Specific pathogen-free
ST-HSC	Short term hematopoietic stem cell
STAT	Signal transducer and activator of transcription
Thbs1	Thrombospondin 1
TPO	Thrombopoietin
TRAP	Tartrate-resistant acid phosphatase
UKBB	United Kingdom Biobank
UMAP	Uniform manifold approximation and projection
VEGF	Vascular endothelial growth factor
VOI	Volume of interest

Table 28: Abbreviations

Figure	Name	Affiliation	Contribution
Figure 1A-E	Prof. Nicolaus Kröger, Dr.med. Mathias Schäfersküpper	Department of Stem Cell Transplantation, University Medical Center Hamburg-Eppendorf, Hamburg, Germany	Provided raw data
	Salim Atakhanov	Institute of Cell and Tumor Biology	Analyzed the data
Figure 1F,G	Dr.med. Aleksandar V. Kargaliev	Department of Diagnostic and Interventional Radiology, Faculty of Medicine, RWTH Aachen University, Aachen, Germany	Analyzed the retrospective CT images
Figure 2A-C, Figure 16A	Prof. Carolin V. Schneider	Department of Gastroenterology, Metabolic Diseases and Intensive Care, Faculty of Medicine, RWTH Aachen University, Aachen, Germany	Provided the data
Figure 3B-I, Figure 4A-E, Figure 5B-E, Figure 9B-H, Figure 10A-K, Figure 11A-F, Figure 12A, Figure 13A,B	Dr. Hector Tejeda Mora	Department of Developmental Biology, Erasmus Medical Center, Rotterdam, The Netherlands	Analyzed biocomputational data
	Salim Atakhanov	Institute of Cell and Tumor Biology	Ethics approval, collected tissues, sorted cells and prepared sequencing libraries, supervised *in silico* analysis
Figure 6A-H, Figure 7A-G, Figure 8A-K, Figure 9A-H Figure 10A-H, Figure 11A-G, Figure 15	Dr. Ian Ghezzi	German Cancer Research Center (DKFZ), Division of Experimental Hematology, Heidelberg, Germany	Performed *in vivo* experiments
	Salim Atakhanov	Institute of Cell and Tumor Biology	Amendment for animal protocols, collected and processed all the tissues, analyzed wet lab data
Figure 7, Figure 8A-D, Figure 15H-K	Dr. Marta Rizk	Department of Orthodontics, Faculty of Medicine, RWTH Aachen	Analyzed murine micro-CT data

		University, Aachen, Germany	
Figure 10I-K, Figure 12A-H	scRNA-seq dataset from Banjanin B., Nagai J., Mun Y. *et al*. https://doi.org/10.1002/hem3.70309		
Figure 12B-F	Lina Schmidt	Institute of Cell and Tumor Biology	Analyzed spatial transcriptomics data
Figure 13C-G	Dr. Tata Nageswara Rao, Chiara Stüdle, Dr. Thomas Lehmann	Laboratory of Stem Cells and Cancer Biology, Division Oncology and Hematology, HOCH Health Ostschweiz, Cantonal Hospital St. Gallen, St. Gallen, Switzerland	Provided biopsies, performed ELISA
	Salim Atakhanov	Institute of Cell and Tumor Biology	Performed and analyzed Thbs1 staining
Figure 13H-Q, Figure 14D-I, Figure 17A-S	Lucas Greven	Institute of Cell and Tumor Biology	Partly performed and analyzed *in vitro* experiments as part of the master thesis project under my supervision
	Dr. Marcelo A.S.de Toledo	Department of Hematology, Oncology, Hemostaseology and Stem Cell Transplantation, Faculty of Medicine, RWTH Aachen University, Aachen, Germany	Established JAK2V617F;RFP and JAK2WT;GFP iPSC for fate mapping experiments
	Salim Atakhanov	Institute of Cell and Tumor Biology	Established iPSC-derived BM organoids in the Schneider Lab, designed all *in vitro* studies in this work, ethics approval for patient primary cells, partly performed and analyzed data
	Dr. Jitske Jansen	Department of Nephrology, Rheumatology, Clinical Immunology and Hypertension, Faculty of Medicine, RWTH Aachen	Established HD353.6 iPSC clone (used for generation of BM organoids)

		University, Aachen, Germany	
	Chloe Radermacher	Institute of Pathology, Faculty of Medicine, RWTH Aachen University, Aachen, Germany	Established immortalized PDL fibroblasts
	Dr. Rogerio Craveiro	Department of Orthodontics, Faculty of Medicine, RWTH Aachen University, Aachen, Germany	
	MPN iPSC clones were established and described in Flosdorf *et al.* https://doi.org/10.1016/j.stemcr.2023.12.011		
Figure 16B-K	Prof. Michael Wolf, Dr. Christian Niederau, Dr. Rogerio Craveiro	Department of Orthodontics, Faculty of Medicine, RWTH Aachen University, Aachen, Germany	Induced periodontal inflammation in mice using coil spring
Additionally to the above-mentioned: Figure 8E-K, Figure 11G, Figure 12G,H, Figure 16B-K	Salim Atakhanov	Institute of Cell and Tumor Biology	Performed and analyzed data

Table 29: Author contributions

12 References

1. Laurenti, E. & Göttgens, B. From haematopoietic stem cells to complex differentiation landscapes. *Nature* **553**, 418–426 (2018).
2. Kucinski, I. *et al.* A time- and single-cell-resolved model of murine bone marrow hematopoiesis. *Cell Stem Cell* **31**, 244–259.e10 (2024).
3. Ditadi, A., Sturgeon, C. M. & Keller, G. A view of human haematopoietic development from the Petri dish. *Nat Rev Mol Cell Biol* **18**, 56–67 (2017).
4. Yoder, M. C. Inducing definitive hematopoiesis in a dish. *Nat Biotechnol* **32**, 539–541 (2014).
5. Eilken, H. M., Nishikawa, S.-I. & Schroeder, T. Continuous single-cell imaging of blood generation from haemogenic endothelium. *Nature* **457**, 896–900 (2009).
6. Ivanovs, A. *et al.* Highly potent human hematopoietic stem cells first emerge in the intraembryonic aorta-gonad-mesonephros region. *J Exp Med* **208**, 2417–2427 (2011).
7. Weinhaus, B. *et al.* Differential regulation of fetal bone marrow and liver hematopoiesis by yolk-sac-derived myeloid cells. *Nature Communications* **16**, 4427 (2025).
8. Méndez-Ferrer, S., Lucas, D., Battista, M. & Frenette, P. S. Haematopoietic stem cell release is regulated by circadian oscillations. *Nature* **452**, 442–447 (2008).
9. Inra, C. N. *et al.* A perisinusoidal niche for extramedullary haematopoiesis in the spleen. *Nature* **527**, 466–471 (2015).
10. Lefrançais, E. *et al.* The lung is a site of platelet biogenesis and a reservoir for haematopoietic progenitors. *Nature* **544**, 105–109 (2017).
11. Rodríguez-Correa, E. *et al.* A kinetics-based model of hematopoiesis reveals extrinsic regulation of skewed lineage output from stem cells. *bioRxiv* 2025.02.04.636388 (2025) doi:10.1101/2025.02.04.636388.
12. Ferchen, K. *et al.* A unified multimodal single-cell framework reveals a discrete state model of hematopoiesis in mice. *Nature Immunology* **26**, 2086–2099 (2025).
13. Hajishengallis, G. & Chavakis, T. Inflammageing and clonal haematopoiesis interplay and their impact on human disease. *Nature Reviews Molecular Cell Biology* 1–17 (2026).
14. Singh, I. *et al*. Pre-existing stem cell heterogeneity dictates clonal responses to the acquisition of leukemic driver mutations. *Cell Stem Cell* **32**, 564–580.e6 (2025).
15. Izzo, F. *et al.* DNA methylation disruption reshapes the hematopoietic differentiation landscape. *Nature Genetics* **52**, 378–387 (2020).
16. Jaiswal, S. *et al.* Clonal Hematopoiesis and Risk of Atherosclerotic Cardiovascular Disease. (2017) doi:10.1056/NEJMoa1701719.
17. Bouzid, H. *et al.* Clonal hematopoiesis is associated with protection from Alzheimer's disease. *Nature Medicine* **29**, 1662–1670 (2023).
18. Grabek, J., Straube, J., Bywater, M. & Lane, S. W. MPN: The Molecular Drivers of Disease Initiation, Progression and Transformation and their Effect on Treatment. *Cells* **9**, (2020).
19. Viny, A. *et al.* Genetics of Myeloproliferative Neoplasms. *Hematology/Oncology Clinics of North America* **35**, 217–236 (2021).
20. McKerrell, T. *et al.* V617F hematopoietic clones are present several years prior to MPN diagnosis and follow different expansion kinetics. *Blood Adv* **1**, 968–971 (2017).
21. Hirsch, P. *et al.* Clonal history of a cord blood donor cell leukemia with prenatal somatic JAK2 V617F mutation. *Leukemia* **30**, 1756–1759 (2016).

22. Van Egeren, D. *et al.* Reconstructing the Lineage Histories and Differentiation Trajectories of Individual Cancer Cells in Myeloproliferative Neoplasms. *Cell Stem Cell* **28**, 514–523.e9 (2021).
23. Williams, N. *et al.* Life histories of myeloproliferative neoplasms inferred from phylogenies. *Nature* **602**, 162–168 (2022).
24. Sousos, N. *et al.* In utero origin of myelofibrosis presenting in adult monozygotic twins. *Nat Med* **28**, 1207–1211 (2022).
25. Ling, V. Y., Heidel, F. H. & Bywater, M. J. Pathogenesis and management of high molecular risk myeloproliferative neoplasms. *Haematologica* **110**, 863–876 (2025).
26. Junker, S. *et al.* Pb2203: Incidence and prevalence of myelofibrosis in Germany: A retrospective claims data analysis. *HemaSphere* **7**, e32222e6 (2023).
27. Gorantla, S. P. *et al.* Efficacy of JAK1/2 inhibition in murine myeloproliferative neoplasms is not mediated by targeting oncogenic signaling. *Nature Communications* **16**, 4833 (2025).
28. Maslah, N. *et al.* JAK2 inhibition mediates clonal selection of RAS pathway mutations in myeloproliferative neoplasms. *Nature Communications* **16**, 6270 (2025).
29. Méndez-Ferrer, S. *et al.* Bone marrow niches in haematological malignancies. *Nature Reviews Cancer* **20**, 285–298 (2020).
30. Comazzetto, S., Shen, B. & Morrison, S. J. Niches that regulate stem cells and hematopoiesis in adult bone marrow. *Dev Cell* **56**, 1848–1860 (2021).
31. Fröbel, J. *et al.* The Hematopoietic Bone Marrow Niche Ecosystem. *Front. Cell Dev. Biol.* **9**, 705410 (2021).
32. Leimkühler, N. B. *et al.* Heterogeneous bone-marrow stromal progenitors drive myelofibrosis via a druggable alarmin axis. *Cell Stem Cell* **28**, 637–652.e8 (2021).
33. Banjanin, B. *et al.* Wnt-dependent spatiotemporal reprogramming of bone marrow niches drives fibrosis. *bioRxiv* 2025.02.12.637594 (2025) doi:10.1101/2025.02.12.637594.
34. Veletic, I. *et al.* Myelofibrosis osteoclasts are clonal and functionally impaired. *Blood* **133**, 2320–2324 (2019).
35. Schäfersküpper, M. *et al.* Reconstructing skeletal homeostasis through allogeneic hematopoietic stem cell transplantation in myelofibrosis. *Nature Communications* **16**, 741 (2025).
36. Wu, Q. *et al.* Resilient anatomy and local plasticity of naive and stress haematopoiesis. *Nature* **627**, 839–846 (2024).
37. Koh, B. I. *et al.* Adult skull bone marrow is an expanding and resilient haematopoietic reservoir. *Nature* **636**, 172–181 (2024).
38. Holik, H. *et al.* Hip and Knee Osteoarthritis in Patients with Chronic Myeloproliferative Neoplasms: A Cross-Sectional Study. *Life (Basel)* **13**, (2023).
39. Kassebaum, N. J. *et al.* Global burden of severe periodontitis in 1990-2010: a systematic review and meta-regression. *J Dent Res* **93**, 1045–1053 (2014).
40. Li, X. *et al.* Maladaptive innate immune training of myelopoiesis links inflammatory comorbidities. *Cell* **185**, 1709–1727.e18 (2022).
41. Hajishengallis, G. & Chavakis, T. Local and systemic mechanisms linking periodontal disease and inflammatory comorbidities. *Nature Reviews Immunology* **21**, 426–440 (2021).
42. Zhang, Y. *et al.* Association of periodontitis with all-cause and cause-specific mortality among individuals with depression: a population-based study. *Scientific Reports* **14**, 21917 (2024).
43. Lim, H.-C. & Kim, C.-S. Oral signs of acute leukemia for early detection. *Journal of Periodontal & Implant Science* **44**, 293–299 (2014).

44. Migliorati, C. A. Periodontal diseases and cancer. *Lancet Oncol* **9**, 510–512 (2008).
45. Wang, H. *et al.* Clonal hematopoiesis driven by mutated DNMT3A promotes inflammatory bone loss. *Cell* **187**, 3690–3711.e19 (2024).
46. Flosdorf, N. *et al.* Proinflammatory phenotype of iPS cell-derived JAK2 V617F megakaryocytes induces fibrosis in 3D in vitro bone marrow niche. *Stem Cell Reports* **19**, 224–238 (2024).
47. Derlin, T. *et al.* Assessment of bone marrow inflammation in patients with myelofibrosis: an 18F-fluorodeoxyglucose PET/CT study. *Eur J Nucl Med Mol Imaging* **42**, 696–705 (2015).
48. Wolf, M. *et al.* Reduced Orthodontic Tooth Movement in Enpp1 Mutant Mice with Hypercementosis. *Journal of Dental Research* (2018) doi:10.1177/0022034518759295.
49. Craveiro, R. B. *et al.* [Ga]Ga-Pentixafor and Sodium [F]Fluoride PET Can Non-Invasively Identify and Monitor the Dynamics of Orthodontic Tooth Movement in Mouse Model. *Cells* **11**, (2022).
50. Rizk, M. *et al.* Periodontal ligament and alveolar bone remodeling during long orthodontic tooth movement analyzed by a novel user-independent 3D-methodology. *Scientific Reports* **13**, 19919 (2023).
51. Satoh, T. *et al.* Human DC3 Antigen Presenting Dendritic Cells From Induced Pluripotent Stem Cells. *Front Cell Dev Biol* **9**, 667304 (2021).
52. Boehnke, J. *et al*. CRISPR/Cas9 mediated CXCL4 knockout in human iPS cells of polycythemia vera patient with JAK2 V617F mutation. *Stem Cell Research* **55**, 102490 (2021).
53. Olijnik, A.-A. *et al.* Generating human bone marrow organoids for disease modeling and drug discovery. *Nature Protocols* **19**, 2117–2146 (2024).
54. Atakhanov, S. et al. Oncodevelopmental plasticity of the skeleton in myeloid neoplasms. BioRxiv 2026 https://www.biorxiv.org/content/10.64898/2026.03.19.712939v1.
55. Skinnider, M. A. *et al.* Cell type prioritization in single-cell data. *Nature Biotechnology* **39**, 30–34 (2020).
56. Arranz, L. *et al.* Neuropathy of haematopoietic stem cell niche is essential for myeloproliferative neoplasms. *Nature* **512**, 78–81 (2014).
57. Shin, Y., Won, Y., Yang, J.-I. & Chun, J.-S. CYTL1 regulates bone homeostasis in mice by modulating osteogenesis of mesenchymal stem cells and osteoclastogenesis of bone marrow-derived macrophages. *Cell Death & Disease* **10**, 47 (2019).
58. Ramalingam, P. *et al.* Suppression of thrombospondin-1–mediated inflammaging prolongs hematopoietic health span. *Science Immunology* (2025) doi:10.1126/sciimmunol.ads1556.
59. Frenz-Wiessner, S. *et al.* Generation of complex bone marrow organoids from human induced pluripotent stem cells. *Nature Methods* **21**, 868–881 (2024).
60. Kumar, R. *et al.* TGF-β activation by bone marrow-derived thrombospondin-1 causes Schistosoma- and hypoxia-induced pulmonary hypertension. *Nature Communications* **8**, 15494 (2017).
61. Hoeft, K. *et al.* Platelet-instructed SPP1 macrophages drive myofibroblast activation in fibrosis in a CXCL4-dependent manner. *Cell Rep* **42**, 112131 (2023).
62. Farmer, S., Horváth-Puhó, E., Vestergaard, H., Hermann, A. P. & Frederiksen, H. Chronic myeloproliferative neoplasms and risk of osteoporotic fractures; a nationwide population-based cohort study. *British Journal of Haematology* **163**, 603–610 (2013).
63. Lee, M. H. *et al.* Risk of Osteoporosis and Osteoporotic Fractures in Patients with Myeloproliferative Neoplasms. *Blood* **144**, 4560–4560 (2024).

64. Usman, S. J., Moore, J., Liesveld, J. L., Calvi, L. M. & Mendler, J. H. Associations between Myeloid Malignancies and Osteoporosis Using Real-World Data from the Trinetx Database. *Blood* **144**, 3798–3798 (2024).
65. Weeks, L. D. *et al.* Age-related diseases of inflammation in myelodysplastic syndrome and chronic myelomonocytic leukemia. *Blood* **139**, 1246–1250 (2022).
66. Romeo, S. G. *et al.* Endothelial proteolytic activity and interaction with non-resorbing osteoclasts mediate bone elongation. *Nature Cell Biology* **21**, 430–441 (2019).
67. Kim, P. G. *et al.* Dnmt3a-mutated clonal hematopoiesis promotes osteoporosis. *J Exp Med* **218**, (2021).
68. Gammill, L. S. & Bronner-Fraser, M. Neural crest specification: migrating into genomics. *Nature Reviews Neuroscience* **4**, 795–805 (2003).
69. Isern, J. *et al.* The neural crest is a source of mesenchymal stem cells with specialized hematopoietic stem cell niche function. (2014) doi:10.7554/eLife.03696.
70. Griffin, M. F. *et al.* Fibroblasts of disparate developmental origins harbor anatomically variant scarring potential. *Cell* **189**, 783–799.e20 (2026).
71. Debnath, S. *et al.* Discovery of a periosteal stem cell mediating intramembranous bone formation. *Nature* **562**, 133–139 (2018).
72. Shi, Y. *et al.* Vascular and Lymphatic Dysregulation via Non-EndoMT Col2a1 Signaling in Bisphosphonate-Related Osteonecrosis of the Jaw. *bioRxiv* 2025.09.27.678999 (2025) doi:10.1101/2025.09.27.678999.
73. Saad, M. *et al.* Non-invasive detection of bone marrow fibrosis in myeloproliferative neoplasms using cell-free RNA. *iScience* **29**, 114325 (2026).
74. Daubon, T. *et al.* Deciphering the complex role of thrombospondin-1 in glioblastoma development. *Nature Communications* **10**, 1146 (2019).
75. Weng, C.-H. *et al.* Thrombospondin-1–CD47 signaling contributes to the development of T cell exhaustion in cancer. *Nature Immunology* **26**, 2296–2311 (2025).
76. Prummel, K. D. *et al.* Inflammatory stromal and T cells mediate human bone marrow niche remodeling in clonal hematopoiesis and myelodysplasia. *Nature Communications* **16**, 10042 (2025).
77. Sweetwyne, M. T. & Murphy-Ullrich, J. E. Thrombospondin1 in tissue repair and fibrosis: TGF-β-dependent and independent mechanisms. *Matrix Biology* **31**, 178 (2012).
78. Murphy-Ullrich, J. E. & Suto, M. J. Thrombospondin-1 regulation of latent TGF-β activation: a therapeutic target for fibrotic disease. *Matrix biology : journal of the International Society for Matrix Biology* **68-69**, 28 (2017).
79. Suto, M. J. *et al.* Identification of Inhibitors of Thrombospondin 1 Activation of TGF-β. *ACS Med Chem Lett* **11**, 1130–1136 (2020).
80. Jeanne, A. *et al.* Identification of TAX2 peptide as a new unpredicted anti-cancer agent. *Oncotarget* **6**, 17981–18000 (2015).
81. Jeanne, A. *et al.* Targeting Ovarian Carcinoma with TSP-1:CD47 Antagonist TAX2 Activates Anti-Tumor Immunity. *Cancers (Basel)* **13**, (2021).
82. Berger, M. *et al.* Systemic inflammation is a risk factor for oral health: an analysis of data from the UK Biobank. *Front. Immunol.* **16**, 1651947 (2026).
83. Haacke, N. *et al.* Innate immune training of osteoclastogenesis promotes inflammatory bone loss in mice. *Dev Cell* **60**, 1854–1870.e6 (2025).
84. Ronaldson-Bouchard, K. *et al.* A multi-organ chip with matured tissue niches linked by vascular flow. *Nature Biomedical Engineering* **6**, 351–371 (2022).

85. Ma, C. *et al.* Leukemia-on-a-chip: Dissecting the chemoresistance mechanisms in B cell acute lymphoblastic leukemia bone marrow niche. *Science Advances* (2020) doi:10.1126/sciadv.aba5536.
86. Ma, C. *et al.* Bioengineered immunocompetent preclinical trial-on-chip tool enables screening of CAR T cell therapy for leukaemia. *Nature Biomedical Engineering* **9**, 2098–2114 (2025).
87. Ren, K. *et al.* Development of iPSC-derived human bone marrow organoid for autonomous hematopoiesis and patient-derived HSPC engraftment. *Blood Adv* **9**, 54–65 (2024).

13 Scientific contributions

13.1 List of publications

Atakhanov S.*, Ghezzi I.*, Tejeda H.M.*, Greven L., Rizk M., Schmidt L., Götz K., Merg L., Solozobova V., Benabid A., Wanner P., Lutterbach N., Kargaliev A.V., Schäfersküpper M., Florea A., Pearce J.E., Schmitz S., Schalla C., Wanek P., Craveiro R.B., Radermacher C., Stüdle C., Lehmann L., Weiler W., de Toledo M.A.S., Koschmieder S., Jansen J., Ayuk F., Kröger N., Mottaghy F.M., Truhn D., Kiessling F., Gleitz H.F.E., Rao T.N., Wolf M., Schneider C.V., Kramann R., Bock A., Crysandt M., Milsom M., Schneider R.K. (2026). Oncodevelopmental plasticity of the skeleton in myeloid neoplasms, *submitted*

*Contributed equally to the manuscript.

S.A. conceptualized the study, performed *in vitro* and *in vivo* experiments, collected all murine and patient samples, prepared the sequencing libraries, analyzed wet lab data, designed the figures and wrote the manuscript. I.G. performed *in vivo* experiments in Heidelberg as part of the collaboration for the manuscript. H.T.M. performed biocomputational analyses as part of the collaboration for the manuscript.

Dugué B., Wanner P., Ruiz M., Saad M., **Atakhanov S.**, Banjanin B., Brett V., Copin M., Fuchs S., Galyga A., Gleitz H., Götz K., Guy A., Hebeda K., Paz D., Lutterbach N., Parrens N., Peyrat A., Pritchard J., Schalla C., Schmitz S., Schmidt L., Séré K., James C., Costa I., Benabid A., Schneider R.K. and Dussiau C. (2026). Comprehensive spatial profiling of the spleen in murine and human myelofibrosis identifies targetable immune-stromal interactions. Cell Stem Cell, *in review*

B.D. and P.W. performed the experiments, evaluated all data, wrote the manuscript. S.A. performed some parts of *in vivo* and *ex vivo* experiments for the manuscript.

Atakhanov S., Christen D., Rolles B., Schüler H.M., Panse J., Chatain N., Koschmieder S., Brümmendorf T.H., de Toledo M.A.S., Zenke M. (2022). Towards personalized medicine with iPS cell technology: a case report of advanced systemic mastocytosis with associated eosinophilia. Annals of Hematology. doi: 10.1007/s00277-022-04975-9

S.A. performed all experiments, collected and evaluated the data, wrote the manuscript.

Boehnke J., **Atakhanov S.**, de Toledo M.A.S., Schüler H.M., Sontag S., Chatain N., Koschmieder S., Brümmendorf T.H., Kramann R., Zenke M. (2021). CRISPR/Cas9 mediated CXCL4 knockout in human iPS cells of polycythemia vera patient with JAK2 V617F mutation. Stem Cell Research. doi: 10.1016/j.scr.2021.102490

J.B. performed experiments, collected and evaluated the data, wrote the manuscript. S.A. performed some parts of *in vitro* experiments for the manuscript.

13.2 Oral and poster presentations

Atakhanov S., Ghezzi I., Tejeda H.M., Greven L., Pearce J.E., Koschmieder S., de Toledo M.A.S., Rizk M., Wolf M., Bock A., Crysandt M., Milsom M., Schneider R.K.: Developmental origin of stromal cells dictates skeletal remodeling in myelofibrosis. Poster presentation at the annual International Society of Experimental Hematology (ISEH) conference in Kumamoto, Japan, 25.09.2025

S.A and R.K.S. designed the poster. A.S. presented the work.

Atakhanov S.: From bone to bone: organ-on-a-chip reveals MPN stromal crosstalk. Lightning talk during the annual symposium on "Human pluripotent stem cell-derived hematopoiesis" in Kumamoto, Japan, 24.09.2025

Atakhanov S.: Accelerated systemic inflammation in the interplay of periodontal disease and MPN. Oral presentation at the annual CRU344 meeting in Aachen, 28.11.2024.

Atakhanov S., Ghezzi I., Rizk M., Goetz K., Schmitz S., Brenji S., Weiler M., Craveiro R.B., Milsom M., Kiessling F., Wolf M. and Schneider R.K.: MPN-associated systemic inflammation causes periodontal bone remodeling. Poster presentation on the Day on Organ Crosstalk at the RWTH Aachen Super C, 24.01.2024.

S.A. and R.K.S. designed the poster. A.S. presented the work.

Atakhanov S.: Mutual interactions between periodontal disease and chronic blood cancer. Oral presentation at the IZKF Consortium "soft tissue - alveolar bone", University Hospital RWTH Aachen, 16.03.2023.

13.3 Attendance of major international conferences in the field of hematology

54th Conference by International Society of Experimental Hematology (ISEH),
September 25-27, 2025, Kumamoto, Japan

2025 Symposium on Human pluripotent stem cell-derived hematopoiesis,
September 24, 2025, Kumamoto, Japan

12th International Heidelberg Symposium on Stem Cells and Cancer,
September 14-16, 2025, Heidelberg, Germany

European Hematology Association (EHA) Conference,
June 13-16, 2024, Madrid, Spain

52nd Conference by International Society of Experimental Hematology (ISEH),
August 18-20, 2023, New York City, NY, USA

2023 Symposium on Human pluripotent stem cell-derived hematopoiesis,
August 17, 2023, New York City, NY, USA

13.4 Awards

Ph.D. Fellowship by German Academic Exchange Service (DAAD)
“Forschungstipendien – Promotionen in Deutschland 2021-2025”

14 Acknowledgements

The first-person plural (“we”) is used throughout this thesis to reflect the collaborative nature of the research environment in which the presented work was performed.

First and foremost, I would like to thank my supervisor, Prof. Dr. med. Rebekka Schneider-Kramann, PhD**,** for giving me the opportunity to pursue this clinically relevant project while granting tremendous scientific freedom. Your mentorship, critical thinking, and passion for science have profoundly shaped my development as an independent researcher. I am deeply grateful for your trust, encouragement, and continuous support throughout both the successful and challenging phases of this journey. I would also like to sincerely thank the members of my thesis committee, Prof. Oliver Pabst and Prof. Ivan Costa**,** for their valuable external expertise, constructive feedback, and for evaluating this work.
My sincere appreciation goes to all past and present members of the Schneider and Milsom laboratories for fostering an inspiring, collaborative, and supportive scientific environment. I would especially like to thank Ian Ghezzi, Héctor Tejeda Mora, and Lucas Greven for making this project a true *tour de force*. It was a privilege and great fun working alongside you. I am equally grateful to Katrin Götz, Niklas Lutterbach, Pia Wanner, and Adam Benabid for accompanying countless Aachen–Heidelberg journeys and for waking up at 5 a.m. in hotel rooms to help finish experiments on time. Your dedication and teamwork meant a great deal.
I would like to acknowledge our collaborators and clinical partners, whose expertise made this interdisciplinary and clinically relevant work possible. My deepest gratitude goes to the patients and their families who generously agreed to provide biopsy material, enabling us to better understand their disease.
Beyond the scientific environment, I would like to thank my friends for their encouragement, patience, and for providing balance and perspective outside academia.

I also want to thank my family. И наконец, и самое главное, я хочу выразить свою глубочайшую благодарность моей семье. Одиннадцать лет жизни вдали от дома сделали этот непростой путь одновременно испытанием и огромным источником внутренней силы. Спасибо вам за вашу безусловную любовь, поддержку и непоколебимую веру в меня на каждом этапе этого долгого пути. Особую благодарность я хочу выразить вам за возможность изучать иностранные языки, за воспитание характера и внутренней стойкости, которые позволили мне пройти этот огромный путь через страны, культуры и научные границы к докторской степени. Моё образование и все достигнутые результаты - это отражение вашего труда, вашей самоотдачи и вашего вклада в меня. Эту диссертацию и полученный титул доктора наук я посвящаю вам - за ваше терпение, поддержку и за то, что всегда давали мне смелость идти вперёд, независимо от расстояний.

Fakultät für Mathematik und Naturwissenschaften | RWTH AACHEN UNIVERSITY

Eidesstattliche Erklärung

Salim Atakhanov

erklärt hiermit, dass diese Dissertation und die darin dargelegten Inhalte die eigenen sind und selbstständig, als Ergebnis der eigenen originären Forschung, generiert wurden.
Hiermit erkläre ich an Eides statt

1. Diese Arbeit wurde vollständig oder größtenteils in der Phase als Promovierender dieser Fakultät und Universität angefertigt;

2. Sofern irgendein Bestandteil dieser Dissertation zuvor für einen akademischen Abschluss oder eine andere Qualifikation an dieser oder einer anderen Institution verwendet wurde, wurde dies klar angezeigt;

3. Wenn immer andere eigene- oder Veröffentlichungen Dritter herangezogen wurden, wurden diese klar benannt;

4. Wenn aus anderen eigenen- oder Veröffentlichungen Dritter zitiert wurde, wurde stets die Quelle hierfür angegeben. Diese Dissertation ist vollständig meine eigene Arbeit, mit der Ausnahme solcher Zitate;

5. Alle wesentlichen Quellen von Unterstützung wurden benannt;

6. Wenn immer ein Teil dieser Dissertation auf der Zusammenarbeit mit anderen basiert, wurde von mir klar gekennzeichnet, was von anderen und was von mir selbst erarbeitet wurde;

7. Ein Teil oder Teile dieser Arbeit wurden zuvor veröffentlicht und zwar in:
   Atakhanov S., Ghezzi I., Tejeda H. et al. BioRxiv 2026
   https://doi.org/10.64898/2026.03.19.712939

30.06.2026